Die approbierte Originalversion dieser Dissertation ist in der Hauptbibliothek der Technischen Universität Wien aufgestellt und zugänglich.
http://www.ub.tuwien.ac.at

The approved original version of this thesis is available at the main library of the Vienna University of Technology.
http://www.ub.tuwien.ac.at/eng

Unravelling the corrosion mechanism in nanometer confined gaps using white light interferometry in reflection and transmission mode

An der Fakultät für Physik
Institut für Angewandte Physik
an der Technischen Universität Wien
zur
Erlangung des Grades eines Doktors der technischen
Naturwissenschaften (Dr.techn.)
eingereichte

D i s s e r t a t i o n

vorgelegt von

Dott. Mag.ssa Claudia Merola

geb. am 31.05 1989 in Mailand

Betreuung:	Univ. Prof. Dr. techn. Dipl.-Ing. Markus Valtiner
Berichterstatter:	Prof. Dr. Ir. Herman Terryn (Vrije Universiteit Brussel)
Mitberichterstatter:	Prof. Dr. Joelle Frechette (Johns Hopkins University)
Tag der Einreichung:	19.12.2018
Tag der mündlichen Prüfung:	21.01.2019

Ich erkläre an Eides statt, dass ich die vorliegende Dissertation selbstständig und ohne fremde Hilfe unter der Betreuung von Univ. Prof. Dr.Techn. DI Markus Valtiner verfasst habe. Es wurden keine anderen als die angegebenen Quellen und Hilfsmittel benutzt bzw. die wörtlich oder sinngemäß entnommenen Stellen als solche kenntlich gemacht.

Wien, am 19.12.2018

Acknowledgments

> Science knows no country, because knowledge belongs to humanity, and is the torch that illuminates the world.
>
> *L. Pasteur*

We all know that even if the PhD is considered to be a lonely project, the truth could not be further from this. My PhD was the most exciting and terrifying moment of my life and it allowed me to rediscover myself. I consider myself extremely lucky, since I had the chance to do a PhD in two different cities and meet and have next to me, such a high number of great people, friends and colleagues that motivated and spurred me constantly and I don't know how many others could state the same. Here, I will now try to thank all the people that made this possible. If I indeed have forgotten you, please don't take my short memory as a personal offence.

This big journey of my life started in Düsseldorf and it would have never been possible without the help and support of my supervisor so, I would like to express my gratitude to Prof. (a lot of titles in the middle) Markus Valtiner for the useful comments, remarks and engagement through the learning process of this PhD thesis. Markus, thanks for giving me so many opportunities, for allowing me to grow and for pushing me in improving myself. William, our working memory is definitely endless. However, all our synchrotron time remains the best, both in Taiwan and Grenoble. Thanks for being next to me since the beginning of the PhD, for showing me the light and dark side of the SFA, for saving my life and trying to kill me, for trying to teach me chinese. A note of thanks goes to Winnie of course, for showing me how to use the PVD and for the nice chatting. I wish you all the best with your master and both of you much luck for your future in Taiwan. Eberhard thanks for taking care of the machine and for always reserving me an extra spot in the scheduling. Kai thanks for helping me in trying to learn some programming notions, for showing me that for everything that happens there are multiple points of view and always having a word of comfort. A note should go to Philipp, Olga, Enrico, Avinah, Viswanadh and Boaz for making my stay in Max Planck so much fun. A thankyou should go to the workshop both in Düsseldorf and Vienna as well, that no matter how late we were bringing our sample/ drawings, somehow they always found time for doing the work at record time. Laila, big strong Mexican girl, you were my connection between work and the "outside world". Thanks for being such an honest friend and a great colleague,

things that are usually difficult to find in someone. Thanks for sharing with me the pain and joy of SurMat, for moving to Vienna so that we could support each other, for showing me the real tequila and, your questionable mexican food taste. To the whole **Ultimate group** thanks for being such a fantastic support and for being such an amazing group of friends. Without all our evenings, partys and activities, my stay in Düsseldorf would have been way much more boring and dark. Thanks for making Düsseldorf a place where I wanna come back and that I can call home. Vio, you are the best flatmate anyone could ever desire. Thanks for always taking care of me, trusting me with closed eyes and for believing in me without ever a shade of doubt. To my Ale(x) thanks for being a constant support, for always listening to me, for being always on my side, for giving me your "German" point of view and for believing in me so much. Wiebke, thanks for the running moments, the intensive training and for being always enthusiastic about any activity suggestions I have.

If this would have not been already enough to make it the most exciting time, there was still a challenge to play along with: moving to Vienna. Here the group started to become bigger and new people crossed my path. Dominik, thanks for showing me the ICP-MS, for your "special humor" and I wish you all the best for the PhD that with your creativity, limitless knowledge of the lab and your capabilities of building everything from nothing better than MacGyver will be smoother than you think. Pierluigi even if you are the less Italian person ever :p, you now have the responsibility to show some Italian culture to our colleagues and, non ti agitare che alla fine andrà tutto bene. Max thanks for bringing to work always a good mood. Yana thanks for the long talks in Stadtpark and for always having an opinion about everything, thanks for the constant company at work and outside. I hope I managed to show you some Italian food culture and that now you can start to show your culinary abilities on the other side of the planet. Laura, thanks for revealing to me that people from the UK are able to cook, I think it was one of the biggest discoveries of my PhD :). Thanks for spending time in correcting this thesis and making it possible that I was able to submit on time. Thanks for bringing my brain back to the earth when dark moments were approaching. Gastelle, thanks to you, every lunch break is now a comedy show. Giulia, thanks for making my stay in Vienna easier, for the late dinner, for the " we will eat just a salad" and then we put even the grandma inside, for talking to me in a language I could barely understand :p

Vale, thanks for convincing me to apply for a PhD position and for your constant support even when you are so far away. Silvia, thanks for being a constant friend in my life, no matter what, I know I will always be able to count on you. To **the coffee** that was a great company and without whose a lot of this work would have

not been possible in a reasonable amount of time. **“Don’t ever let anyone tell you that fairy tales aren’t real. I drink a potion made from magic beans every day, and it brings me back to life.“** *“The internet“.*

Last but not least I would like to thank my parents, for being such of a great support, for driving endless km to be there to comfort me, for helping me to move through Europe and for always having advice no matter how complicated the situation turned.

Abstract

Corrosion is a natural process, a gradual destruction of materials (usually metals) by a chemical and/or electrochemical reaction with their environment. A study of the National Academy of Corrosion Engineering estimated the annual cost of global corrosion at $2.5 trillion. So, it is no wonder that a better understanding of corrosion phenomena is a crucial task in electrochemistry. Among all types of corrosion, its occurrence in confined spaces remains one of the most difficult types to detect and prevent. Most often crevice corrosion (CC) occurs in narrow fissures where oxygen access is poor and a stagnant electrolyte solution is present. Crevice corrosion is of particular concern for stainless steel and nickel alloys in contact with chloride solutions, commonly found in marine environments. Experimentally it is a challenge to obtain in-situ information about processes in confined geometries and to establish well defined confined situations in the first place. Multiple beam interferometry (MBI) was used here to study and monitor the initial stage of the CC process of thin semi transparent layers of nickel in situ. Using mica as a crevice former in an electrochemical surface forces apparatus (SFA) allowed us to provide a deeper understanding of the initiation of the corrosion process. This novel technique provides not only an accurate real-time monitoring of corrosion in confined geometries, but is also capable to track and quantify localized nanoscopic features of the corrosion mechanism, such as pit formation with nano-to-microscale resolution. For instance, the shape of single localized corrosion sites (e.g. pits) and their depth profile can be directly tracked in real-time, yielding localized corrosion current densities in a well-defined confined geometry and currents from inside and outside the confinement can be detected. Further, we successfully extend MBI from transparent thin film materials to mirror polished bulk materials. We demonstrate the capabilities of MBI in reflection mode and compare the initial CC mechanism on confined nickel and a Ni model alloy in real time. Here, the study of bulk material was coupled with other techniques to study the morphology of the corroded samples, such as atomic force microscopy (AFM) and nano-Laue diffraction to correlate the local crystal structure, surface defects, domain orientation and dissolution process during the initiation of a corrosive process in confinement, where differences between the pure nickel and the nickel alloy mechanism were identified. Finally, to better understand the mechanism of dissolution and formation of the oxide film in different nickel alloys, similar experimental conditions were reproduced in a newly constructed Avesta type flow-cell, using time-resolved inductive coupled plasma mass spectroscopy (ICP-MS) analysis. Anodic polarization well into the transpassive region allowed us to isolate the role of different elements in protecting the alloys and follow their dissolution in real-time.

Glossary

Symbols

Symbol	Meaning
d_p	Pit Diameter
ΔD	Mirror Sift
h_p	Pit Depth
i	Current
t	time
U	Potential
J	Current Density

Abbreviations

Abbreviation	Meaning
AFM	Atomic Force Microscopy
ARXPS	Angle Resolved X-ray Photospectroscopy
CC	Crevice Corrosion
CCS	Critical Crevice Solution
CE	Counter Electrode
EBSD	Electro Backscattered Spectroscopy
EC-SFA	Electrochemical Surface Force Apparatus
EDL	Electric Double Layer
FECO	Fringes of Equal Chromatic Order
ICP-MS	Inductive Coupled Plasma-Mass Spectroscopy
MBI	Multiple Beam Interferometry
NR	Newton Rings
OCP	Open Circuit Potential
PVD	Physical Vapor Deposition
RE	Reference Electrode
SFA	Surface Force Apparatus
SEM	Scanning Electron Microscopy
WE	Working Electrode
XPS	X-ray Photospectroscopy

Chemicals

Symbol	Meaning
NaCl	Sodium Chloride
EtOH	Ethanol

Alloys

Name	Element composition
B2	nickel and molybdenum 26-30%
C276	nickel, chromium 15%, iron and molybdenum 16%

Contents

Acknowledgments ii
Abstract v
Glossary vi
Table of contents viii

I Introduction **1**

1 Motivation and Literature Reviews **2**
1.1 Literature background 2
1.1.1 Nickel and nickel alloys 2
1.1.2 Corrosion 3
1.1.3 The passive film 7
1.1.4 Corrosion in confinement 8
1.2 Motivation and overview of this work 12

2 Methodologies **14**
2.1 Electrochemistry 14
2.2 Scanning Electron Microscopy and Electron Back-scattered Spectroscopy 15
2.2.1 Electron Back-scattered Spectroscopy 15
2.3 Atomic Force Microscopy 17
2.4 Nano Laue Diffraction 20
2.5 X-Ray Photo-electron Spectroscopy 21
2.5.1 Angle Resolved X-ray Photo-electron Spectroscopy (ARXPS) 23
2.6 Chemicals and surface preparation 24
2.7 Preparation of sample alloys 24

II Results and Discussion **25**

3 Adapting the Surface Force Apparatus technique for corrosion research **26**
3.1 Multiple beam interferometry 26
3.1.1 Absolute distance measurement 28
3.2 Previous versions of the Surface Forces Apparatus 30
3.3 Opportunities for, sources of systematic and observational errors of the SFA technique 33
3.3.1 Potential errors of the optical system 33
3.4 New optical system for SFA measurements 37
3.4.1 Multiple beam interferometry in corrosion 40
3.5 SFA in reflection mode. 41
3.6 Interferometry calculation of transmission/ reflection mode 45
3.7 SFA in corrosion 45
3.8 Analysis of reflection mode with multiple matrix method 47

4 Real-time view of crevice corrosion of a Nickel thin film in an SFA in transmission mode **49**
4.1 Introduction 50
4.2 Apparatus Modifications 52
4.3 Experimental Procedure 53
4.4 Nickel Thickness Determination 54
4.5 Results and Discussion 54
4.6 Conclusions 63
4.7 Further investigations 64
Influence of oxygen and argon 64
Influence of the dynamic ramping of potential 66
Influence of the position of the counter electrode 68
Influence of the surface structure 69

5 Nickel and $Ni_{75}Cr_{16}Fe_9$: SFA in reflection mode **71**
5.1 Introduction 71
5.2 Results and Discussion 73
Operating principle and construction of a Surface Forces Apparatus for reflection mode application 73
Crevice formation and overview of the recorded crevice corrosion process in an rSFA. 76
5.3 Conclusions 91

6 EC-ICP-MS **93**
6.1 Introduction 94
6.2 Inductive Coupled Plasma-Mass Spectrometry 96
ICP-MS in corrosion 97
6.3 Results and discussion 98
6.4 Conclusions 107

7 Conclusions and Outlook **109**

Bibliography **111**

Appendix **122**
Resulting publications 122
Conferences participation 123
Copyright permission 124
List of figures 128
List of tables 129

Part I

Introduction

Chapter 1

Motivation and Literature Reviews

1.1 Literature background

1.1.1 Nickel and nickel alloys

Nickel is the fifth most abundant element on Earth with the majority of it being inaccessible within the earth's inner core. The silvery-white non-ferrous metal has: excellent corrosion resistance, mainly due to the spontaneous development of passive film; temperature resistance; possesses a high Young's modulus and displays a range of special magnetic and electronic properties. These characteristics occur both in pure nickel as in nickel alloys, making them the ideal material in a broad range of fields such as industry, military, transport, aerospace, marine, architecture and the general population, while their strength and resistance to corrosion, wear and fire make them a practical long lasting choice for public and industrial buildings. [1] In many of these applications there is no substitute for nickel without reducing performance or increasing production costs due to the tremendous design versatility. [2] However, the majority of nickel, 65% is used to manufacture stainless steels, another 20% is used for highly specialized industrial, aerospace –in the turbines– and military applications –aircraft Carrier and submarine nuclear power systems–and the rest is used, including coins, electronics, and in batteries for portable equipment and hybrid cars.[3] The most common alloys are the Ni-Cr-Fe alloys, which are the major components for stainless steel, wherein the percentage of nickel is between 8% and 12%. However, for more demanding resistance, such as in gas turbines or chemical plants, the concentration of nickel is increased.

Nickel use is growing at about 4% each year, while use of nickel-containing stainless steel is growing at about 6%. [4] The fastest growth today is seen in the newly and rapidly industrializing countries, especially in Asia. Nickel-containing materials are needed to modernize infrastructure, for industry and to meet the material aspirations of their populations. Despite nickel's corrosion resistant nature, it can still undergo localized crevice and pitting corrosion, especially in the presence of chlorides. Crevice corrosion has a higher likelihood to occur due to the more harsh environmental conditions created in the occluded cell.

The green side of nickel

Nickel is one of the most recycled materials globally. It is collected and recycled, mostly in the form of alloys. About half of the nickel content of a stainless steel product today comes from recycled sources.[5] Recycling of metals creates win-win situations for both the environment and industry. Among the non-ferrous metals, nickel is one of the most valuable, due to its excellent physical properties, so the commercial motivation to use it effectively is very high, moreover, from first use to last use, non-ferrous metals retain their basic properties and thus retain their utility value to a much larger extent than others materials. Within every stage of the recycling process, the nickel can be restored to its original quality without losing its intrinsic properties. Moreover, stainless steel is lighter than carbon steel but with the same mechanical properties; this leads to the possibility of using nickel stainless steel as a substitute in car manufacturing. Roland Gustafsson, manager of the consortium's research project known as Next Generation said "weight costs money, it costs efficiency, and it costs fuel."[4] At the end of their useful life, nickel-containing products can be collected and recycled for future use and re-use.

1.1.2 Corrosion

Corrosion is the natural process of degradation of a material when it reacts with its environment. The impact of corrosion is quite severe in different fields, and various studies have reported the economic impact of corrosion, but the two most significant are from Uhlig and NACE[6, 7]. As can be seen in **fig. 1.1** corrosion has a big impact economically on different fields, and its prevention would be very beneficial, since unfortunately, often in the past (and even now) it let to catastrophic events. A lot of the money could be saved, with a better understanding of the beneficial of a prior corrosion prevention, investing in monitoring the corrosion process, leading to a fewer failures and less money for cost production.

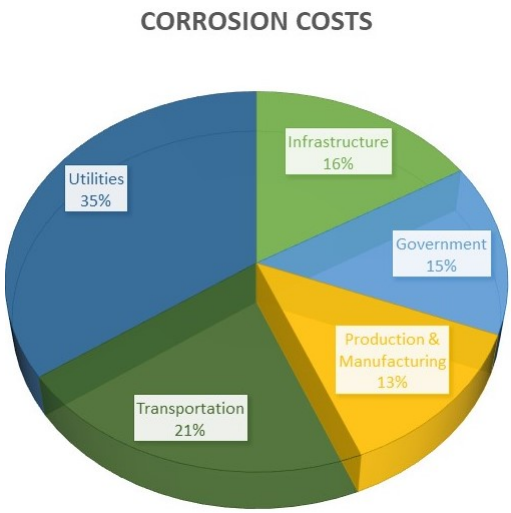

Figure 1.1: ***Distribution of the economic loss by field due to corrosion:*** *the figure shows how corrosion in economically affecting different fields. [8]*

The consequences of corrosion are, however, not limited to economic losses, but also involve health (as in metallic implants in the body), safety (as in the failure of vehicles and structures), and technology (as a developmental barrier to new technologies). The phenomenon of corrosion can often be observed visually, making it easier to prevent and control but it could also be present for a very long time without displaying any visual features, leaving it unnoticed until it results in catastrophic failure of the material and possibly severe damage.

When corrosion occurs in an aqueous environment, it is considered to be an electrochemical process. So when a metal surface is exposed to a conducting aqueous electrolyte, it normally becomes the site for two different reactions: an anodic oxidation reaction that implies the electronical dissolution of metal as metallic ions and resulting in a current (release of electron) as follows

$$Me \rightarrow Me^{n+} + ne^- \tag{1.1}$$

and a cathodic reduction reaction that consumes the electrons produced in the metal dissolution step. In most corrosive processes the counter reaction to the metal dissolution is the oxygen reduction as follows:

$$O_2 + 2H_2O + 4e^- \rightarrow 4OH^- \tag{1.2}$$

in neutral environment, and

$$O_2 + 4H^+ + 4e^- \rightarrow 2H_2O \tag{1.3}$$

for the acidic environment.

In case of hydrogen reduction in processes such as hydrogen embrittlement, as follows

$$2H^+ + 2e^- \rightarrow H_2 \tag{1.4}$$

Since both reactions, and anodic dissolution and a cathodic reduction, occur simultaneously on a metal surface, they can create a - so called localized - electrochemical cell/ or corrosion pair with an anode and cathode that could be adjacent or widely separated from each other, depending on the particular mechanism. For instance, the Evans drop experiment nicely conceptualizes and proves the picture of localized anode and cathode in a corrosion process. **Fig. 1.2** shows an Evans drop schematic in which the anode and the cathode are separated from each other. Evans placed a drop of diluted NaCl on a steel and followed with the help of pH indicator - due to the production of OH^- that will shift the pH to higher values -the develop of the anodic and cathodic area under the drop. The area closest to the interface liquid-air function as cathode since there the concentration of oxygen was higher, compared to the middle of the drop, where the oxygen is depleated.[9] At the anode, an oxidation of the metal will take place, resulting in the release of electrons, while at the cathode, a counter reaction will occur, more specifically a reduction, leading to the consumption of the generated electrons.

The spontaneity of the reaction is driven thermodynamically by the reduction of the Gibbs free energy: $\Delta G < 0$. In order to achieve this, the energy potential of the cathodic process must be higher than the anodic one. However, even if the corrosion process would be thermodynamically favourable, kinetics must be taken into account as well. The velocity of the corrosion process could be affected by a difference in oxygen concentration in the environment that would lead to differential aeration across the system, and so the zone with a depletion of oxygen will be the anode, while the one rich in oxygen will be the cathode. Similar effects can occur because of variations in the concentration of metal ions or other species in the environment. The flow of electrons between the corroding anodes and the cathodes forms the corrosion current, the value of which is determined by the electron production rate of the anode and the electron consumption rate of the cathode. The rates of electron production and consumption, of course, must be equal or a buildup of charge would occur.

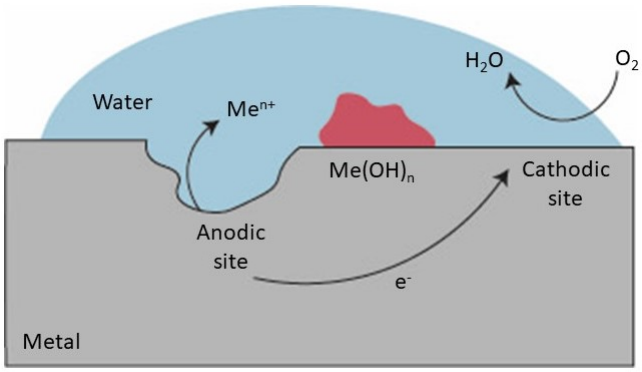

Figure 1.2: ***Corrosion cell****: shows the typical corrosion process in aqueous environment. The metal ions migrate from the anode to the cathode through an electrolyte (water); this process leads to the dissolution of the metal may than can form a metal hydroxide (red). This product itself could be the source of a crevice and so accelerate the corrosion process.*

In order to enable an electron flow between the anodes and cathodes, a driving force is required. The established driving force is identified as a potential difference between the anode and cathode. The foundations of this potential difference lies in the potential associated with each oxidation and reduction reaction and indicates the tendency of each reaction to occur spontaneously. The potential is a measure of this tendency. A useful way to study the relation of potential to corrosion is through the use of an equilibrium diagram developed by Pourbaix which plots potential versus pH, a parameter of great importance to corrosion processes [10]. Those diagrams enable the determination of the tendency of a metal surface to corrode by means of potential and pH measurements. Hereby various regions exists: immunity, where the tendency for corrosion is null; corrosion region, a region where the tendency for corrosion is high; passivity, a region where the tendency for corrosion may still exist but where there is also a tendency for a protective or passive film to exist.

Obtaining corrosion tendencies from the determination of potentials is necessary but not sufficient to ascertain whether a given metal or alloy will suffer corrosion under a given set of environmental conditions. This is because, while the tendency for corrosion may be strong, the rate of corrosion may be very low, and it may not present any problems. To determine corrosion rates a current is applied to a metal surface whose corrosion rate is being determined by means of an auxiliary electrode and the change in potential of that metal surface observed. When the potential of the metal surface is changed as a result of a flow of current to it, it is said to be polarized. If it is polarized in a positive direction (potential increases), it is

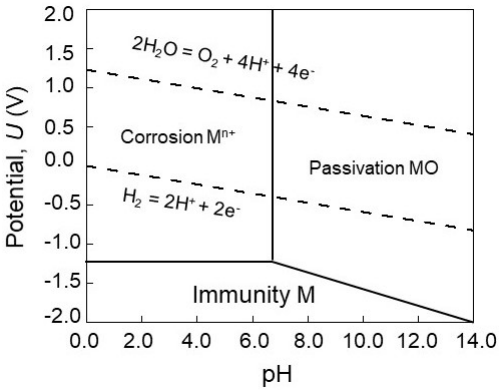

Figure 1.3: ***Pourbaix diagram for a general metal in water at 25 ° C.*** *Here three areas are highlighted: the immunity zone, the corrosion and the passivity one. The two dashed line represents the stability line of the hydrogen (button one) and the oxygen (upper one). In between the two lines, the water is stable.*

said to be anodically polarized; a negative direction signifies that it is cathodically polarized. The degree of polarization (the degree of potential change as a function of the amount of current applied) is a measure of how the rates of the anodic and the cathodic reactions are retarded by environmental (concentration of metal ions in solution) and surface process (adsorption, film formation, ease of release of electrons, etc.) factors.

1.1.3 The passive film

As discussed above, both thermodynamic (corrosion tendency) and kinetic (corrosion rate) considerations are crucial in dictating the speed and extent of the corrosion of a metal surface. A crucial factor in controlling the rate is the existence of the phenomenon of passivity for certain metals and alloys, such as stainless steels and titanium. Some metals, acquire a natural passivity, so they naturally grow a passive oxide film: this phenomenon is a key for our metal-based civilization. This oxide layer is normally a few nanometers thick and, effectively isolates the metal from the corrosive environment preventing it from the tendency to undergo further reactions. However if the protection fails, and the passive film is not reformed, the corrosion consequences are worse, since the damage is then concentrated on this specific site. There are two main theories regarding the nature of passive films which are: the oxide film theory and the adsorption theory. Historically, according to the oxide film theory, the passive film forms the diffusion barrier layer of reaction products that separates the metal from the environment and slows down the

reaction rate. In adsorption theory, from Langmuir, the passive metal is covered by a chemisorbed film of oxygen and that displaces the water molecules that are normally adsorbed [11, 12]. The rate of anodic dissolution is hereby slowed down by the hydration of the metal ions. To remain effective such a film must resist the breakdown processes that lead to the formation of localized corrosion. Nowadays the oxide layer theory is understood to be the predominant mechanism.

Two types of breakdown process for the oxide layer exist, chemical and mechanical. The many mechanisms proposed for chemical breakdown are based on two models, each having many variations. They are (a) adsorbed ion displacement models and (b) ion migration or penetration models. It should be noted that all of the breakdown mechanisms involve a damaging species. Unfortunately, one of the major species causing breakdown of passivity is the chloride ion, a damaging species abundantly available in nature. Mechanical breakdown occurs when the passive film is ruptured as a result of stress or abrasive wear. Fortunately, competing with the breakdown process there is a repair process: repassivation. Thus, an effective alloy for resisting localized corrosion would be one whose surface not only forms a passive film that resists the processes leading to breakdown but that is also capable of repassivating at a sufficiently high rate, so that once a breakdown has occurred exposure to a corrosive environment is minimal. In this case, the corrosion is said to be local. The passive film of Ni can be described by a bilayer model with the inner part consisting of nickel oxide (NiO) and with the outer part consisting of a hydroxylated NiO surface or a 3D nickel hydroxide $Ni(OH)_2$ layer.

The point defect model The question that now could rise is: is there any theory able to express both the growth and the breakdown of the passive film? The most accredited theory, regards the point defect model (PDM), developed by MacDonald and Lin in 1981. According to them, when the oxide grows, it does it with a crystalline structure that includes defects, some of those oxide can contain so much defects, to have almost a porous structure. According to this model, then dissolution of the passive film is due to a migration of the metal cations from the interface metal/ film to the interface film /solution leaving so holes on the upper layer of the passive film.. If the void grows to a certain critical size, the passive film suffer local collapse and the corrosion process can proceed. [13, 14]

1.1.4 Corrosion in confinement

Crevice corrosion (CC) is a type of localized corrosion that happens when there is an occluded region on a metal surface due to the presence of another surface

element. Due to its nature of being difficult to detect and since crevices that cause this form of corrosion can be readily created, for example through the gap in a flange or under a deposit, catastrophic structural failure can occur in situations where corrosion was unexpected. In these situations crevice corrosion may also go completely undetected until failure. [15] As for the Evans drop, in CC a local anode and cathode occurs, due to the specific geometric factors in a crevice as can be seen in **fig. 1.4** due to a differential aeration. Again a local anode (dissolution of the metal as in **equation 1.1** and the oxygen reduction at the outside are combined to form a local corrosion cell.

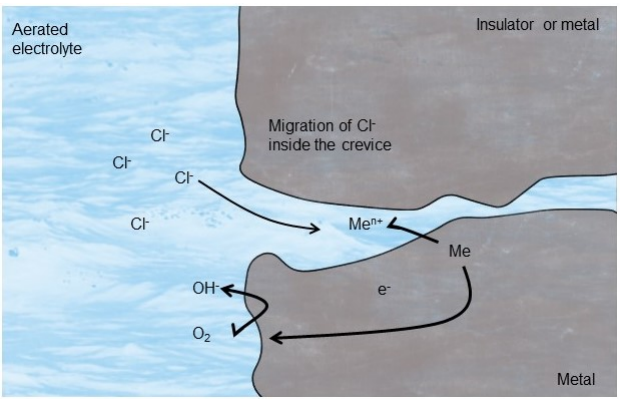

Figure 1.4: ***Crevice corrosion:*** *the schematic shows a typical example of crevice corrosion in a highly aggressive environment. The metal (M) is dissolving in its cations (M^{2+})*

Considering that crevice corrosion is normally caused by:

- separation of cathodic and anodic site
- hydrolysis of metal cations created by metal dissolution within the crevice leading to a local decrease in pH
- increase of chloride concentration inside the crevice to maintain charge neutrality
- the previous both aspects result in a accelerated dissolution of any protecting passive films, resulting in a sustained corrosion in the crevice,
- limitation on mass transport due to confinement may result in reaching solubility limits, which can slow down or stop an accelerating CC again.

We can easily derive that the crevice area (the anode) has a chemistry that is more aggressive than the one in the bulk[16]. Particular recognition was accorded

to Evans and Mears, to explain the reason for crevice corrosion that first attributed it to the formation of an electrochemical cell due to different areation. [17]

Another type of localized corrosion that shares with CC most of its characteristics is pitting corrosion, sometimes pitting can be the initial stage of crevice corrosion[18, 19]. Any passive alloy is fundamentally susceptible to crevice corrosion due to the loss of its protective oxide in the occluded region.

The stages of CC are **a)** incubation, **b)** propagation and **c)** saturation. During the incubation time, generally there is no localized attack, the environment is just entering the conditions that favor corrosion. Once the parameters for the critical condition are met, propagation occurs until the conditions inside the crevice are not anymore favorable to corrosion. As a result, the attack stops and complete repassivation of the crevice occurs (saturation).Crevice corrosion can be generally explained with two different models:

- **Critical crevice solution (CCS)**: The CCS mechanism was proposed by Fontana and Green and it is mainly it is described by the restrictions of mass transportation, due to the occluded region, and how the solution chemistry inside the crevice results in being highly different from the solution one. So, according to the model, the attack will be more severe the further it is from the crevice mouth, as deeper into the crevice the conditions will be more aggressive. The main drawback of the model is that it ignores the potential dependence of corrosion rate when it assumes the passive current density is low enough (mA/cm^2) as to not result in an appreciable potential drop within the crevice. When the pH and chloride ion concentration in the crevice solution cause disruption of the passive film the solution is said to have reached a critical state and crevice corrosion will initiate. This is the onset of the active stage of crevice corrosion with high rates of corrosion occurring in the crevice.

- **The IR model**: According to Pickering [18] , the occluded geometry can lead to ohmic potential drops. At this location –within the crevice– where the potential falls, there is an increase of the current density: the passive layer is no longer stable and the dissolution begins. This mechanism can be applied just to metals that show an active passive dissolution. The IR drop mechanism was first published by Pickering,[18] who stated that crevice corrosion would abruptly start when the potential difference between the crevice mouth and interior was large enough to cause the anodic potentials to become active. This difference is caused by the IR drop in the solution, the magnitude of which is due to factors such as concentration gradients, composition and geometry.

Since both models undergo strength and weakness, an attempt over the years was done to try to bring the two models together. In the incubation stage, the metal has spontaneously developed its passive film, and the current out of the crevice is governed by the passive current density; therefore the ohmic potential drop, characteristic of the CCS theory, is present due to the geometry restrictions of the crevice. In later stages, when the crevice solution becomes more aggressive, the metal dissolution rate, and thereby the current flowing through the crevice increases, resulting in a substantial potential drop. At this point, the IR criteria becomes more significant, and the location and magnitude of the attack become potential dependent. As the crevice solution changes, the representative boundary conditions are modified. Near the mouth of the crevice, the CCS cannot be maintained against diffusion, whereas at some point deeper into the crevice, the diffusion barrier is sufficient to create and maintain the CCS. At this location, the activation controlled kinetics lead to a high rate of dissolution. Deeper still into the crevice, the increased ohmic drop acts to decrease the dissolution rate until the open circuit potential (OCP) of the system is reached and the cathodic focusing effects described by Stewart become more important. [20] To implement this theory, other models were suggested: Oldfield and Sutton [21] developed a crevice corrosion solution theory (CCST) model that predicted the crevice corrosion incubation period for stainless steels. They assumed that there were no concentration gradients within the crevice, with mass transport occurring solely between the crevice and bulk fluid. Galvele [22] developed three CCST pitting corrosion models culminating in a model that considered diffusion, migration, and electroneutrality. The authors demonstrated that the pH within the pit was significantly lower than the bulk pH, with the major change occurring at the pit mouth.

Despite the amount of literature regarding crevice corrosion, a deeper understanding and visualization of the corrosion starting point is still missing. To have a better understanding of the corrosion mechanism, post-mortem analyses are normally performed; though valuable, they provide no real-time information on the evolution of corrosion and therefore are limited. Optical techniques are a solution to provide in situ knowledge about corrosion and being able to monitor the system. Light around the visible range from 250 nm up to the far infrared range, penetrates typically up to 55 nm of a metal, and it can transfer through transparent materials, making it suitable for analyzing thin film corrosion as well as surface layers. Some of the most used technique for studying corrosion layers is ellipsometry or differential reflectometry [23], as well as infrared and Raman spectrocopy. In addition, optical microscopy of corrosion damage as well as electron microscopy have been used for visualizing corrosive effects ex-situ, after a corrosion process occurred. Although these optical methods for corrosion are well established, they

interfere with the surface reactions or they can not be done in-situ. Direct observational methods have been used occasionally by some researchers in studying corrosion,[24] performed in situ analysis on aluminum with an optical microscope, Li [25] used an atomic force microscope combined with an optical microscope to study the initial stage of pitting corrosion. However, still very few techniques are able to directly measure and study reactivity in confinement in situ at relevant length scales, leaving even more uncertainty surrounding the initiation and early growth of dissolution or corrosion processes in confinement. This is due to the difficulty in establishing a confined zone, while beeing able to monitor any processes inside of this zone in real time. As a result, the understanding of early-stage reactivity in confinement remains challenging and more detailed nanoscale real-time characterization methods are required to develop a deeper understanding of CC.

1.2 Motivation and overview of this work

In this work, I introduce multiple beam interferometry (MBI) as a new tool for studying corrosion processes in confined zones in real time. MBI, which will explained in detailed below, is capable to view into a confined zone, it can characterize initial crevice corrosion of vapor deposited or sputtered metal thin films (with thicknesses in the range of 20-60 nm) under the influence of confined geometries. The idea for this technique is derived form a modified transmission mode surface forces apparatus (tSFA) setup, which is well know and frequently used in other fields such as adhesion and tribology research[26]. In this work I will show that a standard tSFA can be easily modified for corrosion studies, and I will demonstrate that this setup provides valuable information to explore the initiation of pitting and crevice corrosion of thin films of a Nickel model surfaces. However, the tSFA method is also limited to thin films, which often have distinctly different microstructures compared to bulk and specifically commercial alloys. This is a drawback that greatly restricts the investigation of commercially available alloys, and effects of microstructure. Therefore, I will also show how the classic tSFA can be extended to operation in reflection mode, allowing to probe CC on any sufficiently reflecting material in real time, inside of a confined area. The result and discussion part of this work is divided in 4 chapters: The first chapter is introducing the reader to the technique. After a small introduction about the history of the surface force apparatus, I will explain the modification that were established in order to adapt it to the different kind of CC measurements. In the following chapter, I will explain how the apparatus

was first used on a thin layer metal and the advantages that were derived. In chapter 4 we moved from thin film metal to metal blocks, in order to make the technique more versatile even for an industry point of view. I will explain which kind of modification were applied to the instrument and some extensive studied we did on the pure nickel and one model derivate. Finally, in the last chapter, different derivates from the Ni alloy were studied with inductive coupled plasma mass spectroscopy coupled with an Avesta type electrochemical flow cell, to further uncover corrosion mechanism and the role of different elements during the anodic metal dissolution in a crevice.

Chapter 2

Methodologies

In this chapter I will give an overview of the technique used in this work. They are ordered accorded to the chronogical use.

2.1 Electrochemistry

The majority of the electrochemical experiments performed in this thesis are linear sweep voltammetry in which the potential was ramped up at 1 mV/s. All data is referenced to the Ag|AgCl potential for comparison. For the surface forces apparatus experiments, Pt wire was used both as reference and counter electrode. Every Pt pseudo reference used in SFA experiments was referenced against a standard 3N Ag|AgCl electrode, showing a difference of about + 200 mV with typical variations of 50-80 mV depending on the Pt wire used. For Inductively Coupled Plasma Mass Spectrometry (ICP-MS) data an Ag|AgCl electrode was used as reference and Pt wire as counter electrode. All measurements were performed in 1 mM NaCl solution.

To ensure that the recorded electrochemical signal in the reflection SFA is related to the polished surface, all samples were first sealed with epoxy glue, and then polished to the desired surface finish. During SFA experiments the experiments were initiated at E_i: -0.1 V vs. open circuit potential (OCP), and scanned to an upper limit of E_f: 1.5 V vs. E_{ref}, if not stated otherwise below. In the flow cell ICP-MS setup, experiments were performed with a Ag|AgCl reference electrode and a Pt wire as counter electrode, starting from a potential of -0.2 V against Ag|AgCl until 1.6 V.

2.2 Scanning Electron Microscopy and Electron Back-scattered Spectroscopy

In a scanning electron microscope (SEM) when a focused beam of electrons is directed through a specimen surface it interacts with the atoms of the sample, and produces signals (i. e. secondary electrons, backscattered electrons) that contain information about the surface topography and composition of the specimen. In a typical SEM, an electron beam, which typically has an energy ranging from 0.2 keV to 40 keV, is thermionically emitted from an electron gun fitted with a tungsten filament cathode. The beam is then focused by one or two condenser lenses to a spot about 0.4 nm to 5 nm in diameter. The beam passes through pairs of scanning coils or pairs of deflector plates in the electron column, typically in the final lens, which deflects the beam in the x and y axes, is used to scan it in a raster fashion over a rectangular area of the sample surface.

The magnification and resolution in a SEM is not dependent on the objective lenses, they are just needed to focus the beam. In an SEM, as in scanning probe microscopy, magnification results from the ratio of the dimensions of the raster on the specimen and the raster on the display device. Assuming that the display screen has a fixed size, higher magnification results from reducing the size of the raster on the specimen, and vice versa. Magnification is therefore controlled by the current supplied to the x, y scanning coils, or the voltage supplied to the x, y deflector plates, and not by objective lens power.

2.2.1 Electron Back-scattered Spectroscopy

When interest in the specimen goes beyond the surface and topography, to include the crystallographic structure of the material, as in the grain structure of metals, then Electron Back-scattered Diffraction (EBSD) is needed. To perform an EBSD analysis, the specimen has to be flat or well polished. The polishing procedure includes: grinding with sand paper of different grain size (from P80 to P2500), then polishing with diamond paste of 0.05μm and final polishing with OPS-suspension for EBSD preparation. The specimen is then introduced into a SEM chamber equipped with an EBSD detector containing at least a phosphor screen, compact lens and low light CCD camera. In order to enhance the contrast of the resultant back scatter diffraction pattern, the surface has to be introduced with a tiltation angle of 70° from horizontal. The phosphor screen is located within the specimen chamber of the SEM at an angle of approximately 90° to the pole piece and is coupled to a compact lens which focuses the image from the phosphor screen onto

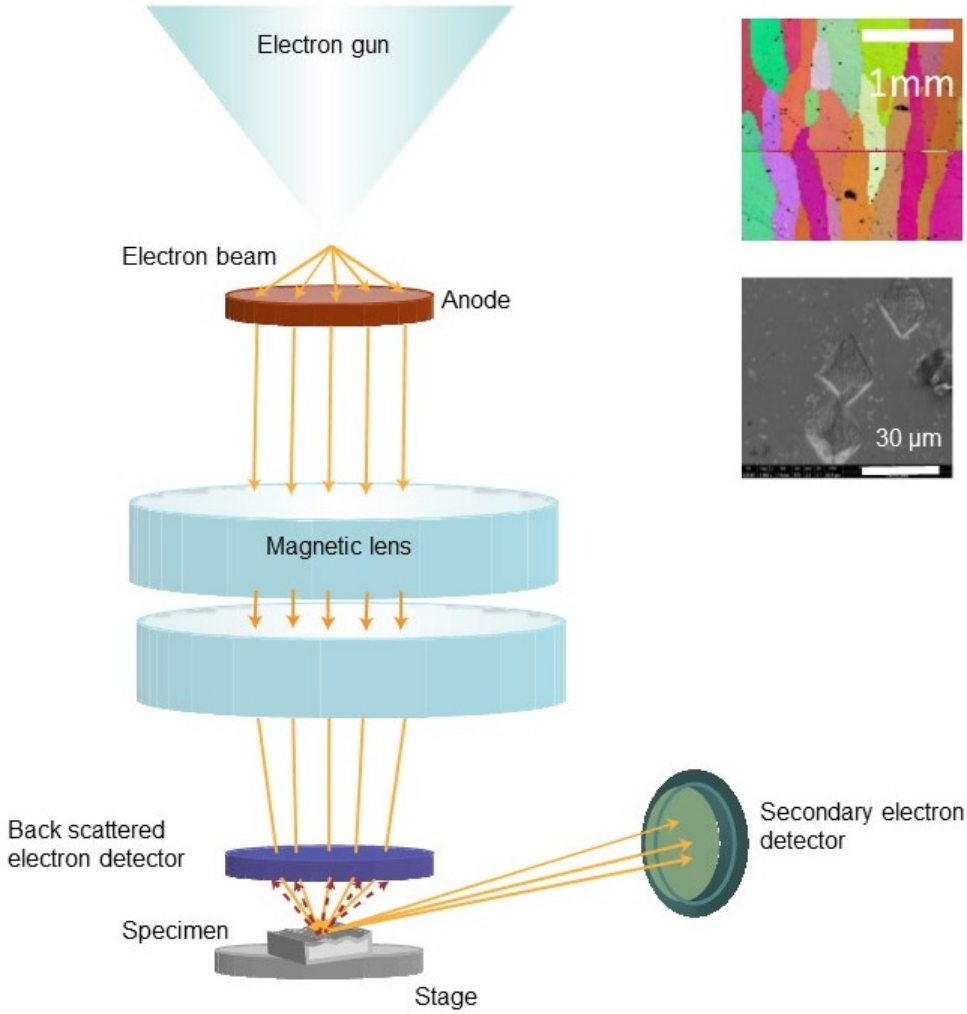

Figure 2.1: ***Schematic of a SEM:*** *the electron beam is focused on the specimen by the condenser lenses and it raster a rectangular area on the surface of the probe. The energy exchange between the surface and the electron beam result in a series of elastic and inelastic scattering that can be detected by different detectors. It is even possible to plot the current absorbed by the specimen as a distribution. To notice is that the condenser lenses are just to focus the beam, the real magnification is from the ratio of ratio of the dimension of the raster on the specimen and the raster on the display device, that is equivalent to say that the magnification is a function of the current supplied.*

the CCD camera. In this configuration, the electron beam is focused onto the surface of a crystalline sample. The electrons enter the sample and some may backscatter see **fig. 2.1**. Escaping electrons may exit near to the Bragg angle and

diffract to form Kikuchi bands which correspond to each of the lattice diffracting crystal planes. If the system geometry is well described, it is possible to relate the bands present in the diffraction pattern to the underlying crystal phase and orientation of the material within the electron interaction volume. Each band can be indexed individually by the Miller indices of the diffracting plane which formed it. In most materials, only three bands/planes which intercept are required to describe a unique solution to the crystal orientation (based upon their interplanar angles) and most commercial systems use look up tables with international crystal data bases to perform indexing. This crystal orientation relates the orientation of each sampled point to a reference crystal orientation. While this 'geometric' description related to the kinematic solution (using the Bragg condition) is very powerful and useful for orientation and texture analysis, it only describes the geometry of the crystalline lattice and ignores many physical processes involved within the diffracting material. To adequately describe finer features within the electron beam scattering pattern (EBSP), one must use a many beam dynamical model (e.g. the variation in band intensities in an experimental pattern does not fit the kinematic solution related to the structure factor.)

SEM pictures were taken in a LEO 1550 VP with an energy of 10 keV. The EBSD mappings were performed using a Hikari EBSD Camera Series. The sample was tilted of 70°, using an energy of 20 keV and step size of 20 μm. The images were then processed with TEAM EBSD Analysis System. Some of the pictures were taken at the USTEM facility in Vienna, working on FEI Quanta 250 FEG with an energy of 10 keV. When talking about metals, SEM and EBSD are fundamental. Most of the literature on corrosion, regards methods analyzing the surface of the specimen with post moretem technique. SEM helps in having a general overview of the corrosion process and the morphology of the surface. EBSD is important, because the orientation of the grain can be a determinant for knowing if that facet of the metal is more prone to corrosion.

2.3 Atomic Force Microscopy

Atomic force microscopy (AFM) is a very-high-resolution type of scanning probe microscopy (SPM) and is mainly used for three different applications: force measurements, imaging, and manipulation of surfaces. The main part of the AFM consists of **1)** a cantilever with a sharp tip (probe), with a radius of curvature on the order of nanometers at its end that is used to scan the specimen surface, **2)** a laser and a 4-quadrat photodetector and **3)** a stack of xyz multi-axis translation piezos as shown in **fig. 2.2**. When the probe approaches the sample surface, forces

between the tip and the sample lead to a deflection of the cantilever according to Hooke's law and it can be used to form an image of the three-dimensional shape (topography) of a sample surface at a high resolution. The surface topography is commonly displayed as a pseudocolor plot.

The following is a more detailed description of how measurements are made in the AFM. The incident laser is focused on the backside of the cantilever and the photodetector collects the reflected laser beam from the cantilever. The angular motion (bending/twisting) of the cantilever, described by the angle θ, can then be translated into the reflected laser shift on photodetector.

$$r_s = L \times sin\theta \tag{2.1}$$

In this equation, L is the traveling distance from the cantilever to the photodetector. This equation can be simplified as followed when L is much greater than r_s

$$r_s = L \times \theta \tag{2.2}$$

From the simplified equation, L is the magnification factor which is able to significantly translate a fine angular motion θ to a measurable shift of a laser reflected onto the detector. The resolving power of the photodetector is therefore determining the spatial resolution of the AFM. To operate the AFM probe as finely as possible, the whole set up is able to translate by a xyz multi-axis piezo stage. In general, the xy axis piezo are used to scan or measure the lateral dimensions of a material surface. With the z axis piezo, the AFM is able to position the sample to the desired position relative to the tip.

The AFM can be operated in a number of modes, depending on the application. In general, possible imaging modes are divided into static (also called contact) modes and a variety of dynamic (non-contact or "tapping") modes where the cantilever is vibrated or oscillated at a given frequency. Nowadays, tapping mode is the most frequently used AFM mode when operating in ambient conditions or in liquids.

In tapping mode, the cantilever is driven to oscillate up and down at or near its resonance frequency. This oscillation is commonly achieved with a small piezo element in the cantilever holder, but other possibilities include an AC magnetic field (with magnetic cantilevers), piezoelectric cantilevers, or periodic heating with a modulated laser beam (Blue Drive^{TM}). In tapping mode, the frequency and amplitude of the driving signal are kept constant, leading to a constant amplitude of the cantilever oscillation as long as there is no drift or interaction with the surface. The interaction of forces acting on the cantilever when the tip comes close to the surface, Van der Waals forces, dipole-dipole interactions, electrostatic forces,

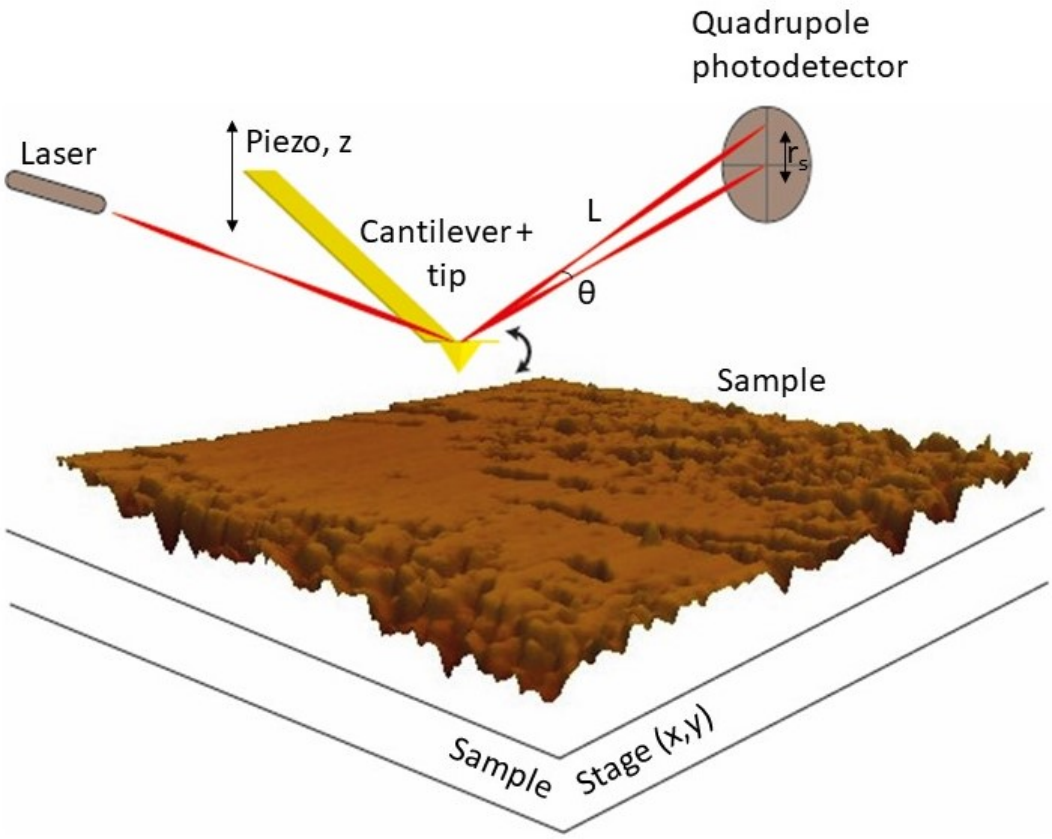

Figure 2.2: ***Principles of AFM:****a sharp tip is used to scan the surface of the sample. When the cantilever bends, the laser is deflected with a small angle θ and can result in a shift of the laserbeam on the quadropole.*

etc. cause the amplitude of the cantilever's oscillation to change (usually decrease) as the tip gets closer to the sample. This amplitude is used as the parameter that goes into the electronic servo that controls the height of the cantilever above the sample. The servo adjusts the height to maintain a set cantilever oscillation amplitude as the cantilever is scanned over the sample. A tapping AFM image is therefore produced by imaging the force of the intermittent contacts of the tip with the sample surface.

Due to the short duration of the applied force in tapping mode, although the peak forces applied can be much higher than those typically used in contact mode, tapping mode generally lessens the damage done to the surface and the tip compared to the amount done in contact mode. When operating in tapping mode, the phase of the cantilever's oscillation with respect to the driving signal can be recorded as well. This signal channel contains information about the energy dissipated by the

cantilever in each oscillation cycle. Samples that contain regions of varying stiffness or with different adhesion properties can give a contrast in this channel that is not visible in the topographic image. Extracting the sample's material properties in a quantitative manner from phase images, however, is often not feasible.

AFM images were recorded in tapping mode with an Asylum Research Cypher AFM ES (environmental scanner), implemented with Blue Drive TM. The measurements were performed with gold coated cantilevers (Arrow-UHF-AuD, Nano World) with a length of 35 μ, resonance frequency of 0.7 -2 MHz. The images were post-processed using plane leveling implemented in the Asylum software package.

2.4 Nano Laue Diffraction

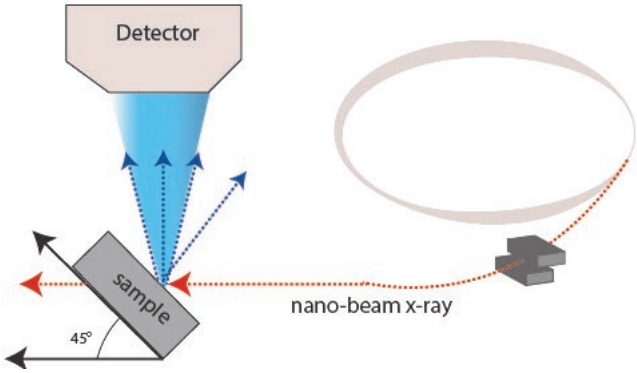

Figure 2.3: ***Schematic of synchrotron setup:****Small x-ray beams are generated by efficient brightness preserving x-ray focusing optics. Laue x-ray microdiffraction is best performed with an x-ray synchrotron source providing a continuous spectrum. Nominal expected spot size on the sample is 100 nm provided by fixed shaped KB mirrors from JTEC corporation. The beam is then arriving at the specimen that is already having a tilted angle of 45° and after collected normally by the detector.*

Synchrotron experiments were performed at TPS Beamline 21A at the National Synchrotron Radiation Research Center (NSRRC), Taiwan. This beamline is dedicated to white or monochromatic beam nano Laue diffraction (nano-LD) for structural analysis (e.g. phase analysis, grain orientations, residual strain, stress, and dislocation mappings). The estimated spatial resolution for such measurements can regularly reach 100 $\times$ 100 $\times$ 50 nm at this beamline. Therefore, the beamline utilizes a pre-shaped Kirkpatrick-Baez mirror pair to focus the polychromatic

X-ray beam with energies ranging from 5 to 30 KeV. This polychromatic X-ray diffraction, that is equivalent to Laue diffraction discovered by Max von Laue in 1912, uses a polychromatic incident beam to collect Laue patterns from a crystalline sample. With this technique, the Bragg condition is satisfied simultaneously for multiple reflections, without the need to rotate the crystal. The sample was navigated inside the chamber with an online real-time scanning electron microscope (SEM) with a spatial resolution of 4 nm, allowing us to correlate the locations examined with other techniques. The station is mounted on an adjustment structure and is positioned on an active vibration isolation table. All measurements were performed in vacuum. The specimen was mounted on a specially designed sample stage with 45° pre-tilted angle relative to the incident X-ray beam.

Diffraction patterns are collected using a high sensitivity pixel array detector (PAD, PILATUS-6M), located at the focus point above the sample (angle resolution better than 0.018 °). Diffraction patterns were analyzed using the XMAS software package [27] to identify the crystal phases, while the mapped images of total intensity, crystal orientation, and peak width were calculated using a LabVIEW-based code.

2.5 X-Ray Photo-electron Spectroscopy

X-ray photo-electron spectroscopy (XPS), is one of the most powerful analysis techniques to reveal the surface material composition and chemical status, which uses X-rays as an excitation source to eject photo-electrons out of the material. The schematic instrumentation principle is shown in **fig. 2.4** Due to the characteristic short mean free path of the photo-electron, XPS is extremely sensitive to analyze the signal from the 5 nm upper-layer of the material, which is the typical thickness of an oxide layer. In a lab based XPS, an anode is normally coated with Al or Mg and it is bombarded with high energy electrons in order to form an X-ray which is then guided into a single crystal to be "monochromated" via Bragg diffraction so to reduce its energy dispersion. After the sample is irradiated by the X-ray, the core electrons in the material receive enough photons of energy to overcome the energy barrier, and finally, the core electrons escape from the material surface. The photoelectrons are then collected and guided to the detector by an electric field across the sample surface and the detector. As a result, the photoelectrons have distinct kinetic energies depending on their core level state. In general, photoelectrons ejected from an atom with higher atomic number, leads to higher kinetic energies of the same core levels due to the lower binding energy of the core and vice versa. To sort out photoelectrons with various kinetic energies,

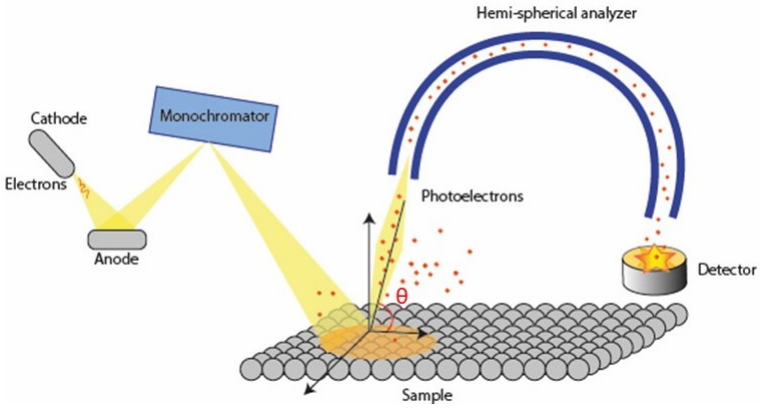

Figure 2.4: ***Principles of XPS:****the specimen is bombarded with high energy electrons so that the core electrons can escape the material surface, to be collected and directed to the detector by an electric field.*

a hemi-spherical analyzer is used to separate photoelectrons with different kinetic energy by applying a non-homogeneous electric field. The fundamental principle of XPS is shown in following equation

$$E_k = E_b + \phi + h\upsilon \tag{2.3}$$

where E_k is the kinetic energy of the photoelectron received by the detector, E_b is the binding energy of the material, ϕ is the work function of the surface and hυ is the X-ray energy. The overall equation describes the conservation of energy in the process of photoelectron generation, where the total energy hυ is equal to the energy required to overcome the binding energy from the atomic core, the work function ϕ which depends on the nearby chemical surrounding and finally, the kinetic energy of the escaped photoelectron.

For chemical analysis, the elemental information can be obtained from the binding energies of individual core electrons, which are characteristic for different atoms. So, the type of atoms can be determined by E_b where E_k can be measured in detector and hυ is a known table value for different X-ray sources. The only uncertainty is the work ϕ function, which also known as the "chemical shift" in XPS studies. Practically, the chemical shift can be estimated by the degree of electronegativity of the atoms. High electronegativity indicates the atom is rich in electron cloud density, which lowers the energy barrier of the escape of core electrons and vice-versa. However, the degree of chemical shift is also related to the type of chemical bonding to neighboring atoms, degree of charge neutralization at the surface, conductivity of the material and the purity of the X-ray source.

2.5.1 Angle Resolved X-ray Photo-electron Spectroscopy (ARXPS)

Although XPS is highly surface sensitive, the embedded bulk signal can still mislead the analysis, especially for thin film studies as it would be for an oxide layer. The mean free path/attenuation length is the distance that particles (photoelectrons in this case) can travel in the material without collision with any other atom cores and it is indicated with D_λ. Along this distance there is no energy loss. D_λ is related to the material properties as the crystal structure and the electron density. is generally larger for electron from low binding energy level, valence bend electron in metals, for example. Unfortunately, not all photoelectrons are generated within the distance D_λ, therefore, in this case, the probability of energy loss will increase exponentially as described in equation 2.4

$$I = I_0 exp(-\Delta_x / D_\lambda) \tag{2.4}$$

Here, I(x) is the photoelectron intensity emitted from depth Δ_x without energy exchange, I_0 is the intensity emitted from the sample surface and D_λ is the attenuation length. For the total photoelectron intensity, there are 65% photoelectrons are escaped within D_λ, 85% within $2\times D_\lambda$, and 95% within $3\times D_\lambda$ based on the integration of equation 2.4 to maximize the surface sensitive signal (typically within D_λ). One strategy is to change the acceptance angle of the photoelectrons by tilting the sample stage. As shown in **fig. 2.4** by changing the tilt angle θ, the probing depth after tilt, d' is related to the non-tilt probing depth d by a factor of $\cos(\theta)$

$$d' = d\cos(\theta) \tag{2.5}$$

Combined with equation 2.4, leads to

$$I = I_0 \exp(-\Delta_d / D_\lambda \cos\theta) \tag{2.6}$$

Now, equation 3.11 relates the photoelectron intensity from depth d to the tilt angle θ, which decreases with increasing tilt angle. Due to the exponential decay, when θ approaches 90° the photoelectron signals from the sample surface are dominant. However, the intensity of the photoelectron signal has maximum flux at the surface normal direction. As the sample stage is tilted the overall intensity massively declines, the signal-to-noise ratio becomes very low when tilt angle is greater than 60°, practically.

All XPS measurements were performed with a Quantum 2000 (Physical Electronics) XPS. Spectra were measured using the implemented high power mode, where photoelectrons are generated by a continuous scanning of a 100×100 μm^2 sized X-ray spot (100 W) over an area of 100×1000 μm^2 in order to minimize X-ray damage to the sample. Pass-energy and scan steps were 22.5 eV and 0.2 eV for high resolution element scans, and 104 eV and 0.4 eV for survey spectra acquisition. To obtain a good signal-to-noise ratio, 15 and 30 sweeps for the C 1s and metal signals, were used respectively. All binding energies are referenced against the adventitious C 1s signal at 284.8 eV.

2.6 Chemicals and surface preparation

High purity sodium chloride was purchased from Sigma Aldrich and a 1 mM solution was prepared with Milli-Q (Millipore) water with a resistivity >18 MΩ·cm and a total organic carbon (TOC) value <2 ppb. The calibration solutions, standard 2A, for ICP-MS were purchased from Agilent Technologies. Optical grade V1 ruby-mica was obtained from S&J Trading Company as sheets of about 20 cm × 20 cm and 2 mm thickness. Surfaces were prepared using 5-10 cm^2 mica sheets with thicknesses ranging from 2 to 5 μm, which were hand-cleaved from raw sheets and used for the experiments [28]. These highly flexible sheets of mica, back-coated with silver, were then glued to cylindrical silica disks of nominal radius of curvature R = 7-15 mm.

2.7 Preparation of sample alloys

Nickel alloys were cast from 99.99 percent pure Elements. B2 ($NiMo_{30}$ plus up to 1% other elements) and C276 ($NiCr_{15}Mo_{16}Fe_6$ plus up to 5% other elements) were obtained as hot rolled sheet material from VDM. Cast ingots or sheet samples were cut into 5x5x5 mm^3 samples. The resulting metal blocks were first ground with sand paper of decreasing grain size (from P80 to P2500), then polished with 0.05μm diamond paste followed by a final polishing with OPS-suspension to a mirror finish. The metal was then cut into pieces, so that the total width was 5mm. The metal blocks were then first ground with sand paper of different grain size (from P80 to P2500), then polished with diamond paste of 0.05μm and and final polishing with OPS-suspension for EBSD preparation.

Part II

Results and Discussion

Chapter 3

Adapting the Surface Force Apparatus technique for corrosion research

In this chapter multiple beam interferometry (MBI), as a technique to study confined zones between two apposing surfaces, is briefly described and reviewed. Implementation of MBI into a transmission mode surface forces apparatus (tSFA) will be described. State-of-the art optical systems in tSFA, as well as typical sources of error, will be reviewed. Finally, improvements to optics and the tSFA technique in general will be described, with a focus on necessities and new aspects for making MBI practical and accurate for studying corrosion in confinement in both tSFA and reflection mode operation.

3.1 Multiple beam interferometry

Multiple beam interferometry is a technique that was pioneered by Tolansky [29]in the 1950 and it allows to give direct measurements of distances across surfaces down to separation distances D below 1 nm. Specifically MBI uses two highly reflective surfaces in cross-cylindrical orientation to each other and a white beam of light that undergoes multiple reflections between them.

Fig. 3.1 shows a schematic of how MBI works. In **fig. 3.1 a** the traditional interferometry is explained; two mica surfaces back coated with semitransparent silver, represents the three layer interferometry. When the light enters the confined space

between the mirrors, there will be multiple reflections. Depending on the distance between the surfaces, specific wavelengths undergo constructive interference and establish standing waves. The white light emerging from the interferometer contains an interference pattern that is then directed to the spectrometer where it is split into fringes of equal chromatic order (FECO).

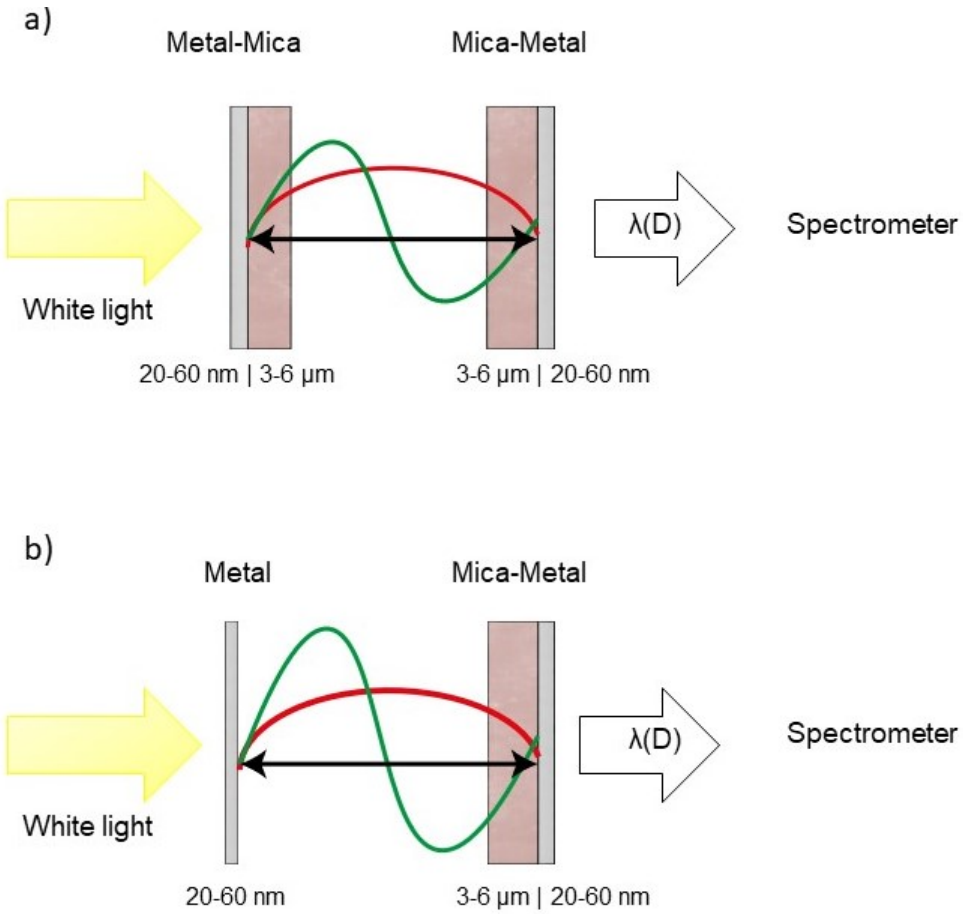

Figure 3.1: ***Schematic of multiple beam interferometry:****a) shows a two layer interferometry and b) a three layer one. The wight light is entering the interferometer and just some specific wavelengths (n*D) will undergo constructive interference. The resulting signal is then directed to a spectrometer.*

Fig. 3.1 b shows a modified interferometry also often used in MBI experiments. It is a two layer interferometry and it is formed by a thin layer of metal and mica back coated with silver.

3.1.1 Absolute distance measurement

The distance measuring between two surfaces of the interferometer is done by relating the wavelength dependent interferometry to the thickness of layers between the two mirrors. **Fig. 3.2** details the interferometer configuration to demonstrate the distance measurement in the interferometer.

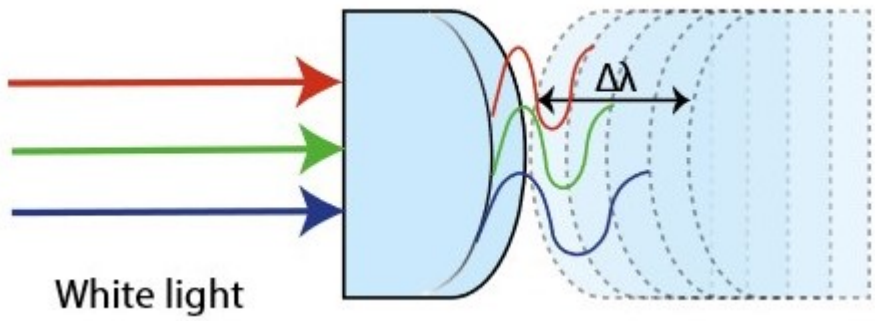

Figure 3.2: ***Relation between the shift of the FECO and the separation distance of the surfaces.***

Experimentally, the constructively interfered light is displayed as a series of parabolic bands (FECO) in a distance (lateral) versus wavelength plot as shown in **fig. 3.3**. A shift of the FECO in the blue direction is seen as a decreasing of separation distance between the two surfaces, while a red shift means an increasing of the separation distance.

The lateral distance axis is equivalent to a line profile of the contact, which provides information on the contact roughness, confined particle size and deformation of the surfaces. The wavelength axis displays the constructive interference of the range we are considering between two mirrors. With increasing the separation between two mirrors, the FECO wavelengths shift. Upon changing the separation distance D, the FECO shift toward lower wavelengths (blue shift) when distance becomes shorter and vice versa. By tracing the shift of the FECO wavelength (peak position of FECO intensity fitting), the change of distance can be calculated with sub-*Ångstrom* resolution. In **fig. 3.3** we can see the FECO approaching the contact position. In a typical configuration the contact is usually flat over a wide lateral range due to adhesive forces as shown in **fig. 3.3c**.

The distance, D, can be measured from the wavelengths of two adjacent FECO recorded in contact D_0 (λ_n^C and λ_{n-1}^C) and at a certain distance D (λ_n^D and λ_{n-1}^D), considering a simplified interferometer (similar thickness of transparent layer and

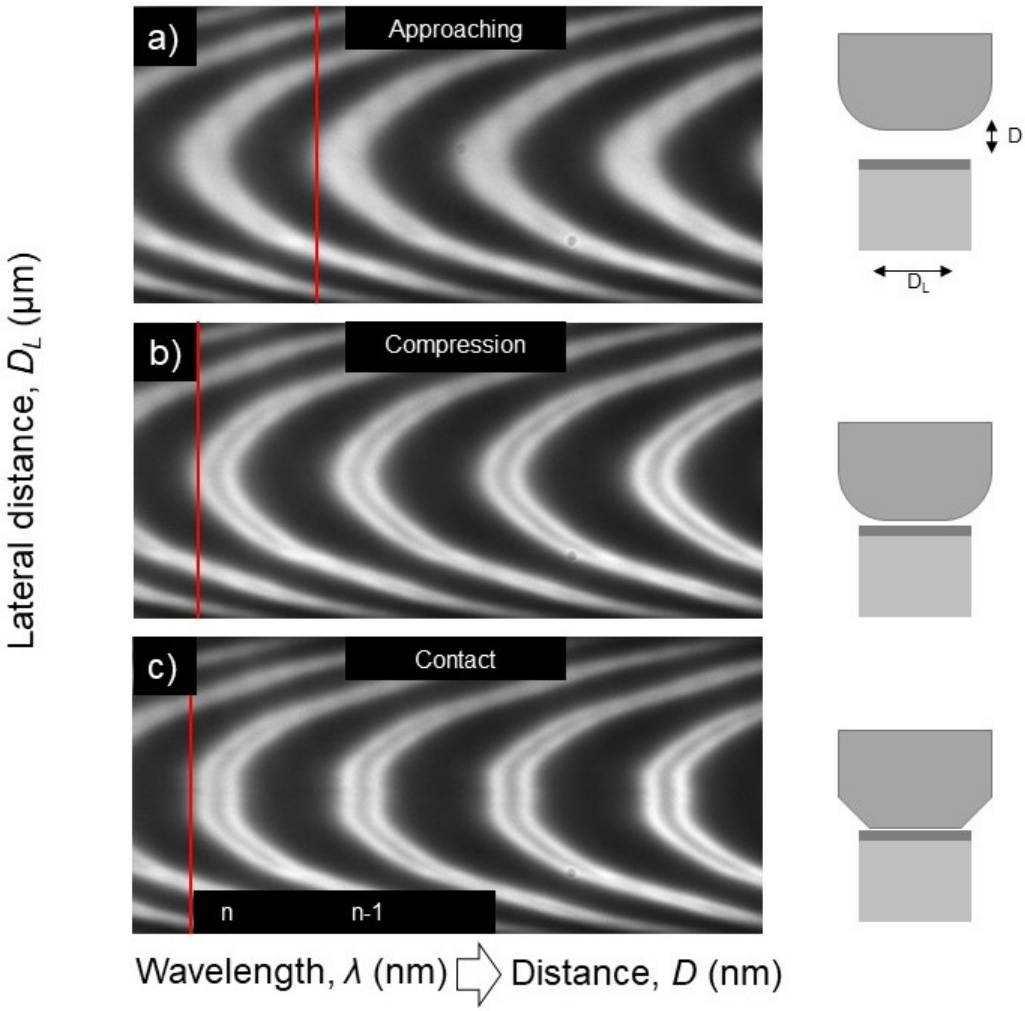

Figure 3.3: ***FECOs during the approach of two surfaces:*** *the blue line represents the front*

mirror ones) as in the following equation for a three layers interferometer as in **fig. 3.1a** and two layers one **fig. 3.1b**.

$$\text{3-Layer: } \tan\left[D\frac{2\pi\mu_{fl}}{\lambda_n^D}\right] = \frac{2\left(\frac{\mu_{ts}}{\mu_{fl}}\right)\sin\left[\frac{1-\lambda_n^C/\lambda_n^D}{1-\lambda_n^C/\lambda_{n-1}^C}\pi\right]}{\left(1+\left(\frac{\mu_{ts}}{\mu_{fl}}\right)^2\right)\cos\left[\frac{1-\lambda_n^C/\lambda_n^D}{1-\lambda_n^C/\lambda_{n-1}^C}\pi\right] \pm \left(\left(\frac{\mu_{ts}}{\mu_{fl}}\right)^2 - 1\right)} \quad (3.1)$$

with the plus sign referring to odd order FECO, and the minus sign to even

order FECO. Even and odd FECO have either an amplitude maximum or a node with minimal amplitude close to or at the center of the interferometer cavity. The refractive indices of the confining transparent surfaces μ_{ts} and the separating (often) fluid medium μ_{fl} are needed to within an accuracy of ± 0.0002 to allow for an accurate absolute measurement. Hence, with **equation 3.1** it is possible to simultaneously measure both the refractive index of the fluid medium μ_{fl} as well as distances D by (1) first recording the reference wavelengths of two adjacent FECO λ_n^C and λ_{n-1}^C (red shifted FECO) in contact. Afterwards, (2) the thickness $T = D$ of any layer confined between the two apposing surfaces and its refractive index can be evaluated by recording the wavelengths λ_n^D and λ_{n-1}^D.

However, for a 2-layer interferometer it is not possible to independently measure refractive index and distance using these analytical equations as both even and odd FECO behave similarly upon change of μ_{fl}.

$$\text{2-Layer:} D = \frac{\left(\frac{\lambda_n^C}{\lambda_n^C - \lambda_{n-1}^C}\right)\left(\lambda_n^D - \lambda_n^C\right)\mu_{ts}}{2\left(\mu_{fl}\right)^2} \text{for even } \underline{\textbf{and}} \text{ odd FECO} \tag{3.2}$$

3.2 Previous versions of the Surface Forces Apparatus

Historically the typical contact geometry between the two surfaces was crossed cylinders, recently different types of surface shapes were investigated such as flat on cylinder (see chapter 5) which, however require extensive alignment and preparation effort but extended the application of SFA to a broader range of materials.

The surface forces apparatus (SFA) was developed during the 20th century and has been used for many years to measure the physical forces between surfaces. Over the last 40 years, J.N. Israelachvili [30] and numerous co-workers continued to further refine the first SFA design, in order to adapt it to different applications and as of now a number of specialized setups [31], were developed by his group. Even though a lot of changes were done, the principle remained the same.

As illustrated in **fig. 3.4**, an SFA is composed by three major parts: **1)** a white light source, **2)** an interferometer of two opposing reflective surfaces and **3)**a spectrometer.

Early versions of the SFA experiment by Tabor [32] and Israelachvili consisted of a

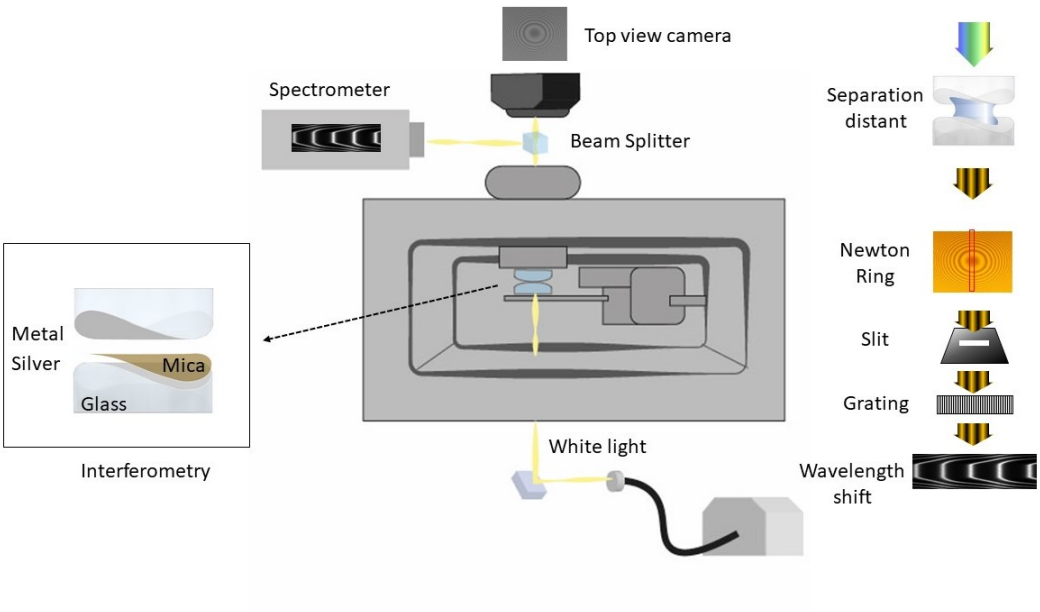

Figure 3.4: ***Overview of the most important parts of an SFA:*** *a) enlargement of the interferometer; b) general setup of an SFA; c) relation between FECO, newton Ring and position of the slit.*

simple apparatus, where one of the surfaces was supported by a short metal spring and the other surface was approached with the help of a piezoelectric transducer, this version allowed to measure critical separations where two surfaces jumped together. The first refinement by Adams and Israelachvili [33] using stainless 316 steel, Teflon and Delrin as materials for a measurement chamber enabled operations in fluids.

A differential spring mechanism was introduced to reduce motor motions to 1 nm accuracy, while piezo transducers were used for fine motions and sample vibrations. These adjustments led to the creation of SFA Mark I, which was further refined by introducing double cantilever springs for preventing torsional sample movements during operation, and additional attachments were developed to enable more interfacial phenomena to be studied. These include a friction device for applying lateral motions between the surfaces [30]. In this so-called Mark II, friction forces were detected using strain gauges [34]. As more and more complex fluids were studied using the completely refined SFA technique, dubbed Mark III [35], was developed for simplified operations. Specifically, the chamber was significantly smaller, which also simplified cleaning procedures for the apparatus. The last major upgrade of the original SFA by the Israelachvili group was described

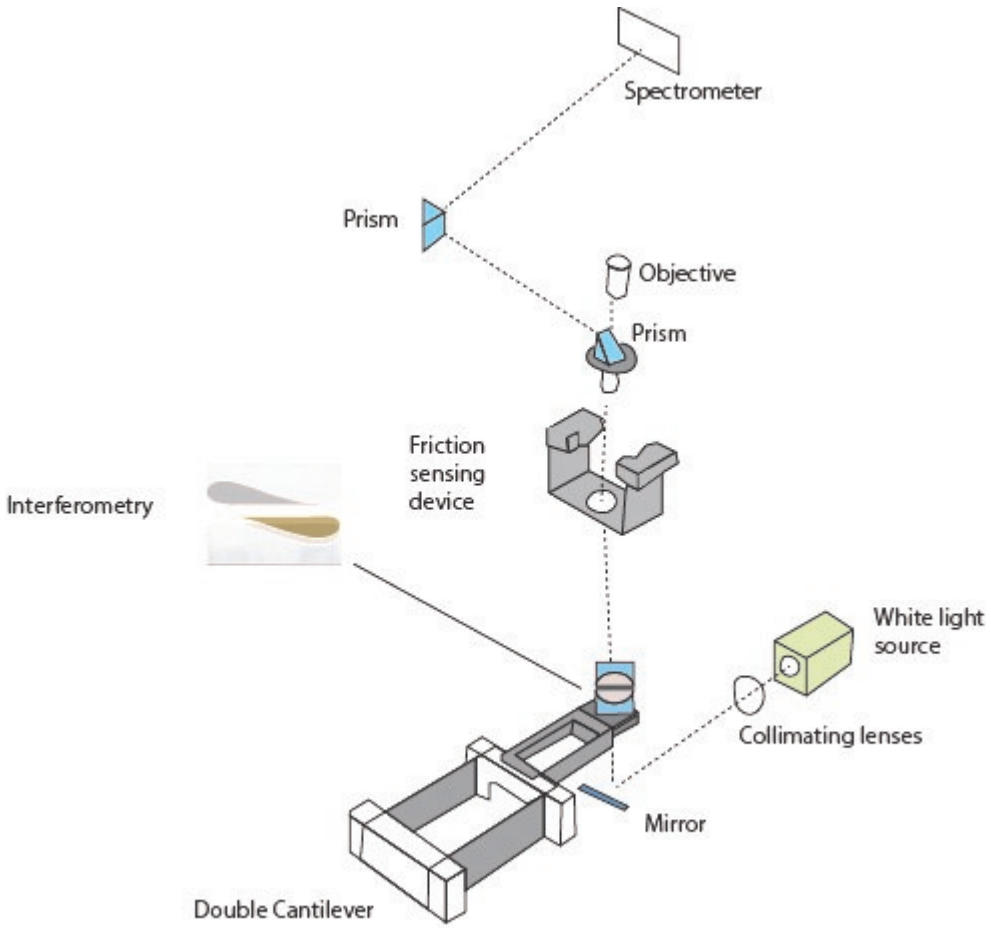

Figure 3.5: ***Traditional SFA setup:*** *shows the classical version of the SFA 2000, where every element in the optical system is movable.*

in 2010 [31]. This so-called SFA 2000 **fig.3.5**, further simplified operations and a number of different attachments were developed.

The most elaborate alternative development of an SFA experiment was described by M. Heuberger in a series of papers in the early 2000s. He analyzed sources or error and drift in existing SFA setups, and introduced what is now called the extended SFA. Apart from an ideally drift-minimized design, this is the first SFA with remote controlled operations.

In addition, Heuberger introduced the so-called fast spectral correlation interferometry using the transfer matrix method [36] for simulating peak positions of interference fringes [37]. A fast correlation of measured and simulated peak positions

allows distances to be directly extracted with very fast processing rates.

This SFA data analysis relies on a full treatment of the optical cavity, providing accurate distance estimates from 0 to 10s of μm. Also, the analysis of refractive indices of confined thin films is considerably more precise using the transfer matrix method. Notable other SFA developments include the first electrochemical SFA by J.Frechette *et al.*[38], an apparatus based on capacitive sensors by Tonck and coworkers [39]. J. Klein developed a smaller version of the SFA, with a focus on minimizing the number of components in contact with the fluid. The fluid chamber of this SFA, dubbed the Surface Forces Balance (SFB), is made of glass for improving cleaning procedures [40].

3.3 Opportunities for, sources of systematic and observational errors of the SFA technique

Before going through the changes made by our group in the SFA, it is important to understand why those changes were needed. It is very instructive and important to reconsider potential sources of error in any experimental technique in order to try and minimize, or at least keep such errors in mind when interpreting data. For SFA operations a number of sources of systematic errors were discussed extensively by M. Heuberger *et al.*[41]. For example, some of the errors were attributed to thermal drift, as a possible variation of the surface separation due to a change in temperature of the SFA. Though, it is not possible to completely avoid any thermal drift, but it has to be taken into consideration in the material selection for the different components. Another possible source of error could be derived from the optical system and/or the analysis.

3.3.1 Potential errors of the optical system

Deviations of the optical path from an ideal perpendicular alignment can lead to artificial shifts of the measured thicknesses and distances, in particular, if contact points are changed during an experiment. Sharp fringes are obtained when the light beam is passing normally through the surfaces at their point of maximum vicinity; if not, the fringes will result to be blurred and shifted to shorter wavelengths. If we want to ensure that the calibration with D_0 remains value along the whole experiment, θ hast to be equal to zero. **Fig. 3.9** shows how a misalignment could lead to a wrong interpretation of the contact position, for a mathematical explanation see figure caption.

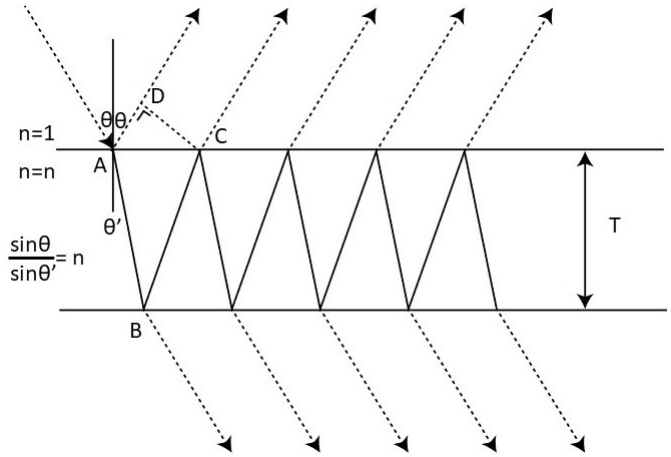

Figure 3.6: ***Error in optics alignment:*** *the path length for each reflection is 2Tn for θ=0 and '2AB-AD' for θ>0, where n is the refractive index of the sheet of thickness T. By Snell's law sin θ=nθ' so that AD = AC sin θ=2Ttanθ'=2Tnsin^2 θ'/cos θ', and 2AB.n=2Tn/cosθ'. Thus, 2AB.n-AD="Tn(1-sin^2 θ')/cosθ'="Tncos θ'. Since cos θ'<1 for θ'>0, the path length for interference is seen to decrease as θ'(and therefore θ) increase above zero.*

Another systematic error is the variation of the absolute refractive index of mica and the birefringence, which may be significantly different from sheet to sheet and batch to batch. As we show before, modeling and analyzing FECO data can directly fit birefringence, but absolute refractive indices of mica have to be obtained from reference measurements and may be more or less accurate. As a result, absolute distances can have some uncertainty, while relative changes will always be accurate.

Reference errors An important consideration is that the absolute distance is measured between two mirrors in SFA. The convenient reference of the surface/surface contact in dry nitrogen is also absolute as such, yet whether this is the actual surface to surface distance is not immediately clear[42, 43]. For instance, it is may not be possible to desorb all water molecules from a surface at ambient pressures and temperatures as used in SFA experiments. As such, this adsorbed water is usually included in the distance measurement, but it is rarely addressed. In addition, organic carbon contaminants are always present on surfaces prepared at ambient conditions [44] which can add another layer of uncertainty to the absolute surface/surface distance. While such layers are in fact trackable, considering them in the interpretation of data is not always straightforward. Hence, a final uncertainty on the absolute distance of one contaminant layer is often present in

the interpretation of the data, and should be carefully ruled out and/or considered. For instance, negative distance shifts of 3-4 Angstrom can occur, indicating that a contaminant layer was desorbed (often into the used medium) after referencing surface/surface distances [43].

Motor linearity A disadvantage of the (very sensitive) force evaluation via wavelength shifts is that the force is not measured independent from the distance measurement. Based on the acquired separation distance from tracking the motion of FECOs, the force is calculated by using various methods of constant approach speed or constant displacement. Assuming that an apparatus is perfectly moving at constant speed, the variation of observed motion and applied motion can be converted into a normal force and distance characteristic by calibrating the linear motion using the distance measurement in a regime were no force is applied and by then simply applying Hooke's Law to convert any deviations into an interacting force. However, it is rather tricky to ensure that the applied motion is correct in a real system that is subject to thermal noise. For example, non-linearities of the motion system can translate into an observational error. Specifically, it is not the actual motion that may be non-linear (an experienced user would easily spot any relevant non-linearities of a motion system), but thermal drift of the systems often adds an unknown variation to the motion, which may not always be detected or which may not be prevented. Small variations in the range of 0.1-0.5 degree of the temperature °C around a set point in a temperature controlled lab will directly translate into - often oscillating - temperature and hence "apparently non-ideal" motion profiles. This may become a problem for very slow measurements.

Evaluation of D / interferometry The **equations 3.1** and **3.2** seen above, give significant deviation from the full result at separations larger than 30-60 nm. As a result of the analysis, such systematic deviations may be interpreted as artificial weak forces (up to 2-5 μN). Due to simplifications, the analysis with these equations can add a significant uncertainty to the distance measurement, as it may introduce "apparent" but artificial distance changes which can amount to 5-10% of the measured values.

Also, in SFA analysis using **equations 3.1** and **3.2**, the refractive index of a confined medium is treated as constant and wavelength independent. However, it is clear and was often shown, that this is not the case. As such, analysis with simplified equations may often introduce an error in absolute distance due to not taking the variation of the refractive index into account. This can be circumvented if a full analysis using the wavelength dependent refractive indices is applied.

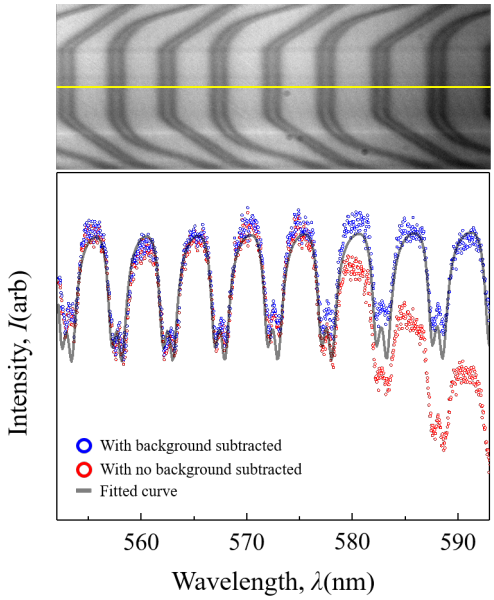

Figure 3.7: ***Background subtraction:*** *the figure shows the different interpretation according if the light in the background is considered or not.*

Another noteworthy issue is the intensity-wavelength profile of the light source. In this application, a mounted white LED light source (ThorLab, 800 mW, MCWHL5) is used due to its stable intensity profile in the 500-600 nm wavelength window and low intensity in the red-infrared region, which stabilizes the interferometer from thermal drift compared to a normal halogen lamp/filament. Additionally, the spatial distribution of the intensity of light emitted from a LED is more homogeneous than the light emitted from a filament, which reduces the complexity of imaging analysis by providing a uniform background in the CCD camera. However, every light source has its characteristic intensity-wavelength profile, which contributes a non-negligible error in data analysis, and therefore, proper background sampling is very crucial. Similar to other optical methods, sampling a reference light path can actually solve the FECO data analysis error which is generated from the intensity-wavelength profile of the light source. In **fig. 3.8** the green paths are the reference light path which is split from the light source directly by a BSC and guided to the spectrometer via another optical path as shown with the green indication line. The BSCs used in transmission mode and reflection mode are different. In transmission mode, the incident light intensity should be maximized to obtain good FECO signal/noise(S/N) ratio, however in reflection mode, strong incident light will be reflected as background signal which reduces the S/N ratio instead. Therefore, 10/90 and 90/10 BSCs are used for transmission and reflection mode, respectively, to optimize the FECO quality.

Although the output intensity of the reference white lights are not equal, it does not affect the outcome since only the relative intensities over wavelengths are calculated to subtract the background instead of absolute intensity. The influence of background subtraction is shown in **fig. 3.7**.

3.4 New optical system for SFA measurements

If on one side, a lot of effort was invested in order to improve the design of the apparatus over the past years, on the other side, very little was done in order to improve the optic system. This is however crucial for establishing MBI in an SFA as a tool for monitoring corrosive processes in confined geometries. **Fig. 3.5** shows the traditional optical path of an SFA experiments,that was composed of a white light source, a SFA chamber, a free standing microscope and one or two prisms to guide the light path emerging from the microscope into a spectrometer. The alignment of the prisms was crucial in order to guide the beam into the spectrometer. However, this procedure can introduce small but often significant deviations from a perpendicular light path. Specifically if a contact position is changed within an experiment, realignment of the path may lead to artificial shifts of the recorded FECO and hence distance. In addition, this optical layout is not equipped with possibilities to simultaneously record both optical and FECO paths. Usually the optical path is only used during rough alignment and contact establishing, while FECO are used for fine alignment and recording of FECO shifts, making it extremely tedious and imprecise to work with corrosion experiments. This classical system has the following drawback for working with corrosive interfaces:

- no background is measured
- optical alignment is tedious (ideal perpendicularity is hard to ensure)
- no permanent top view camera installed
- no reflection mode operation possible without complete update of optical path

In order to overcome these problems, new SFA optics were implemented as follows.

In the improved setup, shown in **fig. 3.8**, we introduced a new idea of the optical system based on one easy step as shown in **fig. 3.9: moving the Newton's ring (NR) into a well-aligned optical path**. The optical path is fixed, by a standard cage system as illustrated in **fig. 3.8**, while the SFA chamber, since an additional 2 axis-stage (XY) was implemented, can freely move so that any established contact

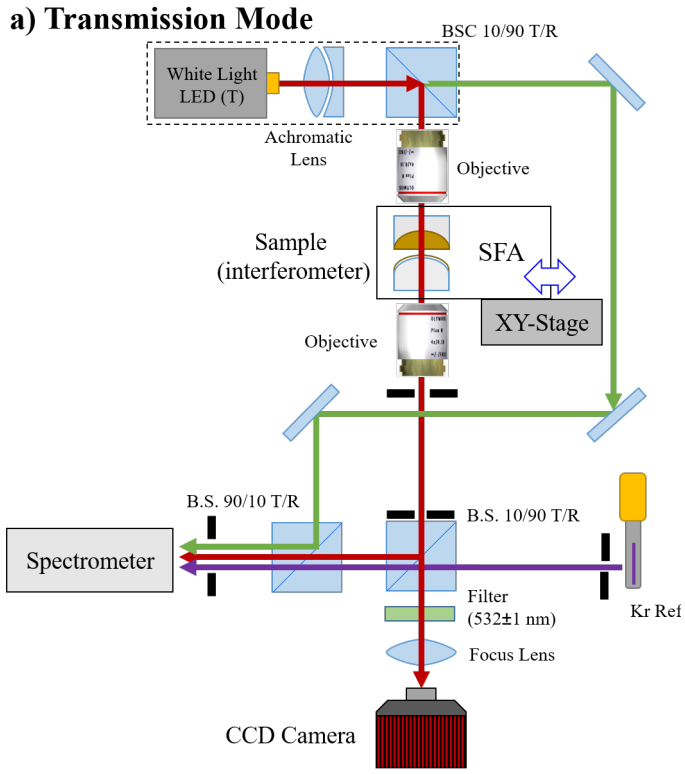

Figure 3.8: ***Suggested improved optics in SFA:*** *in this setup all the optics element are fixed, and the only part that is movable is the interferometer.*

can be translated into an optimized optical path. This procedure greatly reduces any artificial shifts due to misalignment of the optical path. In addition, we use using a fixed optical rail system with beam splitters instead of prisms, to establish the optics. This allows to include additional paths such as a simultaneous optical and FECO analysis. In this setup the NR is found through the help of a CCD camera. In order to align the optics properly, first, a NR is found and positioned in the middle of the CCD camera. All the other optics, including the spectrometer, are then aligned accordingly in order to enhance the contrast of the fringes of equal chromatic order (FECO).

Regarding the corrosion experiments, this is a crucial point: while from the FECO we can derive information regarding the thickness of the electrolyte, the roughness inside the confinement and be sure that the crevice is well established, the top view camera, gives us information regarding the size of the confinement, how is corrosion proceeding and how deep it goes.

On the same line, the spectrometer is aligned with the CCD camera via a 10/90

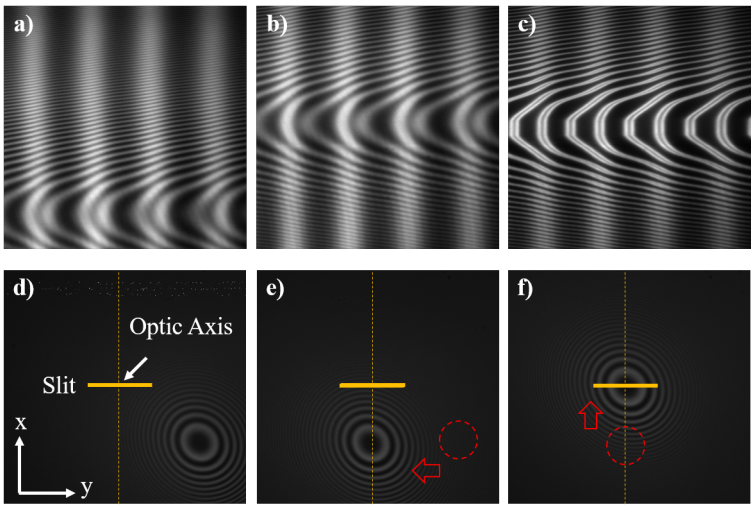

*Figure 3.9: Relationship between **a-c** fringes of equal chromatic order (FECO) and **d-f** Newton ring (NR) during the alignment process. The NR part represents where the contact is in relation to the slit for each of the resultant spectrometer images.*

(T/R) beam splitter cube (BSC) which guides 90 % of intensity to the spectrometer and 10 % to the CCD camera. The BSC is relevant in order to control the amount of light that is distributed through the optics to have a better resolution and depending on the scope of the measurements, it could be changed to different T/R ratios according to different experimental requirements, for instance, fluorescence.

Miss-alignment often results in the emergence of pseudo forces, which leads to wrong interpretations of the interfacial interactions. It is important to consider that the FECO can be measured with an accuracy of sub-picometer , while the lateral resolution remains depending on the microscope and the resolution used.

Fig. 3.9 shows the relationship between the NR image (**fig.3.9d-f**) from the CCD camera with projection of slit and optic axis, and FECO images (**3.9a-c**) from the spectrometer of a contacted mica-mica geometry in air as a guideline of alignment procedure. Here, the slit position is determined at the beginning of optic's alignment. While the NR is far from the optical axis as shown in **3.9a** and **3.9d**, the FECO are usually away from the spectrometer center and out of focus. Relocation can be carefully made by using the 2 axis-stage underneath the SFA (see **fig. 3.8**). Here, the x-axis and y-axis have different functions in terms of the alignment procedure: **Translation along y axis and x axis are equal to moving FECO pattern up/down and contact search, respectively**. From **fig. 3.9a**, **d** to **3b**, **e**, the NR is translated along the y direction towards the left-

hand side, which is equal to translating the FECO upwards to position the FECO pattern at the center of the spectrometer slit. Afterwards, motion from **fig. 3.9b**, **e** to **c**, **f** surveys the confinement geometry to find the contact position. As shown from **fig. 3.9b** to **c**, flattened contact was revealed when the center of the NR moved into the projection of the slit along the x direction. This step is the most important part for establishing a particle free contact for proper interfacial force measurements.

In general for mica/air/mica geometry, the Van der Waals (VdW) force is dominant when the surfaces are flat and particle free. During the approach of two mica surfaces in air, a strong attractive force is expected, which will result in a fast jump-in and contact flattening. After contact flattening, a higher attractive force due to a higher contact area is typically observed during the separation of the two mica surfaces. If the surfaces are contaminated by particles, the VdW attractive force will be greatly reduced, which is a very important indication to check the contact quality.

3.4.1 Multiple beam interferometry in corrosion

Now that we have seen how multiple beam is working, we can focus on how it helps us in studying corrosion. Here a three layer interferometer is considered, where the nickel will be the electrochemical active mirror and the silver the electrochemical inactive one. **Fig. 3.10** shows how FECO are affected during the dissolution process. **Fig. 3.10 a)** and **fig. 3.10 b)** represents the FECO before and during the corrosion process. The x-axis is represented always by the wavelength while the y-axis represents the lateral position (the position of the slit) and it can be divided in 2 sections: the confined area and the crevice mouth. **Fig. 3.10** shows a 2 layer system where the FECO are recorded between a thin layer of nickel and the transparent crevice mica back coated silver. When corrosion occurs there are two main things to monitor: one is the ΔD in the mirror shift and the other one the ΔI in the intensity - increase of brightness of the FECO-. **Fig. 3.10 c** shows the variation in the mirror shift - the distance between the contact position and a given distance-, equivalent to the distance between the nickel layer and the silver.

When the process of dissolution begins, if the pits start to form at the slit position, we will have a shift of the FECO and so in the mirror shift, as the distance between the two surfaces would increase at that specific point due to the dissolution of the metal. Plus, the formation of the pit, would make the layer of the metal thinner and so, more light would pass through the metal, and the intensity of light would increase. It is possible to notice that in **fig. 3.10**, three different point are highlighted. The red line, where there is the formation of a pit going through all

the surface, the green line, where nothing is happening, but still a variation of the mirror shift is observed due to the neighbouring pitting, but no change in the intensity, and finally the blue section where the pitting just started to form. Here, I would like to underline, that the position of the slit is very crucial. If the pitting is happening on the surface, but not in the exact position of the slit, no change in the FECO will be observed.

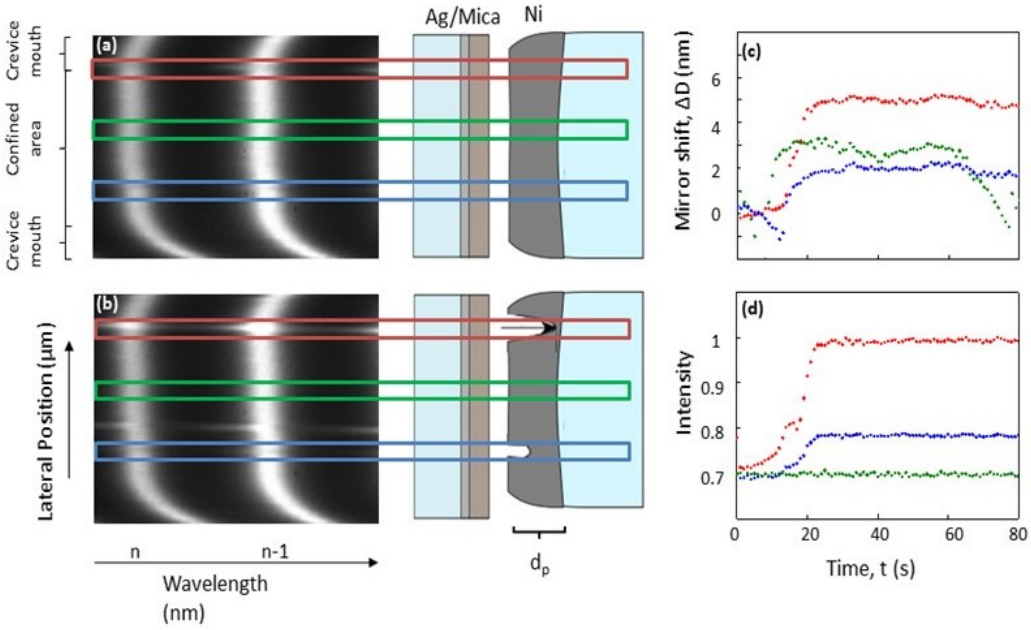

Figure 3.10: ***FECO variation during the dissolution process:*** *a) before corrosion b) after corrosion c) variation of the mirror shift with time and d) variation of the intensity with time*

3.5 SFA in reflection mode.

Fig. 3.11 shows a schematic of the optical path in reflection mode. Although the study in transmission mode, was already giving us a total new outlook about the corrosion process in confinement, a necessity to move from the thin film to real metal was requested. The influencing breakthrough of the new optics system is the integration of reflection mode SFA (rSFA). Similar to the transmission mode SFA (tSFA), the reflection mode surface force apparatus (rSFA) measures the gap geometry of the confined region of a non-transparent sample based on interferometry. As the name rSFA indicates, the reflected/interfered light from the confined

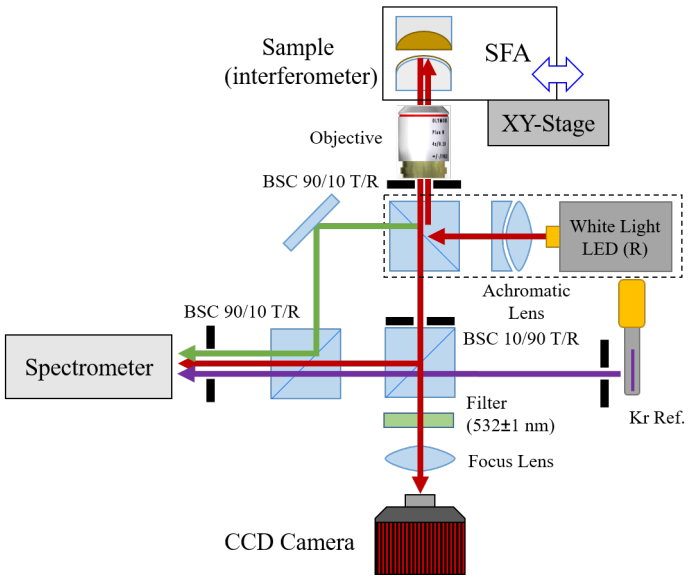

Figure 3.11: Schematic of optical path of ***b)****reflection mode.The white light path is indicate by the red line. After the first beam splitter part of the light is directed through the optics path and the other part is directly lead to the spectrometer in order to have it as a reference for the background (green line).The violet line indicates the reference light from a mercury lamp being guided to the spectrometer for calibration purposes. At the center of the optical path, is the interferometry, where the two surfaces are in cross cylindrical section and they are set on a x-Y stage plus a goniometer.*

sample interface is collected to characterize the gap size, roughness and electrochemical behavior in e.g. corrosion science. The rSFA is first invented by R. Horn [45] with the interferometer consisting of a drop of mercury and a flat back silvered mica surface. Due to the optic's arrangement for reflection mode, the observed fringes of equal chromatic order (FECO) are constructive interference that shows as reduced brightness because during the bouncing back and forward in the cavity the light is absorbed as well, this hence reduces the intensity leading to FECO which look as the inverse of the transmission mode (bright fringes). The general principle of operating SFA in reflection mode is using a 90/10 (T/R) beamsplitter, which reflects only 10 % of incident achromatic white light to the interferometer (mica/sample). Light is then focused onto the sample surface to generate an interference pattern. Afterwards, the same objective simultaneously collects the interfered light from the same focal plane, and directs the interfered light to pass the same beamsplitter with 90 % transmission efficiency towards another beamsplitter with 10/90 T/R efficiency which splits 10 % to the CCD camera for Newton's rings observation and 90% to the spectrometer to analyze the Fringes of Equal Chromatic Order (FECO). Unlike tSFA which requires high incident white light

intensity to achieve sufficient signal-to-noise ratio of the interference pattern, the incident light intensity of rSFA is much lower in order to prevent the saturation of the background which is mainly contributed from the reflected incident light from the back silvered mirror. Good contrast could be obtained by carefully tuning the incident light intensity and sample orientation, such as tilt and angle of contact geometry. Moreover, the contact searching in rSFA is much easier than in tSFA. During the contact searching, the reflected incident light forms a parabolic band across the image, which shows the orientation of the apex of the back silvered disk. In a well aligned geometry, the contact position can always be found within this band (see **fig. 3.12**).

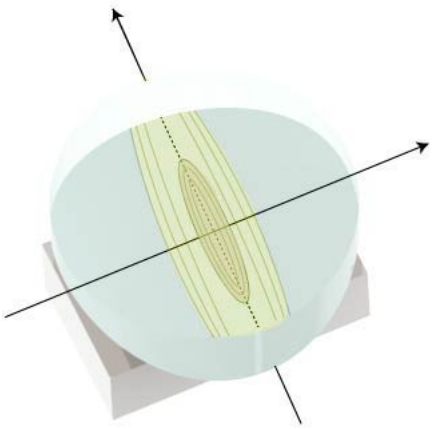

Figure 3.12: Schematic of the interference pattern in reflection mode. The parabolic band where it is expected the interference pattern to be seen is highlighted.

Ideally, the optimum sample alignment is when the surface normal of the sample is perfectly aligned to the optical axis of the objective. For this purpose, a mini goniometer is built in together with a set of XY- strain gauge to fine tune the tilt angle and contact position of the sample orientation. Afterwards, the optimum alignment condition can be achieved by maximizing the intensity of the reflected light from the sample surface by fine tuning the tilt angle, which indicates both the incident light and the reflected light are in the same optical axis. After the correct sample orientation is determined, a counter disk with back silvered mica surface is then introduced to construct the interferometer for crevice corrosion tests.

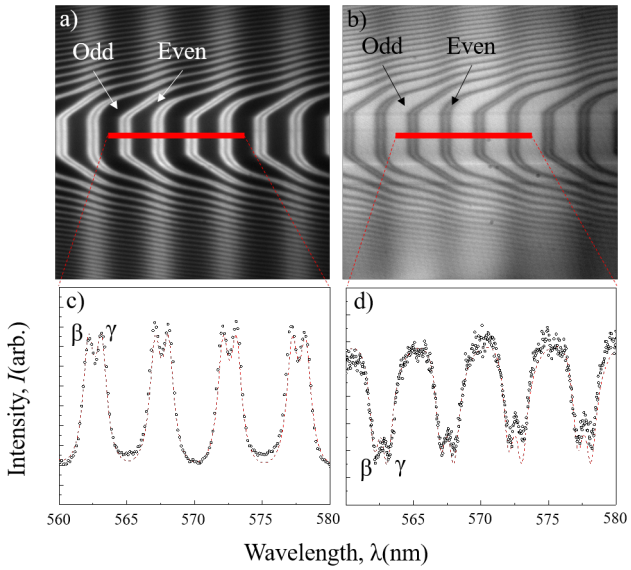

Figure 3.13: FECO obtained from the same mica-mica (40 nm Ag mirror) dry contact geometry either using: ***a)****transmission mode and* ***b)****reflection mode. The spectra at the region marked in red are fitted by Multiple Matrix Methods (MMM).* β *and* γ *represent the bifringes properties of the mica and therefore we observe the splitting during the analysis.*

Plus, when running a reflection mode SFA experiments, it is needed to be taken in consideration that both surface have to be able to reflect light. However, due to the different optical properties such us low NR contrast, high system background and limited view in the interferometer, reflection mode has not been well studied so far .

3.6 Interferometry calculation of transmission/ reflection mode

The optical design, as shown in **fig. 3.13**, has a mechanism to switch the transmission and reflection mode module based on individual experiment requirements. Here, a mica/air/mica contact is used as an example to compare the FECO quality of these two modes in a same contact geometry without doing any other optimization but switching the light source and reducing the light intensity from transmission to reflection mode. Mica thickness (2 layers) is then calculated by SFA Explorer (home made software based on 4×4 multiple matrix method) [46] from acquired FECO images. The results show that the calculated mica thickness in transmission/reflection mode are 9919.07/9917.42 nm (less than 0.2 % error), which precisely correlates the reflection mode measurement to the transmission mode with all spectrum features.

3.7 SFA in corrosion

Crevice corrosion experiments were performed in a confined geometry generated in a newly designed tSFA/ rSFA. The setup and its optics were home build using components from Thorlabs, including a sCMOS camera (2.1 Megapixel), a laser line filter 532 ± 1 nm, two beam splitters (10/90 and 90/10), objective with a 4x magnitude, an Andor spectrometer coupled with an IXON 3 EMCCD camera, and a MWWHL4 LED as white light source (WL).

Fig. 3.14a shows the typical confining surface layout used as crevice former. Specifically, a molecularly-smooth, back-silvered muscovite mica surface is glued on a glass cylinder. Using the layered-silicate muscovite mica provides a molecularly smooth and transparent crevice former that can be produced with very small thickness by manual cleavage[28]. The silver coating at the back-side is semi-transparent (40 nm silver thickness) and provides the mirror surface for generating an interferometer. As shown in **fig. 3.14b** and **fig. 3.14c**, the apposing surface

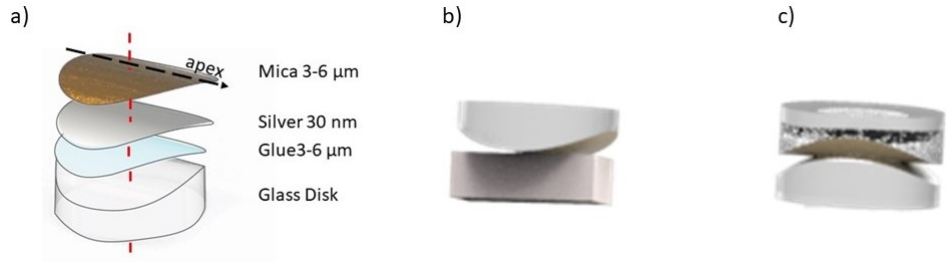

Figure 3.14: ***Crevice former and crevice configuration in SFA:****a) Typical crevice former b) crevice configuration in reflection mode c) crevice configuration in transmission mode*

could be both a **b** metal blocks (Ni, alloy) with 5 mm height and 5 mm diameter or a **c**thin film metal layer deposited directly on a glass, mounted on the top sample holder with their fine polished surface apposing the crevice former. With these two mirrors, a 2-layer interferometer is generated. Any changes in the separation distance between the Ag and the metal mirror due to, e.g., ingress of water, or shift of the metal mirror surface by corrosion (conversion into oxide or dissolution), can be tracked with time by analyzing standing waves in the optical cavity that is generated. Further details on white light interferometry can be found here[47]. Once corrosion occurs, clear changes in the wavelength and hence light intensity of the Newton's rings (NRs) can be detected with an optical microscope of 4-20X magnitude by projecting the image on a CCD camera and the spectrometer slit. In **fig. 3.15** a comparison between the observation of the corrosion process in transmission and reflection mode is shown. When performing a SFA experiment, the position of the mirrors and how the light travels through them it is a sign of how intense the constructive interference will be. In a) we can see a schematic of the light path, according to the mirror thickness and their arrangements: so, in the transmission mode, the light goes through the first mirror and it is reflected back from the second one, creating an interferometry between the two surfaces, and just specific multiple of λ would allow the further passage of the light. In the reflection mode, the light once is passed through the first mirror, is partially absorbed and partially reflected back to the first mirror. Fig b) shows the different in FECO in transmission and reflection mode. If in the transmission mode, the only part visible are the FECO while, in the reflection mode, it is exactly the opposite; one observe a strong background and what visualize is the absence of FECO. In c) this difference is quite appreciable. So, while during the corrosion process in tSFA, where the light intensity increased due to the formation of the pits, on the contrary, formation of pits on bulk metal defects the light in rSFA which decreases the light intensity because of scattering in pits. d) shows the electrochemistry difference

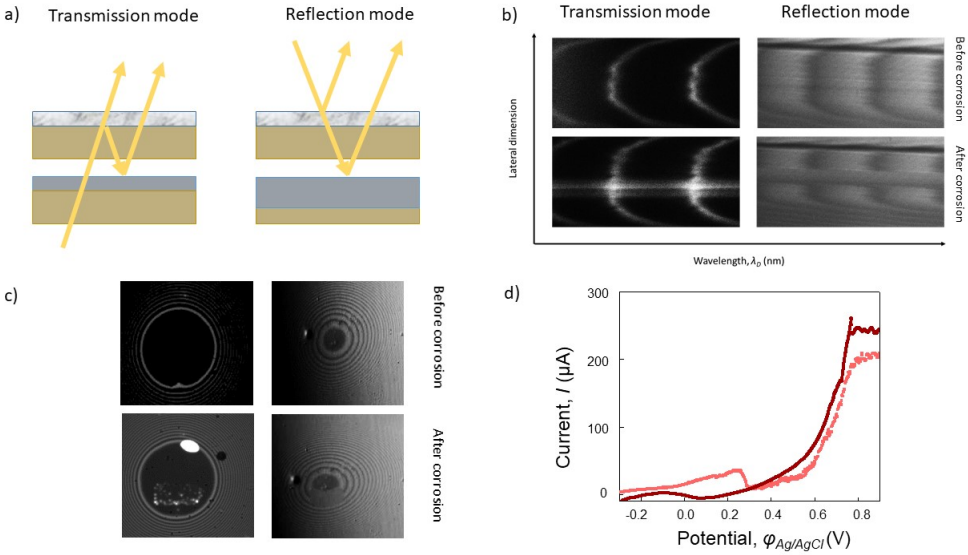

Figure 3.15: ***A comparison between the observation of the corrosion process in transmission and reflection mode.***

of a 50 nm surface dissolution and of 100 nm thick layer. We can observe how the current needed to dissolve the thicker layer is higher due to the higher surface area.

3.8 Analysis of reflection mode with multiple matrix method

For this work, we did not use the simplified equations shown above to analyze interference spectra. Instead we implemented (not part of this thesis) and used a multiple matrix based approach. A number of researchers, specifically K. Vanderlick et al. [48], who pioneered the approach in 1994, independently developed more rigorous analysis approaches [49, 50], compared to the analytic equations discussed before, and adapted the Multiple Matrix Method for SFA using a 2×2 matrix derived by Born and Wolf [51] to simulate interferometric spectra.

The Multiple Matrix Method is an approach to describe the amplitudes of incoming and outgoing light depending on polarisation on a per-media basis. It is designed to be a solution to Maxwell's equations and depends on the thickness and complex refractive index of a stack of optically homogeneous and parallel media. Using a 2×2 matrix approach limits the analysis, however, to systems with

linear eigenpolarisations. This means, the 2x2 matrix methods are not capable to describe anisotropic optical layers such as mica, which is used in this work as crevice former.

In the home made SFA explorer software (available via TU Wien) used for analysis in this work a 4×4 transfer matrix approach based on the method developed by Schubert [52] is implemented. It allows simulation of full transmission and reflection mode MBI patterns obtained in our corrosion SFA experiments. Anisotropic and isotropic interferometric layers are described by a partial transfer matrix within the model. The partial transfer matrices for anisotropic layers, such as mica, are calculated using a unique numerical fitting approach. The corrosion SFA data is then fitted to the generated model[46].

Chapter 4

Real-time view of crevice corrosion of a Nickel thin film in an SFA in transmission mode

In this chapter, I will show how MBI in a transmission mode SFA (tSFA) can be utilized to study the corrosion of confined metal. Here, Nickel is present as a 30-40 nm thin film, which was coated onto glass using a physical vapor deposition. This provides a first proof of principle how MBI can be useful to studying corrosion. Direct real-time visualizations of a crevice corrosion process, measurement of local currents as well as dependencies on solution concentration and oxygen levels will be demonstrated. Finally, limitation of the tFSA will be discussed.

The following chapter is based on the article "In situ nano- to microscopic imaging and growth mechanism of electrochemical dissolution (e.g., corrosion) of a confined metal surface". In agreement with the copyright guidelines of "Copyright (copyrightyear) National Academy of Sciences, U.S.A." this chapter contains parts of text and graphics of said article. Confirmation is added to appendix. The author's contribution includes execution, analysis of all experiments, design of research, discussion of all experimental results, and article writing.

4.1 Introduction

Reactivity in confinement is central to a wide range of applications and systems, such as geological and technological processes, for example, pressure solution [53, 54], chemical mechanical polishing (CMP) [55], electropolishing [56], and corrosion [57, 58], including biocorrosion, for example, implants and dental fillings [59, 60]. In some cases, increased dissolution rates are desired, such as CMP; however, in other systems, particularly involving pitting and crevice corrosion, increased reactivity leads to material degradation and damage. In each of these systems, the confinement (close apposition) of two asymmetric surfaces in an aqueous environment is a common factor where increased reactivity is observed. However, unlike systems exposed to bulk solutions, the difficulties introduced by reactivity and transport (e.g., diffusion) in confinement lead to complications in developing an understanding of reaction processes under these conditions. Furthermore, few techniques are able to directly measure and study reactivity in confinement in situ at relevant length scales, leaving even more uncertainty surrounding the initiation and early growth of dissolution or corrosion processes in confinement. As a result, the understanding of early-stage reactivity in confinement remains challenging and more detailed nanoscale characterization methods are required to develop a deeper understanding.

From an electrochemical viewpoint, crevice corrosion—the focus of this article—and pitting corrosion are related phenomena [61, 62], although there are significant geometrical differences between them. Pitting corrosion is driven by an aggressive ionic environment and oxygen depletion in the stagnant electrolyte of growing pits on a surface exposed to bulk solution [63–65]. Crevice corrosion is a related form of localized/confined corrosion that may occur within cracks and crevices where depletion and reduced transport of species such as oxygen may lead to the development of aggressive media and local corrosion potentials [66]. Within crevice corrosion, the initiation and growth of pits are observed and, throughout this paper, we will commonly refer to pits within the crevice (which is a separate phenomenon from pitting corrosion).

Crevice corrosion is of particular concern for stainless steels and nickel alloys in contact with chloride-containing solutions, commonly found in marine environments [57, 58]. Chloride anions can be found in a wide range of environments such as seawater, industrial raw water, and sludge. In particular, the potential gradient that develops in crevice corrosion drives cations out of the crevices and anions, such as chloride, into the crevices [65]. The diffusion of ions into or out of crevices depends on their mobility. Chloride has a very high mobility and it is often present in high concentration in crevices. As such, chloride anions tend

to accumulate inside the crevice while the more hydrated and larger cations (e.g., sodium), which typically are less mobile, remain mainly outside the crevice. In addition, the hydrolysis of the dissolving metal ions leads to a stark local variation of the pH [62, 63, 67]. The dissolution products of the material (metallic cations) are also driven out of the crevice, which leads to a local change of the pH.

Ex situ macroscopic studies of pitting corrosion, crevice corrosion, and uniform corrosion of nickel alloys in different aqueous media and conditions were reported by various authors [68–70]. However, real-time and in situ nanoscale investigations of localized corrosion (both pitting and crevice corrosion) remain a challenge. In particular, localized corrosion processes take place at very small length scales and highly localized initiation sites that may be buried or hidden within the confined geometry of two closely apposed surfaces. A direct, in situ view into the various crevice corrosion processes at progressing cracks is experimentally difficult. Recently, significant advances have been made using X-ray tomography [71]; however, resolution limits still inhibit characterization of the onset of corrosion. Typically, electrochemical pitting corrosion and crevice corrosion tests are carried out in a system-relevant environment and conditions, and the sample surfaces are examined ex situ using a variety of different materials characterization and imaging techniques. Initial pit formation on an extended surface can also be studied in situ by locally resolved probe techniques, such as spectroscopy or X-ray tomography, but it is not straightforward to detect pitting corrosion since the initiation sites are sparsely distributed and typically hidden inside a confined area where two surfaces are separated by nanometer-sized gaps or crevices which are difficult to resolve (temporally and spatially).

Previous observation using a modified electrochemical surface forces apparatus (EC-SFA) on nonmetallic surfaces (e.g., silica) of electrochemical reactions, dissolution, and in situ observation of, for example, pit formation, has been demonstrated as a valid method to study reactivity in confinement using multiple beam interferometry (MBI) [31, 72]. We further demonstrated angstrom-resolved real-time visualization of the initial corrosion behavior in a confined environment using white-light interferometry to study corrosion of confined aluminum surfaces [73]. Here, we extend our studies to crevice corrosion of nickel. In addition to our previous method, a camera was added to visualize and quantify the crevice corrosion process with simultaneous optical microscopy and interferometry (MBI) in real time. We studied the effects of concentration and charging dynamics on the corrosion initiation by changing the surface potential/charge ramping rate, and following the initial dissolution and pit formation of confined nickel surfaces in chloride solutions. Based on our experimental results and methodology, we present a detailed mechanism for the initiation and initial growth of pits during nickel crevice

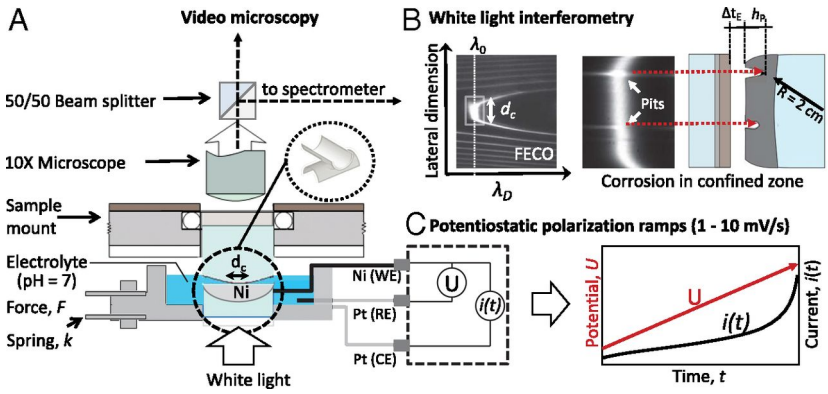

Figure 4.1: ***Surface Forces Apparatus:*** *crevice corrosion setup using the SFA. Simultaneous (A) optical video microscopy and (B) white-light interferometry allow tracking of both optical images of corroding confined areas and depths hp of corroding areas via shifts of the corroding metal mirrors via wavelength shifts ($\Delta\lambda = \Delta\lambda D$- $\lambda 0$) of FECO, and via intensity changes due to metal mirror thinning. For establishing a confined round-shaped area (A) back-silvered mica surfaces are used as compliant crevice formers. Typical contact areas have a diameter $d_C \sim$ 100–300 μm. Depending on the contact force F and the resulting flattening of the compliant mica surface, a controlled pressure can be applied, resulting in a uniform equilibrium electrolyte film thickness ΔtE in the confined zone. In addition, (C) a potentiostat with a three-electrode setup is used to apply external potential ramps to the nickel surface. Here, nickel was used as the WE, and Pt wires were used as the RE and CE. All data are referenced to OCP, which is −450 mV vs. Ag|AgCl.*

corrosion, which may provide general insights into nanoscale pit formation and growth in other systems.

4.2 Apparatus Modifications

The EC-SFA has been adapted for characterization of corrosion processes in confinement as shown in **fig. 4.1A**. In addition to a standard EC-SFA setup [31, 74], an optical camera connected to a 10 × microscope was added to simultaneously record both (i) optical images of the corroding confined areas and (ii) shifts of the corroding metal mirrors via wavelength shifts in the fringes of equal chromatic order (FECO) [75]. A typical FECO image showing a flattened contact is depicted in **fig. 4.1B**. The 2D FECO pattern or spectrum measured in the spectrometer simultaneously provides a spectroscopic axis to directly measure the distance between the two apposing mirrors with a resolution of 0.1 nm and a lateral axis for an optical image of a section through the contact region with a resolution of

about 0.7 μm. For more details on the use of FECO, we refer the reader to an article by Israelachvili [75]. A 50/50 beam splitter equally divides the light between the camera (i) and the spectrometer (ii). A round-shaped confined area was established by pressing a back-silvered mica surface, as a crevice former, onto a nickel-coated glass disk (30-nm Ni film, PVD deposited) as previously described [76]. In addition, (iii) a three-electrode setup with nickel as the working electrode (WE) and two Pt wires as the reference (RE) and counter electrodes (CE) are built into this setup.

4.3 Experimental Procedure

First, a dry contact (defined as $D = 0$) was established between the mica and the nickel surface (direct contact). Afterward, aqueous NaCl solution was injected between the two surfaces at concentrations ranging from 1 to 100 mM. FECO and real-time video were recorded simultaneously as the electrochemical potential was ramped up from open-circuit potential (OCP) = 0 mV (i.e., -450 mV vs. Ag|AgCl) at varying rates (**fig. 4.1C**. During a preramp period of 120 s after the electrolyte was injected, the ingress of electrolyte was traced and the OCP was recorded to confirm a proper working electrochemical cell. Any changes of the separation distance between the Ag and the Ni mirror surfaces due to, e.g., ingress of water, or a shift of the Ni-mirror surface due to corrosion (conversion into oxide or dissolution), can be tracked in situ by monitoring three signals: (i) the distance shift of the mirror (wavelength shift of a standing wave), (ii) the change of the light intensity (i.e., more light passing through the nickel mirror due to the thinning of the reflecting nickel layer), and (iii) the width of the FECO fringes, which provides information about the roughness of the reflecting Ni surfaces. As such, all signals and parameters together allow us to distinguish clearly the difference between roughening from oxidation or water ingress. Water ingress will shift the FECO fringes to longer wavelengths, while an oxidation shifts the FECO fringe wavelength and increases the intensity of the light going through the nickel mirror. Moreover, pure roughening leaves the FECO fringe wavelength position unchanged (because the average surface height does not change), yet the width of a FECO fringe increases proportionally with the rms roughness. As of now, the setup is restricted to corroding thin films studied in transmission mode; extensions to bulk samples may be possible using reflection mode interferometry [77] as shown in the next chapter.

4.4 Nickel Thickness Determination

For analyzing and determining Ni thicknesses, we can use both white-light interferometry and intensity analysis of the light passing through the interferometer. First, to translate FECO wavelength shifts recorded with the imaging spectrometer using white-light interferometry into distance changes, we use an in-house-developed software (SFA Explorer from TU Wien). The SFA Explorer uses the multiple-matrix method, as proposed by Schubert [78], to simulate and fit interferometric spectra against measured spectra. To fully visualize evolving crevice corrosion in 3D, the part of the surface that is projected into the spectrometer slit can be rastered back and forth to obtain FECO for the entire crevice area. Lateral scans of the crevices can be performed with a linear motor, moving at a given speed (here, 4.8 μm/s), while the frame rate was kept at 10 frames per second (fps) providing a nominal 500 nm resolution with 1-fps time resolution. With this setting, the spectroscopic dimension (wavelength and light-intensity changes of 2D slices) can be scanned with frame rates up to 30 Hz. However, the third lateral microscopic dimension can only be scanned at a considerably slower rate ($\sim$1 Hz)—taking about 100 s for the entire crevice scan. As such, the FECO can only be recorded fast enough to visualize initial corrosion at a static position. Hence, we also implemented a faster Ni-thickness determination method based on using the intensity changes in the optical image (top-view camera) taken at a given wavelength. For this, we calculated the intensity of typical standing waves as a function of the Ni thickness using the multiple-matrix method for the given interferometer setup. This reveals a linear relation of intensity and Ni thickness 4.2. Based on this result, a linearized attenuation model with an effective extinction coefficient can be used to directly extract the Ni thickness from optical images with $\sim$0.5 nm depth and $\sim$500 nm lateral resolution. Over the entire crevice area this analysis can be performed in real time with frame rates up to 0.1 kHz (depending on the top-view camera).

4.5 Results and Discussion

A typical corrosion experiment starts with the mica and nickel surfaces pressed together under dry condition to form a circular-shaped crevice with about $\sim$300 μm diameter. The electrolyte solution is added while the nickel electrode remains at OCP. **Fig. 4.3** shows how $\sim$2–3 nm electrolyte ingresses into the confined area (i.e., where the surfaces are in close contact). This can be directly inferred from a positive mirror shift, detected by a red shift of the FECO fringes, and was routinely

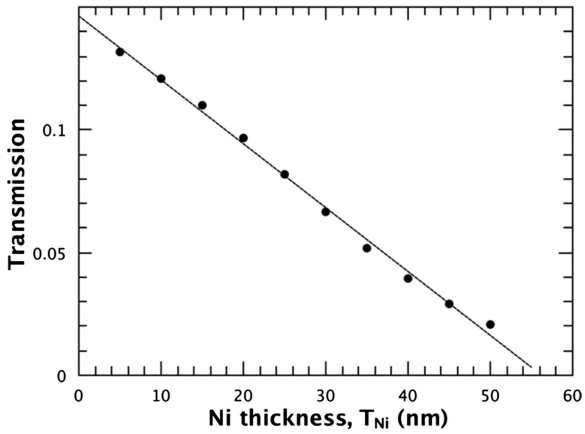

Figure 4.2: ***Ni thickness*** *Calculated light transmission through interferometer for wavelength of ∼575 nm using the multiple-matrix method as implemented in the SFA Explorer, indicating a linear relationship with R2 ∼ 0.99 for light intensity versus Ni thickness in the range relevant to the experiments discussed in the main text.*

recorded during the wetting of the crevice. One hundred and twenty seconds after wetting the crevice and establishing a stable OCP, a potential ramp with +1 mV/s was started from the OCP toward anodic potentials. There are a number of interesting details that we observe during the corrosion of the 30 nm-thick nickel surface in this configuration, which we show and discuss below.

With the EC-SFA, one can track and quantify in real time the crevice corrosion mechanism upon application of any (here, anodic) ramp. The real-time imaging (recorded with the top-view camera; see again **fig.4.1A** of crevice corrosion initiation shown in **fig. 4.4** indicates significant qualitative differences in the corrosion mechanism depending on the chloride concentration and the applied ramp rate. At high chloride concentration (>10 mM), shown in **fig. 4.4 a)** and **fig. 4.4b**, corrosion initiates at the crevice mouth while the inner part of the confined zone remains intact at 1 mV/s ramp rate; this qualitative effect reverses, with corrosion initiating inside the confined zone, at slower ramp rates of 0.5 mV/s shown in **fig. 4.4c** and **fig. 4.4d** . Furthermore, at low chloride concentrations (<10 mM), shown in **fig.4.4 e)** and **fig. 4.4f** , corrosion initiates inside the confined zone where the surfaces are separated by only a few molecular layers of solvent (∼2.5nm liquid film; see again **fig. 4.3**), irrespective of the ramp rate (from 0.5 to 10 mV/s).

The rate-dependent behavior of the crevice corrosion, as seen in **fig.4.4 b)** and **fig.4.4 d)** , shows the connection between active ion mobility due to the applied potential rate. At high potential rates (>1 mV/s), the chloride ions accumulate at the rim (contact boundary) enhancing the crevice corrosion rate while lower

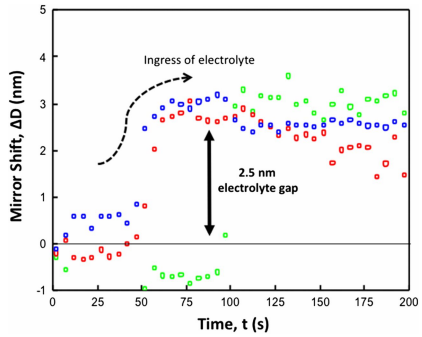

Figure 4.3: ***Injection of the electrolyte*** *Recorded mirror shift measured by FECO during injection of electrolyte. One can clearly see that an electrolyte layer of about ∼2.5 nm thickness penetrates into the gap. The different colors indicate different locations inside the gap. Green is in the center, red and blue at the crevice mouth*

potentials (<0.5 mV/s) allow ions to diffuse into the crevice before crevice corrosion is initiated.

As expected, this behavior supports a simultaneous potential gradient and ion migration kinetic-driven mechanism of crevice corrosion. In particular, crevice corrosion has been explained previously based on a combination of the ohmic drop (iR drop) into the crevice [79] and the location where an aggressive so-called critical crevice solution (CCS) with low pH [formed from the hydrolysis of Ni due to corrosion [76] and high chloride concentration (ion migration to maintain charge neutrality in the crevice) is created and maintained in relation to diffusion and migration of solution species [16]. We find that the location of crevice corrosion initiation moves toward the center of the crevice with an increasing iR drop at lower chloride concentrations. The observed crevice corrosion behavior in the experiments fits the framework of the iR drop theory because the potential inside the crevice will be lower than outside. This explains why crevice corrosion initiates and also maintains higher rates deeper into the crevice at lower solution concentrations. Conversely, at lower iR drops—i.e., at higher concentrations—crevice corrosion is initiated closer to the crevice mouth. With the lower iR drop, faster ion migration into the rim region (compared with migration into the center region) triggers the formation of a CCS at a region closer to the crevice mouth [16].

As anticipated from macroscopic observations, crevice corrosion depends on a delicate interplay of both the transport and depletion kinetics of active species which profoundly change the qualitative corrosion mechanism.

There are two electrochemical processes going on simultaneously here that need to be distinguished, which we now refer to as the "active" and "passive" processes.

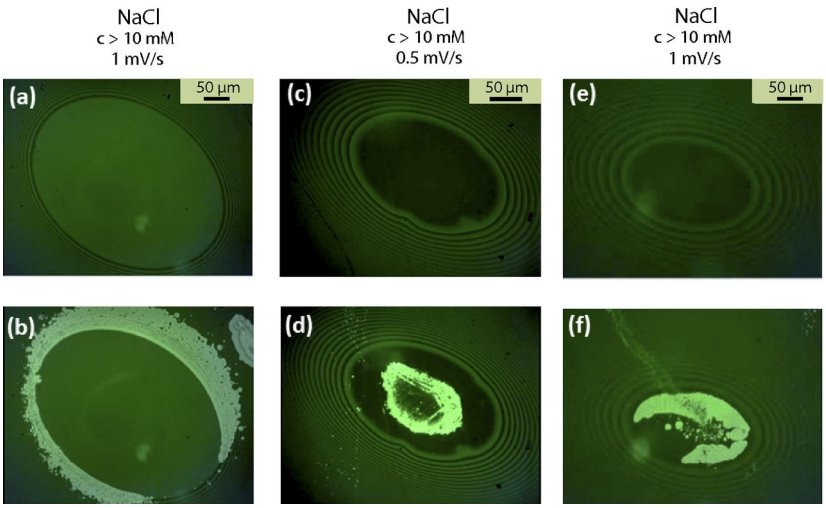

Figure 4.4: ***Optical images of the corrosion process in-situ*** *Optical microscopy of confined nickel areas while applying a linear potential ramp with $\Delta U = 1\ mV/s$. Crevice corrosion (CC) of nickel in NaCl just after injection (Top) and after severe corrosion occurred (Bottom): (A and B) At c >10 mM with a ramp rate of 1 mV/s indicating corrosion along the crevice rim; (C and D) at c >10 mM with a ramp rate of 0.5 mV/s, indicating corrosion inside the crevice; and (E and F) at c <10 mM, indicating CC again inside the confined zone. The contact (e.g., Newton rings) for each experiment appears visually different due to the different angles arising from different radii/curvatures of the metal surfaces. Interestingly, we do not observe any notable changes in the morphologies and rates of CC due to curvature effects, contact area, and aqueous separation distances (in the range 1–3 nm)*

The active process involves the applied potential, U, that generated the current flow and is quantified by the iR values and changes as corrosion progresses. However, at zero applied potential there also exists a passive or "resting" potential, U_0, as in a capacitor or battery, even in the absence of any current flow or electrochemical reactions. The value of U_0 is determined by the difference in the "double-layer" surface potentials of the two (dissimilar) surfaces—nickel and nonconducting mica in this case—as well as the aqueous distance between them and the Debye length [80]. This potential, too, will change as corrosion progresses and presumably also contribute to the rate of pit growth [80]. A simple calculation based on electric double-layer theory [81] shows that a 3∼nm-deep pit will cause a change in U_0 of 30–60 mV. We are not able to quantitatively establish which of these processes dominate the iR drop or the change in the different potentials associated with this corrosion process.

Our data not only provide a unique real-time view of this expected behavior during crevice corrosion initiation, but an in situ EC-SFA experiment enables the

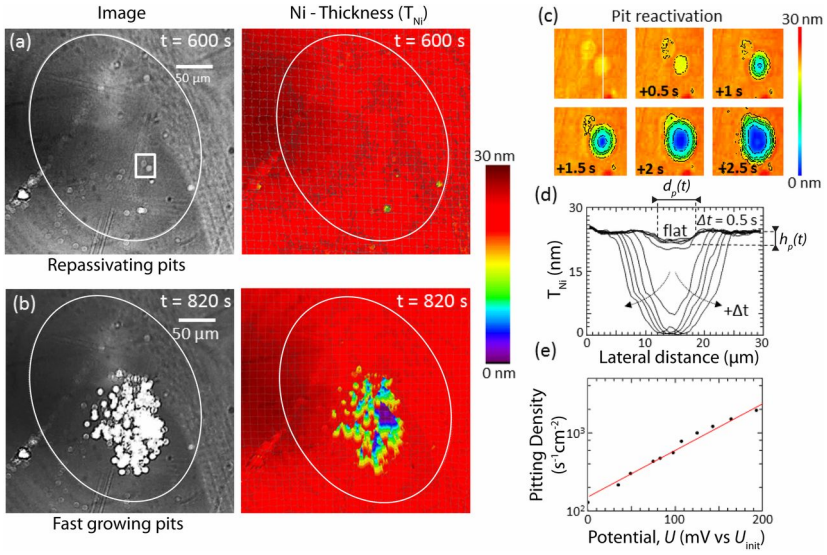

Figure 4.5: ***Reactivation of initially passivated pits above the critical corrosion potential:*** *(a) Optical image (Left) and corresponding Ni thickness contour plot (Right) showing initial repassivating pits inside and outside the confined zone (region marked) after 600∼s linear anodic polarization with 1 mV/s starting from OCP (-450 mV vs. Ag|AgCl). (b) Same confined zone after 820∼s polarization (i.e., 820 mV vs. OCP) showing fast active pitting inside the confined area. (c) Enlarged Ni-thickness contour plot of pit that reactivates (a) region marked by square, and (d) depth profile as function of time recorded at line indicated in C. Pit diameter $d_p(t)$ and pit depth hp(t) are indicated for the repassivated state. Corrosion will continue until consumption or repassivation of the nickel surface. (e) Pitting density of repassivating pits referenced to the initiation potential $U_{init} \sim 300$ mV (vs. OCP) where the first pit was detected in the field of view. Individual pit counting was terminated once a critical pit started fast corrosion.*

ability to track and quantify nanoscopic details of the initial growth mechanism. This includes qualitative and quantitative changes of corrosion dynamics into local currents with nanoscale-depth (single active site) accuracy and microscale lateral resolution.

Fig.4.5 shows two snapshots of (Left) a microscopic image, and (Right) a 3D analysis of the Ni thickness at progressing time and increasing potential (+1 mV/s). The displayed experiment was recorded at 1∼mM solution concentration of NaCl.

First, we observe that crevice corrosion of mica-confined nickel surfaces does not initiate as homogeneous, locally uniform corrosion. One can observe the formation of nanoscale-to-microscale pits that evolve with exceptionally rapid kinetics (in the microsecond range) before they become metastable, both inside and outside the

crevice, before the initiation of nickel crevice corrosion in confinement.

In particular, **fig. 4.5a** shows an optical image indicating pits with very similar diameters of $d_p(t) \sim 6$–7 μm. The first pit was detected about 300 s after anodic polarization was started (i.e., at 300 mV vs. OCP). The average pit depth of these initial pits is about $h_p = 2$–4 nm and the bottom is flat, as can also be seen in the depth profile shown in **fig. 4.5c** and **fig. 4.5d** . These pits appear inside and outside the confined zone within less than 500 μs (one recorded frame), indicating a localized and extremely rapid, yet self-inhibiting, corrosion process. These initial pits do not immediately penetrate the entire Ni layer as expected by typically estimated anodic pit-current densities [62]. These pits form within less than 500 μs (i.e., within one recorded frame); however, once a typical critical diameter $d_p(t) \sim 6$–7 μ is reached, the formed pits become inactive and the localized corrosion stops (i.e., arrests). We can directly calculate the local charge that transfers in a single site based on a volumetric analysis of nickel loss. From the estimated local Ni-thickness loss **fig. 4.5c** and **fig. 4.5d**, we can calculate a charge transfer of 0.97 μC per pit, which estimates a minimum pitting-current density of >5 A/cm^2 for these pits that appear within t <500 ms. These directly measured single pit-current densities compare well to estimates from penetration time measurements using thin metal films [82], where a range from 1 to 30 A/cm^2 was estimated. These previous studies found that the anodic pit-current density—derived from the penetration time—depends on the thickness of the metal film and the applied potential. Our data extend this view, and demonstrates that initial—non penetrating—pits show rather uniform diameters and depth, without any strong correlation with the applied potential. **Fig. 4.5e** shows that these initial, often referred to as noncritical, pits pop up with an exponentially increasing probability with the increasing potential. We argue that these noncritical pits may be central to establishing the local solution conditions that are necessary to catalyze the corrosion rate of a critical pit that will penetrate the thin film. Considering the corroded volume of nickel in such a pit, we estimate that the solution temporarily reaches very high concentrations.

In addition, the low aspect ratio of pit height to diameter $[h_p(t)/d_p(t) \sim 10^{-3}]$ of these noncritical pits suggests that the initial lateral corrosion is at least three orders of magnitude faster than the initial vertical corrosion into the material. The lateral resolution ($\sim$0.5 μm) constrains the direct observation of the nanoscale morphology (e.g., structural or chemical defects), preventing an accurate description of the pit initiation; however, other studies have observed direct evidence of such defects using in situ near-field microscopy techniques ([63, 83, 84]). Combination of the observed circular-shaped pits and the flat bottom (i.e., counter-bore shape) suggests that a very local oxide breakdown—possibly at defect sites—triggers the

initial pit formation with epitaxial corrosion dynamics. Corrosion triggering defects may significantly lower the activation energy for passive layer dissolution. Once a local defect or impurity in the metal or oxide triggers pit initiation, initially sharp and convex edges of an evolving pit generate a strong electric-field gradient that accelerates lateral corrosion, rapidly increasing the lateral diameter of the pit while the depth increases about three orders of magnitude more slowly (**fig. 4.6** for a detailed proposed mechanism). Due to the confinement of the apposing surface, the solution within the pit becomes saturated quickly with nickel solutes, which arrests the corrosion reaction.

As shown in **fig. 4.5** above a critical potential (here, at +400 mV vs. OCP), an arrested pit within the confined zone (at the rim or the center depending on the chloride concentration) breaks the initial pit size of $d_p(t) \sim 6$–7 μm and hp(t) $\sim$ 2–3 nm and rapidly evolves into a larger depth. Again, from the estimated local Ni-thicknesses loss we calculate a charge transfer of 2.75 μC for this critical pit, which estimates a pit current density of $\sim$25 A/cm^2, which is up to 5$\times$ faster compared with the growth rate of the repassivating pits. From **fig. 4.5** 3D the initial depth penetration rate of this critical pit can be estimated at about 25 nm/s or 90 μm/h.

Moreover , the critical pit triggers and catalyzes a rapid evolution of new pits as well as reactivates other arrested pits in its immediate surroundings. This collaborative pit growth is most likely due to a strong variation of solute concentrations inside the confined zone and the formation of a CCS with low pH and high chloride concentration.

The collaborative pit-growth behavior supports the hypothesis that crevice corrosion of nickel in chloride solutions initiates as self-catalyzed pitting corrosion due to chemical changes in the crevice solution within the confined areas. As expected, the ongoing metal dissolution inside the confined region leads to an excess of positive charge in the crevice solutions, and to a lowering of the pH due to metal ion hydrolysis. This excess of local charge is largely compensated by the relatively faster migration of chlorides into the confined zone, while metal ion diffusion out of the crevice is relatively slower due to greater ion mobility of chlorides[16]. Pits that are formed outside the confined crevice area are all swiftly arrested, even at higher potentials, which may be due to the lack of buildup of local aggressive electrolyte environments [16, 86].

Based on the corrosion rates found for single pits (together with their measured dimensions and growth kinetics, as demonstrated in **fig. 4.5**), and for the entire confined zone we can finally compare integral currents (inside and outside of confinement) to currents estimated from volumetric Ni-thickness loss for localized

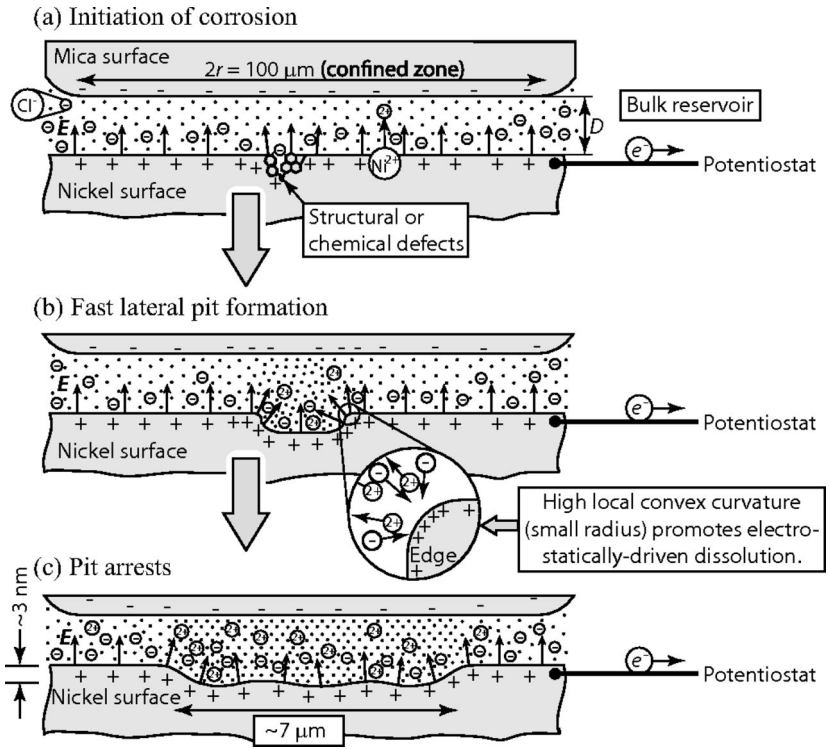

Figure 4.6: ***Proposed mechanism of nickel/nickel oxide dissolution/corrosion.*** *(a) Initiation of corrosion. The potentiodynamic ramp of the potential toward positive voltages increases the local potential and surface charging. Initially, the apposing mica and Ni surfaces are negatively charged, thereby constraining the diffusion of chloride ions into the cavity. As the potential of the nickel surface increases, the charge of the nickel surface increases to positive values; this results in the migration of chloride ions into the positively charged cavity to maintain charge neutrality. In addition, the closely apposed negatively charged mica surface further enhances the local electric field [80]. A structural surface defect (e.g., a dislocation, or an inclusion) locally accumulates surface charges and generates a Rayleigh-type instability [85] that lowers the interfacial tension of the solid–solution interface and favors dissolution. These defects can then act as corrosion trigger points, where the activation energy for nickel to escape from the surface is lowered. Once a defect dissolves the top layers of the material, very fast lateral growth starts with pits growing to a size of ~ 7 μm in diameter and a depth of only a few nanometers within less than 500 μs, before corrosion inside these pits arrests again. This indicates that the initial lateral corrosion is at least three orders of magnitude faster than initial corrosion into the material. (b) Fast lateral pit formation. These initial "noncritical" pits (i.e., pits that stop fast growth) form a very consistent and reproducible "counter-bore" shape with a sharp (i.e., highly curved) edge at the rim. The sharp convex edge generates a strong electric-field gradient that adds another, highly repulsive, electrostatic force between any ions and dipoles. This additional force enhances the nickel dissolution/corrosion at the sharp edge—rapidly increasing the lateral diameter of the pit while the depth increases much more slowly (several orders of magnitude slower). (c) Pit arrests. Finally, as the pit grows the edge becomes less sharply curved, leading to a weaker electric-field gradient. The bottoms of the pits were generally not completely flat or smooth, having a gently undulating shape, which is in line with the argument that local high curvature is a factor in governing evolution of growing pits. In addition, due to confinement of the apposing surface (dotted area), the solution within the pit becomes saturated with nickel solutes, which will arrest the corrosion reaction.*

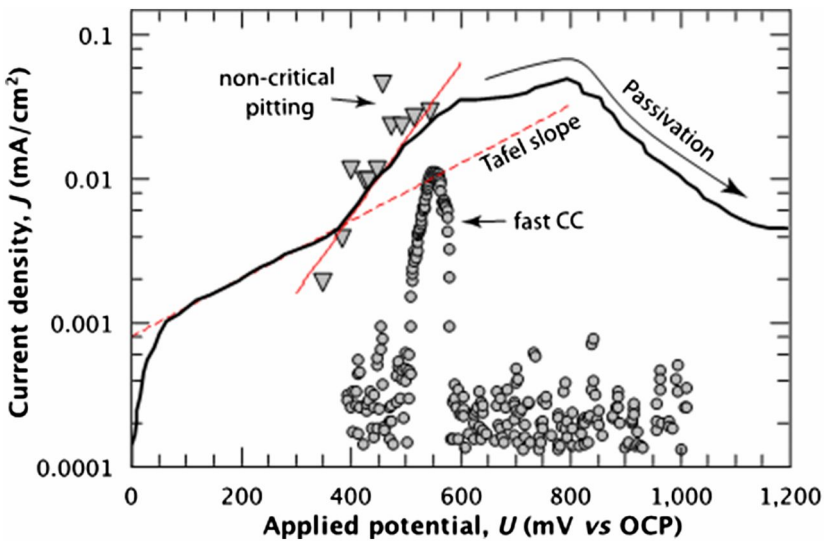

Figure 4.7: ***Electrochemically measured current density for experiment shown in fig. 4.5 (solid line)****. The current estimated from the pitting density of noncritical pits (triangles) as well as the current density originating from the fast CC within the confined zone are compared with the integral current (see the text for details). At higher anodic potential of ∼ 800 mV (∼ 450 mV vs. Ag|AgCl), polarization leads to the expected passivation of the outside region. The solid red line is a guide to the eye for the noncritical pitting curve that deviates from the Tafel slope, as indicated by the dashed red line.*

corrosion sites. **Fig. 4.7** shows excellent agreement, indicating that the deviation from the characteristic exponential Tafel slope (with $i_0 \sim 8 \times 10^7$ A/cm^2 is caused by the additional current density from defect breakdown into the observed noncritical pits. Also, the corrosion in confinement is fast and consumes the entire confined area within ∼100 s. Interestingly, the fast corrosion of the confined zone does not add significantly to the overall current due to the small area of our confined zone compared with the entire sample area. Locally in confinement, however, the crevice corrosion current density ranges up to 300 A/cm^2, which is a reasonable number given that about 10–20 critical pits with anodic pit-current densities of ∼25 A/cm^2 (see above) progress at the same time. As such, the EC-SFA provides a unique measure to in situ quantify the local current density in confinement, which is independent of any competitive reduction reactions such as local hydrogen evolution.

4.6 Conclusions

myboxIn summary, the EC-SFA provides a unique setup to directly visualize individual corrosion sites (here, pits) in confined spaces in real time and to analyze their initial growth kinetics. Compared with standard optical microscopy with transparent crevice formers, the depth resolution of evolving initial corrosive degradations is superior, allowing measurement of pit depths in 3D with subnanometer and millisecond time resolution. Also, the EC-SFA uniquely enables measurement of single pit-current densities and growth shapes in 3D (both laterally and in depth), as well as time-evolving pit densities within the confined zone.

Initial corrosion inside nickel crevices proceeds as preferential and self-catalyzed pitting corrosion (inhomogeneous localized dissolution with the formation of pits), presumably at surface defects within the confined zone. Our data also confirm that there is a strong interplay between migration kinetics of chlorides, bulk chloride concentrations, and the related iR drop (voltage drop), which leads to pronounced qualitative changes in the location (at the rim or center) at which pits form, and their subsequent kinetics. Importantly, local fast corrosion seems to play a crucial role in the initial development of a CCS within the crevice that drives the observed pit growth and propagation, suggesting that understanding and controlling surface chemistry and morphology are essential to prevent the onset of corrosion in the present system. Pit-current densities are >5 A/cm^2 for swiftly arresting noncritical pits, and $\sim$25 A/cm^2 for critical pits.

The above conclusions may be general observations for crevice corrosion systems; however, further studies with other corroding systems are needed to potentially extract and verify general rules and/or models as well as system dependencies of local corrosion rates in situ with nano- to microscale resolution. Local currents originating from reactions within the confined zone (with single pit resolution), and currents from outside the zone can be uniquely differentiated using the EC-SFA technique. In addition, the EC-SFA provides highly resolved data suitable for direct comparisons with quantitative theoretical models of the initiation of crevice corrosion for other metal and alloys systems, enabling direct characterization of initial crevice corrosion mechanisms.

4.7 Further investigations

The following is a further investigation of the thin film nickel and this results are unpublished and it goes beyond the original paper. Here, I would like, to bring the attention of the reader to some environmental and set up condition that could affect the corrosion behaviour of the samples. First I will compare the corrosion behaviour presence of argon and oxygen, so to simulate the crevice conditions. After it will follow a discussion about the influence of the potential on the pitting rate. I will show, how the surface structure could influence the shape of the pits, and finally some statistics about the position of the electrodes.

As mentioned before, even if the thermodynamic conditions for corrosion are fulfilled, although necessary they are not sufficient to guarantee the process of corrosion will happen. It is so required to analyze the process from a kinetic point of view, since it is the kinetics themselves that determine if the process of corrosion will take place or not. For this purpose, different conditions of the traditional corrosion experiments were tuned.

Influence of oxygen and argon

As mentioned in the introduction, one of the prerequisites for crevice corrosion to happen is the depletion of oxygen. On this line, some studies, showed that if the concentration of the oxygen between the crevice was increased, the incubation time would last longer [87]. **Fig. 4.8** shows the corrosion conditions and results on the 30 nm nickel film in Ar and Air atmosphere, in order to simulate the crevice conditions: a) and b) represent the NR before and after the corrosion process. We can notice that, while the presence of oxygen leads to the formation of pits within the crevice, on the other side, its absence makes the corrosion process more uniform than localized. So, if on one side the oxygen is helping to form an oxide layer to protect the metal, on the other side, at higher potential, it instead triggers the initial formation of pits. This finds its explanation in the IR drop theory. Due to the constricted geometric environment, which hinders the mass transportation in and out of the crevice, different acid or chloride concentration could lead to the destabilization of the restricted area.

In the presence of O_2 it is likely that oxygen reduction is catalyzed at the step edges of evolving pits. This may auto-catalyze the initial pit evolution, with catalyzed O_2 reduction at the rim of a pit and Ni-dissolution inside the pit. Furthermore, the hydroxide release will at some point favor passivation of the pit via $Ni(OH)_2$ precipitation, which agrees with our previous observations. Moreover, as expected,

the oxygen level plays an important role in establishing local corrosion inside the crevice and in the all opening zone between the two surfaces. In particular, in oxygen-poor environments corrosion occurs in large areas across the surface, with limited re-passivation inside and outside crevices. In oxygen-rich environments, depletion of oxygen limits re-passivation only in confinement where critical pits can evolve, while re-passivation outside of the confined zone reduces the possibility to form critical pits. Surprisingly, initial "non-critical" pits can only form in the presence of oxygen, suggesting an important role in the initial pit formation, irrespective of the location. In an oxygen-poor environment, an increased light intensity over the whole surface indicates non-localized corrosion (i.e., uniform dissolution), while in oxygen-rich environment the surface shows localized increased intensity inside and outside the confined zone (i.e., pitting).

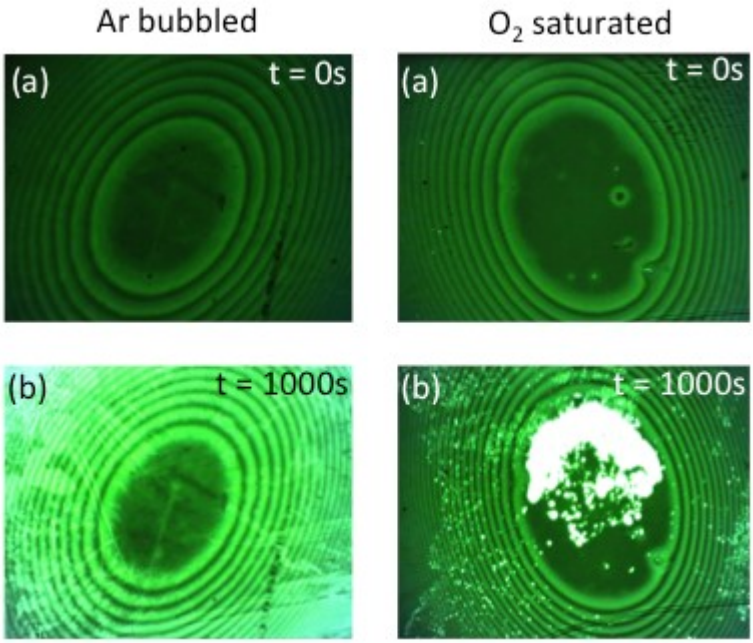

Figure 4.8: ***Simulated confinement environment.*** *Dependence of corrosion mechanism on the oxygen level in 1 mM NaCl at pH = 7.5, recorded from linear sweep voltammetry at 1 mV/s ramp rate. (Left) Ar-saturated electrolyte and vapor (a) before and (b) after corrosion occurred. (Right)* O_2*-saturated electrolyte in ambient air (a) before and (b) after corrosion occurred*

Influence of the dynamic ramping of potential

In contrast to the experimental condition previously discussed, here instead of increasing the potential linearly, we did long steps, in order to allow the system to adapt to every change of potential slowly and observe how it would react.

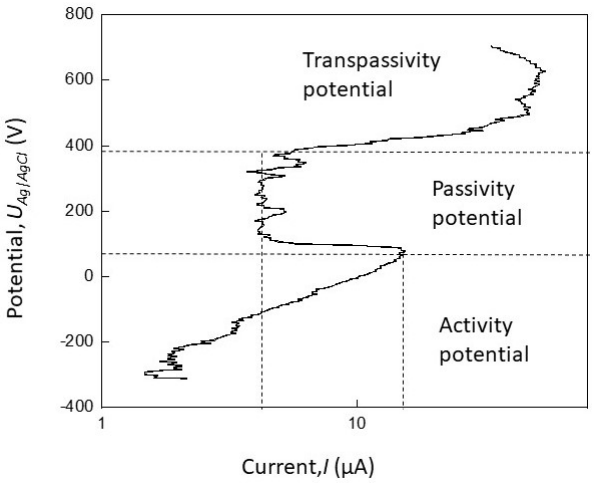

Figure 4.9: ***Nickel plot of the potential against the log of the current:****here we can see how the plotting of the current against the potential is showing, as expected, the typical transpassive behaviour for nickel.*

Fig. 4.9 shows the corrosion curve of 30 nm of nickel with steps of 10 mV with the potential held for 30 seconds. It shows the typical behaviour for a transpassive material as we can recognize three different steps: the active, the passive and the transpassive one. Between the active and passive transition, the current density can decrease by many orders of magnitude, due to the formation of an oxide layer. The transpassive region is when the oxide breaks down and allows high current to pass again.

From **fig. 4.10** we can see that the corrosion starts at the end of the passive region, at the transition with the transpassive one. Using the EC-SFA, we can follow the corrosion process in real time even enabling us to measure the potential at which each individual pit appears in the early stages as detailed in **table 4.1**. Here in **fig 4.10** only the most representative steps are shown: i) the contact before the corrosion ii) the first pit iii) advanced pitting and iv) self sustained corrosion (catalyzed). Moreover, we can even notice, that the pitting corrosion is here starting in the middle of the confinement, while the aggressive condition is then forming on the rim of the ring. At very high potentials we see a lowering of the current due to the reducing of the surface area because of the corrosion.

Pit number	Potential mV	Current μA
1	299	5.7
2	369	6
3	389	6.3
4	399	6.7
5	409	11
6	419	13.37
7	439	25.75
Fast pitting	449	31
Autocatalytic corrosion	669	43

Table 4.1: ***Potential and corresponding current for the pits appearing.***

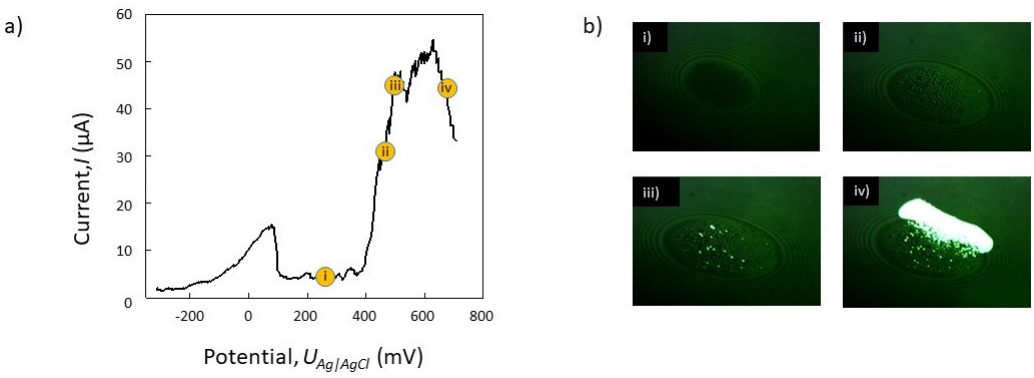

Figure 4.10: ***a) Step potential*** *recorded in 1 mM NaCl at pH = 7.5.* ***b)*** *Key points during the corrosion process: i) contact ii) formation of the first pit iii) sustained pitting formation iv) autocatalytic corrosion behaviour.*

The intensity data, due to the corroding layer, were then fitted with the multiple matrix method, as explained earlier, so that we are able here to calculate how much current did flow for every individual pit. From our analysis we can notice that the pits at the beginning, take around two seconds to form with an average current of 150-200 nA. **Fig. 4.11 a)** shows the charge plotted against time plotted for the time moment of **fig. 4.11 b)**. At higher potentials, when the current increases, the pitting becomes autocatalytc, and no matter whether the potential is held, the current still rises.

Here, we would like to address another key point. When the current is plotted against the potential, following the convention, it is normally plotted as current density; however, the geometric area of normalization is not changed. For these thin films there is a decrease of the plotted "current density" when the corrosion

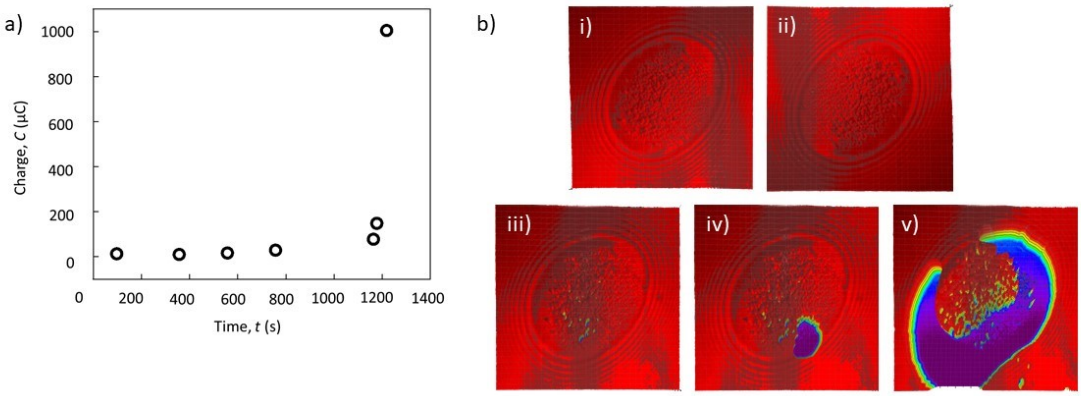

Figure 4.11: ***Calculated local charge:*** *a) charge consumed in every step b) simulated thinning of the layer and calculated depth for every single pit.*

is occurring, while, since the area is actually decreasing, an increase of the current density is expected. leading to a decreasing of the current when the corrosion is happening, while since the area is actually decreasing an increase of the current density is expected. This remark will find importance even in later chapters when we consider the corrosion on thicker surfaces. There, in comparison to the thin layer studies, the formation of pitting would lead to an increase of surface area, so it will show an increase of the current but a subsequent decrease of the corrected current density. By analyzing the video image to understand how much material was consumed, it is possible to recalculate the surface area for every frame and hence measure the effective current density for every step.

Influence of the position of the counter electrode

During different experiments, we also realized that the corrosion was progressing fast either at the center on on one of the sides of the contact area within the two surfaces. We provide statistical analysis of the probability of the starting point of the corrosion process to be in the middle or on the side in **fig. 4.12**; here, three groups are highlighted: corrosion starting at the center of the confinement (C), corrosion starting on the counter electrode side (R) or corrosion starting on the border from all the sides. It is possible to notice, how the highest probability of the corrosion start was either in the middle of the contact or on the side of the CE. This is easily explainable considering that the purpose of the counter electrode is to complete the electrical circuit between the working electrode (WE) and the reference electrode (RE). Current is recorded as electrons flow between the WE

and CE. Another factor to be taken into consideration is the distance between the surfaces and so to say, the thickness of the electrolyte. A further analysis showed us that when the corrosion was starting in the middle of the confinement, the thickness of the liquid was normally higher ($\sim$ 4-5 nm) compared with the corrosion process starting at one of the sides of the confinement ($\sim$ 1-2 nm). This difference in thickness could be explained according to the opening angle, and hence the geometry of the confinement leading to a saturation of the electrolyte.

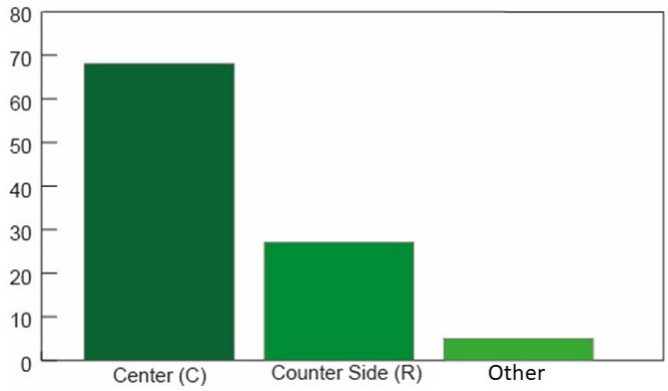

Figure 4.12: ***Probability chart of the staring position of the corrosion process:*** *the chart is based on a total of more than 50 experiments and more than 75% were analyzed to calculate gap between the two surfaces.*

Influence of the surface structure

In previous section of the chapter, we observed that most of the pitting forming due to corrosion had the same shape and the same size. We thought that the phenomena could have been attributed to the surface structure and, accordingly we performed some TEM measurements to characterize the microstructure 30 nm Ni thin films. The experiments discussed until now were all conducted on unannealed nickel surfaces (as deposited in PVD at room temperature). In **fig. 4.13** we can see the difference in surface structure of nickel before and after the annealing process.

The transmission electron microscope (TEM) image **fig.4.13 a)** was taken at the Jülich Institute of Energy and Climate Research using a Zeiss Libra 200 Cs combined with an objective-Cs-corrector achieving a resolution of < 90 pm. The images were then processed with a Digital Micrograph software. **Fig. 4.13** shows the different microstructure of thin film nickel before and after the annealing process. The samples were annealed at 600°C under vacuum for 3 hours. Before the

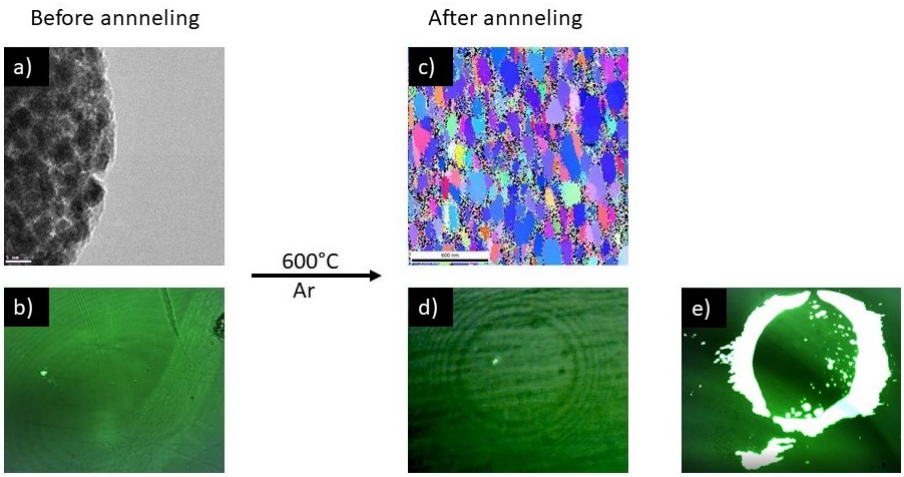

Figure 4.13: ***Relation between the structure and the corrosion mechanism of thin film nickel:*** *a-b) Represent the surface before annealing. a) TEM picture of the surface, it shows an amorphous structure with small cluster of nickel with a size of 20-30 nm; c-e) annealed surface, c) EBSD of the thin layer film after annealing. We can observe the formation of small grains and in d-e) how the corrosion pattern tend to spread more along grains.*

annealing we can see that the structure of the thin film is amorphous, with 10-20 nm spherical-shaped clusters of nickel; this spherical shape explains the shapes and the size of the pits. After the annealing, the clusters of material, aggregate forming small grains of $\sim 200\ \mu$m. Though the annealing does have an impact on the surface structure, the corrosion behaviour is quite similar. Pits are observed but larger defects tend to dissolve along individual grains and so on the corrosion behaviour. Another interesting influence of the formation of a structured layer is, that the corrosion potential, where fast CC occurs and pitting initiates, is shifted to higher anodic potentials. This is probably due to the lower amount of defects on the surface that could trigger the pitting, after surfaces were annealed.

Until now we have seen how multiple beam interferometry can be used as a technique to study crevice corrosion. After preliminary studies on the thin film nickel, we looked at how different conditions could affect the corrosion process. As last, we noticed a difference in the shape and size of pits due to the surface structure. We will go on studying the bulk material, which in general have a clear microstructure.

Chapter 5

Nickel and $Ni_{75}Cr_{16}Fe_9$: SFA in reflection mode

As a matter of fact I hope I convinced the reader by now how powerful MBI is for studying confined metals during active corrosion. However, one can immideatly ask whether it is possible to apply this technique to materials which have higher relevance than a 30 nm metal film. In this chapter, I will show how MBI in a reflection mode SFA (rSFA) can be extended to study the corrosion of confined metal. Here, nickel or the alloy is present as a 5 mm height block.Here a further understanding of the MBI in reflection mode is addressed. Different tecnique to analyze and imagine the post corrosion result will be explained.

The following chapter is based on the submitted article "Nanometer resolved real time visualization of acidification and material breakdown of Nickel and $Ni_{75}Cr_{16}Fe$ alloy in confinement" . This chapter contains parts of text and graphics of said article. The author's contribution includes execution and analysis of all experiments, design of research, discussion of all experimental results, and article writing.

5.1 Introduction

Due to their high corrosion resistance in various aggressive environments nickel and nickel alloys are widely used in different sectors of industry, including *e.g.* petrochemistry or power generation. However, in the presence of chloride, these materials display considerable susceptibility to corrosive degradation[57, 88]. Despite the enormous body of literature and work that was performed over recent

decades on corrosion of Ni-based alloys, crevice and pitting attacks, which take place in confined and localized spots respectively, are very difficult to detect and to study in real time[86, 89–94]. Further, it is currently not yet possible to quantitatively predict localized corrosion due to a limited mechanistic understanding of initial steps. In order to prevent or limit localized corrosive attacks, nickel can be alloyed with different elements to improve resistance[95] against localized corrosion.

Nickel as an alloying element reduces the corrosion rate by passivating the surface of the metal and increases the pitting potential. The breakdown of the passivity of the material is then related to the local dissolution of the passive chromium oxide film from the surface[96]. In this case, literature suggests that the chromium oxide film generally hinders the diffusion of oxygen from solution to the active metal surface, physically blocking the formation of active pits on the surface, while increasing the anodic dissolution potential to inhibit corrosive reactions[66, 97–103].

The initiation and growth of pitting corrosion should be observed in aerated halide solutions only in those metals whose critical potential is lower than the reversible oxygen electrode (E_{SHE} = 0.8 V). For example, metals like Cr and Ti that have their critical potential over 1 V are not expected to suffer from pitting corrosion[104].

However, there is a different situation in the case of crevice corrosion, where the media is stagnant and the concentration of aggressive species can accumulate. With proceeding corrosion reactions a simultaneous decrease in pH, increase in Chloride concentration and depletion of oxygen occurs. This results in a breakdown of the passivity and enhanced corrosion in a crevice, as well as generally lower critical corrosion potentials for most alloys. According to Fujimoto and Newman[105] a threshold concentration of around 10% chromium is required, so that a stable layer of Cr_2O_3 can form to protect an alloy from corrosion. Ebrahimi et al.[106] and Marcus et al.[107] showed through XPS measurements that the resistance of the passive film is controlled by Cr_2O_3 and that once the transpassive potential region is reached, the resistance of the film decreases with a parallel increment of $Cr(OH)_3$ content in the film. Once the passive film breaks down, and dissolution becomes stable, the role of the chromium is to effectively repassivate the crevice. Nagarajan et al.[108] also observed that superaustenitic stainless steels shows an increase of the roughness inside the crevice using optical and atomic force microscopy imaging [109].

While literature on crevice corrosion is vast and well advanced, [16, 110–112] development of methods to view crevice corrosion in real time and at initial stages

are notoriously difficult to develop. We recently[113] developed an interferometric technique for studying the initial crevice corrosion of vapor deposited or sputtered metal thin films (with thicknesses in the range of 20-60 nm) under the influence of confined geometries by using a modified transmission mode surface forces apparatus (tSFA). This setup provides valuable information to explore the initiation of pitting and crevice corrosion [114] of thin films. However, thin films often have a distinctly different microstructures compared to bulk alloys. The limitation of the tSFA is thus a drawback that greatly restricts the investigation of commercially available alloys, and effects of microstructure. In this work we resolved this shortfall, and designed a reflection mode equipped surface forces apparatus (rSFA) for operation with non-transparent bulk metal samples.

The idea of the rSFA was first tested by R. Horn [45] to study the interface between mica and a mercury droplet. Unlike the tSFA, the observed fringes of equal chromatic order (FECO) produce an intensity decrease of the interference pattern in rSFA due to the optical arrangement and light absorption within the interferometer cavity. Yet still, the information available about the confinement geometry can be calculated to the same precision as tSFA. The rSFA can however be used to study any sufficiently reflecting bulk material, including most commercial alloys.

Here, we discuss the newly designed rSFA, which is specifically tailored for generating crevices with well defined geometries. We test its performance using pure nickel and a $Ni_{75}Cr_{16}Fe_9$ model alloy and we complement this work by extensive pre- and post analysis of the samples used, utilizing optical microscopy, topography analysis using an atomic force microscope. We also characterize the samples using Electron Back Scattering Diffraction (EBSD) and nano-Laue diffraction. [115, 116], to characterize local crystal orientation [117], grain boundaries[118] and deformation around pits forming [119] at the corroding crevices.

5.2 Results and Discussion

Operating principle and construction of a Surface Forces Apparatus for reflection mode application

Fig.5.1 shows the major components of the newly designed rSFA, that was introduced already in chapter 3. The crevice former in **fig. 5.1a** consist of a molecularly smooth back-silvered mica (for details refer to methods and materials) glued to a glass cylinder with a radius $R = 1$ cm. The crevice former is compliant due to the

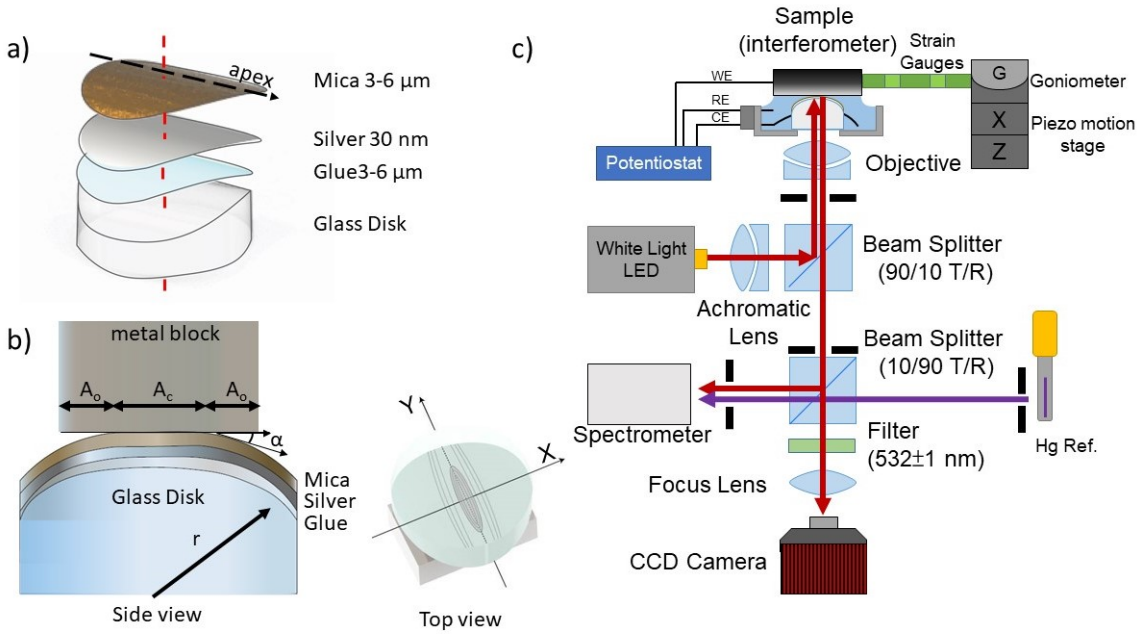

Figure 5.1: ***a)*** *Detailed view of the compliant crevice former.* ***b)*** *Detailed schematic of the sample arrangement (c.f. see text for details). A_c and A_o indicate the area of contact and the area outside of confinement where the apposing surfaces are separated by less then a few µm. Upon contact with the metal block, the glued mica layer can comply with the surface topology of the metal, forming a flat confined contact area with elliptic shape.* ***c)*** *Schematic view of a surface forces apparatus in reflection mode (rSFA). The white light path is represented by the red line, it is guided through a beam splitter where 10% of incident achromatic white light is reflected onto the interferometer (mica/sample). The objective simultaneously focuses onto and collects the light from the sample, at the second (10/90 T/R) beam splitter 10% is projected onto the CCD camera for Newton's rings observation. The other 90% is collected at the spectrometer, where the Fringes of Equal Chromatic Order (FECO) are observed. The sample acts as the working electrode, Pt wires are used as both counter and reference electrodes. A goniometer together with a set of XY-translation stages are used to fine tune the tilt angle and contact position of the sample.*

deformable glue. If the cylindrical shaped crevice former is pressed against a flat mirror polished metal surface (see **fig. 5.1b**) compliance and small variations of the metal grain heights result in flat elliptical contact zones (i.e nanometer confined areas) which are confining the highest grains that are in contact with the apex of the cylinder. Typical major and minor axis diameters of the confined area are in the range of 300 μm and 100 μm, respectively, resulting in confined areas of

$A_C = 0.3$ mm^2. The typical electrolyte thickness T_{fl} in the confined area can be directly measured using white light interferometry and is within the range of 0.5 to 3 nm, which also depends on the charging conditions within the crevice[114].

The elliptic shape of an established crevice also results in different crevice opening angles for the major and minor elliptical axis. The radius of the confining crevice former, can be varied from 5 mm $<R<$40 mm, allowing to control of the opening angle of the minor axis within a limited range between 5 and 15 . As can be seen from **fig. 5.1b**, we also indicate an area around the confined zone, where the crevice opening is typically increasing the distance between the apposing surfaces to some hundreds of nanometers, characterized by an area of A_O.

Fig. 5.1c shows the optical setup, the major motion degrees of freedom and the electrochemical cell. First, the sample, a Pt-CE and a Pt-RE are connected to a potentiostat, as described in the methods section. Second, a contact is established and aligned using a sample stage with coarse and piezo-based fine motion in xyz. A goniometer allows us to align the apex of the crevice forming cylinder in parallel with respect to the flat metal surface. The metal sample is additionally mounted to springs equipped with strain gauges for measuring lateral and normal forces to (1) assist with the alignment, and (2) to set a normal force and hence a pressure at the contact zone. Typical applied pressures in this work are around 2-3 *bar*. Third, interference microscopy and white light interferometry are realized using a home built reverse microscope setup, with an LED white light (WL) source. Collimated WL is guided into a 4x microscope objective using a beamsplitter with a 90 to 10 splitting, for transmission out of the path, and reflection into the confined zone and interference cavity, respectively. The light reflected from the interferometer cavity (ratio 10/90) is then guided through an additional beam splitter to simultaneously record both (1) a microscopic interference image on a CCD camera, and (2) fringes of equal chromatic order (FECO) in a spectrometer. The optical path is filtered through a green 532 nm laser line filter to specifically visualize the standing waves at 532 nm, i.e. to visualize so called Newton's rings (NR) generated by the interferometer cavity. Both, NR and FECO provide a measure for the dimensions of the confined area, with NR only providing a thickness resolution of about 2-5 nm[47], while FECO are accurate to within a few tens of *pm*. Finally, a Mercury reference lamp is guided into the spectrometer in parallel, in order to verify and calibrate the spectrometer.

Crevice corrosion of nickel and a $Ni_{75}Cr_{16}Fe_9$ alloy To test the performance of the newly designed rSFA we studied two different material types that are prone to crevice corrosion. Specifically, we use pure nickel and a $Ni_{75}Cr_{16}Fe_9$ model alloy. Addition of chromium results in the formation of a very stable Cr-rich passive layer,

and a lower susceptibility to corrosion is expected for the alloy. Standard anodic linear sweep voltametry (LSV) with a scan rate of 1 mV/s (**fig. 5.2**) confirm the expected behaviour with a shift of the critical potential of the $Ni_{75}Cr_{16}Fe_9$ to more anodic potentials by about 250 mV compared to pure Ni, indicating the increased corrosion resistance of the alloy.

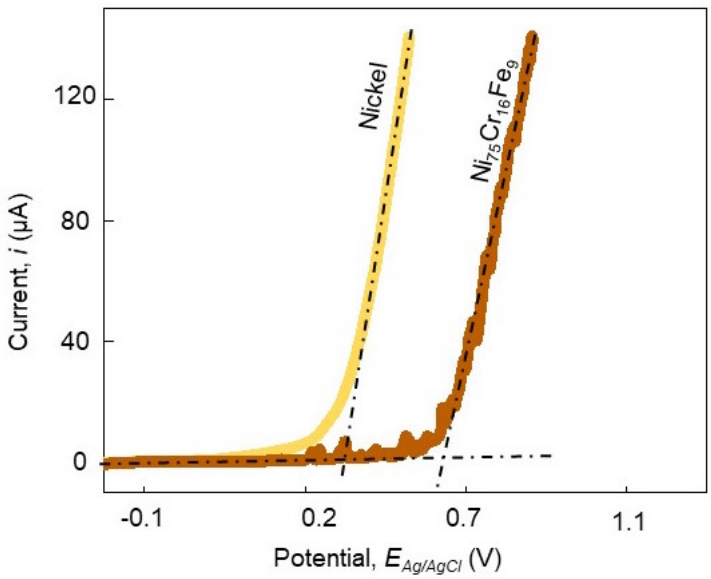

Figure 5.2: ***Linear sweep voltametry****. Linear polarization curves for nickel and $Ni_{75}Cr_{16}Fe_9$ in stagnant solution. Chromium addition to the alloy results in a significant shift of the breakdown potential to higher anodic potentials.*

Crevice formation and overview of the recorded crevice corrosion process in an rSFA.

In **fig.5.3** we first demonstrate the crevice formation for both materials in the newly designed rSFA. Specifically, **fig.5.3a** and **b** show how rSFA may be used to generate a confined area with precise control for nickel and the $Ni_{75}Cr_{16}Fe_9$, respectively. Generally, the local elliptical geometry of the crevice can be well-controlled in terms of the confined area, A_C, which is adjusted to a major axis diameter of about 300 μm for both examples.

The opening angle depends on the local curvature of the crevice former and indicate the expected larger opening angle along the minor axis of the ellipse. In general the opening angle is slightly variable within 0.5 due to gluing the crevice former onto a glass discs. Experimentally, opening angles along the minor axis

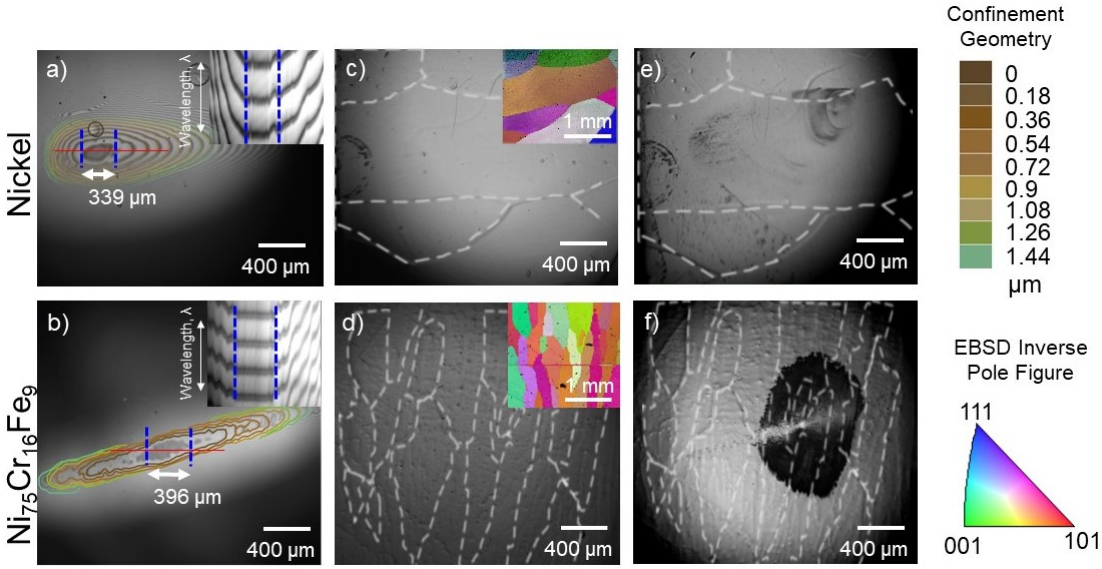

Figure 5.3: ***Establishing and characterization of confined zones****. Newton's rings of mirror polished surfaces of* ***(a)*** *nickel and* ***(b)*** *$Ni_{75}Cr_{16}Fe_9$ confined by a cylindrical mica surface. The Newton's Rings (NRs) were color-coded to indicate a height topology based on a NR analysis. Confinement geometries are further illustrated as inset figures of* ***(a,b)*** *showing typical FECO recorded for the samples.* ***(c,d)*** *Grain boundaries on these optical images are indicated with white dashed lines based on EBSD characterizations, shown as inset figures of* ***(c)*** *and* ***(d)****, for* ***(c)*** *nickel and* ***(d)*** *$Ni_{75}Cr_{16}Fe_9$.* ***(e,f)*** *Samples after corrosion, respectively.*

can be varied by varying the glass disc radius, which is an aspect that we did not study in detail in this work. The measured height-topology of the confinement geometry is indicated as a relief map in the figure as well. Irrespective of the lack in very precise control of the opening angle, the major advantage of interference microscopy is that it allows us to directly and precisely measure any established confinement topology. Opening angles and contact reliefs can be measured based on a nanometer precision,interference-based, distance measurement between the apposing surfaces at any point of the sample contact during the experiment. Even grain boundaries and differences in grain heights can be well resolved. This is clearly visible in the enlarged image of the established Ni-contact shown in the supporting information (**fig. 5.4**).

The small inset in **fig. 5.3a** and **2b** shows the wavelength resolved interference pattern (so called fringes of equal chromatic order) recorded across the contact as indicated. The constant wavelength of each standing wave in the center of the contact, marked by the dotted blue lines, indicates that the confined zone is flat

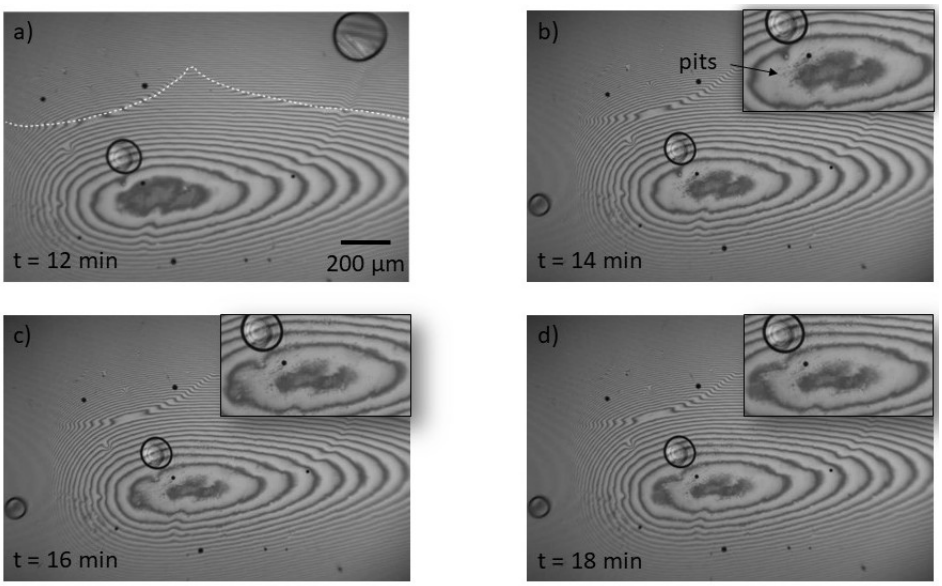

Figure 5.4: ***Time lapse of the corrosion of the pure nickel sample*** *We can see how initiation of pitting corrosion decreases the fully confined surface area inside the crevice. This is due to severe roughening of the surface. The round shaped features are gas bubbles trapped during the wetting of the confined zone. The insets in* ***b-d*** *show an enlarged image of the contact area. Pit formation is visible and indicated in the small inset in* ***(b)****.*

to within the roughness of the metal surface. Using the shift of this standing wave with respect to the dry contact allows us to directly calculate the thickness of the fluid film in confinement, which is estimated to be between 2.5 nm and 3.5 nm at OCP.

Prior to starting a corrosion experiment, all samples were routinely characterized by using electron-backscattering diffraction (EBSD) and optical microscopy. **Fig.5.3c** and **d** show an overview of the optical images together with the corresponding EBSD pattern and grain orientations recorded for the same area where the confined area is established. The Ni sample appears to have considerably larger grains compared to the alloy. We can now correlate grain sizes and orientation to the confined area corroded in experiment.

Fig.5.3e and **f** show ex-situ optical images of Ni and $Ni_{75}Cr_{16}Fe_9$ samples, respectively, after corrosion occurred at the confined areas. Interestingly, the corrosion mechanism of both materials proceeds completely different. Generally, Ni-samples show pitting inside the confined area A_C and in an area A_O around the confined area within the crevice opening. In contrast, the $Ni_{75}Cr_{16}Fe_9$ shows considerably less pitting inside of the nanometer confined area A_C, but a very pronounced cor-

rosion in the area A_O of the crevice opening. The black region in the optical microscopy is presumably due to severe corrosion and increased surface roughness in this region.

Detailed real-time view of the corrosion process using rSFA interference pattern. Apart form establishing very well-characterized confined areas and post-experimental inspection of the corroded area shown in **fig.5.3**, the rSFA allows us to analyze the corrosion process in real time. Therefore a time-resolved sequence of interferometric images is recorded during linear sweep polarization. Images can be recorded with real-time frame rates up to 100 Hz with our equipment. Here, we typically record with frame rates of 2 Hz, as the recorded processes are comparably slow. Representative images of the entire corrosion process are shown in **Figure 5.4** for nickel and in **fig.5.5** for the alloy.

The onset of corrosion on nickel and the $Ni_{75}Cr_{16}Fe_9$ appears at around 0.35 V and 0.6 V vs. Ag|AgCl, respectively. At the onset potential the initiation of crevice corrosion in the NR pattern was very obvious for the $Ni_{75}Cr_{16}Fe_9$, but it was less pronounced in the Ni sample (see SI for details), where we find increased pit formation at the confined zone, and less dense pitting outside. Interestingly, the $Ni_{75}Cr_{16}Fe_9$ displays a much more severe local corrosion mechanism. **Fig. 5.5(a-c)** show time-resolved NR pattern recorded during the LSV scan for the alloy, and **fig. 5.5d** shows the final corrosion damage recorded after the experiments.

Specifically, the NRs in **fig. 5.5(a-c)** show a very pronounced change of the standing waves, which is indicative of progressing local corrosive damage. In addition, a very decrease of the light intensity can be visualized at the center. The NR change and intensity changes in the confined zone can be viewed as a finger print of the changing confinement geometry and ongoing corrosive degradation, respectively.

Table 5.1: Spatially resolved corrosion rates for the $Ni_{75}Cr_{16}Fe_9$ along the major and minor axis of the confined zones.

Average speed μm				
time (min)	**X direction**	**Y direction**	**-X direction**	**-Y direction**
0-3	37.6 ± 4.2	53.4 ± 9.6	17.4 ± 2.6	48.7 ± 2.1
3-10	51.1 ± 3.6	34.3 ± 1.1	31.6 ± 2.9	45.9 ±2.3

Detailed analysis of the corrosion behavior of the $Ni_{75}Cr_{16}Fe_9$ shown in **fig.5.5a-c** reveals several noteworthy characteristics, which are *initiation from a single site in the confined area*, *directional and grain dependency* along with a weakly pronounced *potential dependency*.

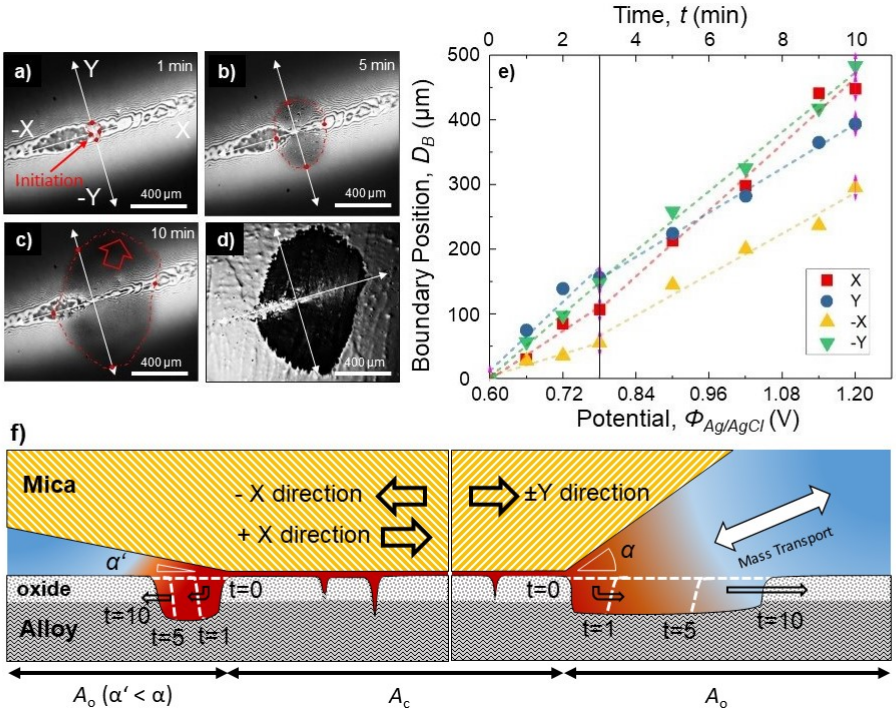

Figure 5.5: Real time corrosion analysis. ***(a-d)*** *Screen-shots of the video of the corrosion progress at different times (+1, +5, +10 min and after corrosion).* ***(e)*** *Crevice corrosion rate along the major elliptical axis (µm X) and (µm Y) for $Ni_{75}Cr_{16}Fe_9$ plotted against the time/applied potential.* ***(f)*** *Schematic of corrosion mechanism around the area of confinement for both samples. The local pH increase is indicated.*

First, in this example and in general the corrosion of the confined $Ni_{75}Cr_{16}Fe_9$ initiated at a single specific location (in the displayed example on the right-hand side) within the confined areaA_c. From this location corrosion progressively propagated out in all spatial directions. This behavior is consistent with the diffusive propagation of an aggressive crevice environment, starting from a particular initiation site. This is consistent with the strongly acidifying breakdown of the protective Cr_2O_3 into soluble chromate, which releases 10 protons per formula unit as follows:

$$Cr_2O_3(s) + 5H_2O(l) \rightarrow 2CrO_4^{2-}(aq) + 6e^- + 10H^+(aq) \tag{5.1}$$

Fig. 5.6 shows the real time resolution of the propagation of the roughening area, with the corresponding bend of the Newton's rings. More detailed of the phenomenon can be seen in the figure caption.

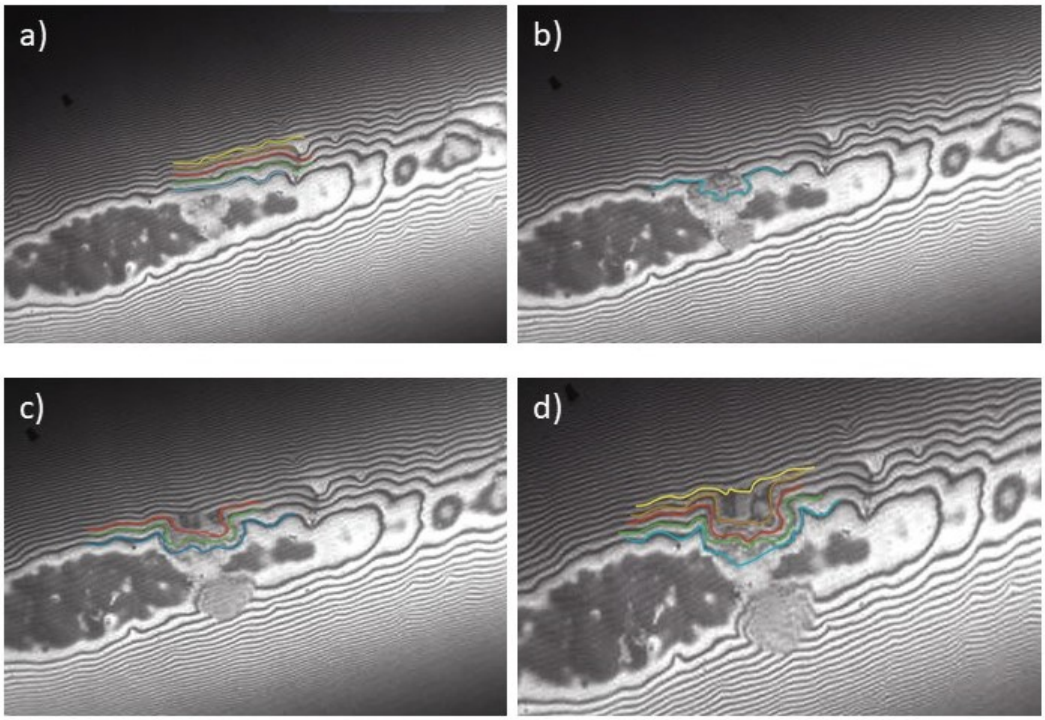

Figure 5.6: ***Bending of the Newton bands due to the dissolution of the oxide:*** *a) before corrosion and b-d) shortly after initiation. We calculate every constructive (or deconstructive) band is ∼250 nm away from each other, so a bending to down to another ring, would explain a dissolution of 250-300 nm. It is important to consider, anyway, that this value could be altered, if we consider the change of refractive index in the solution due to the dissolution of the alloy and accumulation of the chlorides.*

At the final stage as shown in **fig.5.5c** and **fig.5.5d** after mica has been removed, a very pronounced dark corroded region on Ni-alloy was observed. This dark region coincides with the lower intensity that propagated in the realtime NR images and is marked with red dashed lines in the interferometric images in **fig.5.5(a-c)**.

In contrast, on pure Ni (see again **fig. 5.3e**) pitted areas were observed inside, and in the close vicinity of, the confined zone, and general roughening and to a lesser degree pitting was observed over the entire surface. Considering that the anodic dissolution of nickel only generates 2 protons per unit formula, the less significant corrosive attack of nickel in the confined zone can be explained by the less acidic local environment as well. In addition the observed roughening is in good agreement with weaker protective properties of the passive film on nickel, which slowly dissolves at the applied potentials according to the nickel Pourbaix diagram.

We additionally performed XPS analysis of the surface chemistry of the corroded region and outside of the confined regions, for both materials. Data is shown in (**fig. 5.7/5.8**). For the alloy the data indicates that the oxide composition inside and outside of the crevice shows a very clear trend of $Ni(OH)_2$ depletion and Cr_2O_3 as well as Fe_2O_3 enrichment. This further confirms the expectation, that a passive Cr_2O_3 layer is enriched at the surface, and that its breakdown results in a strong acidification of the crevice environment according to **Equation 5.1**. XPS of the nickel surface revealed the expected formation of a $NiO/Ni(OH)_2$ layer, which may slowly dissolve in a mildly acidic environment of a crevice on nickel.

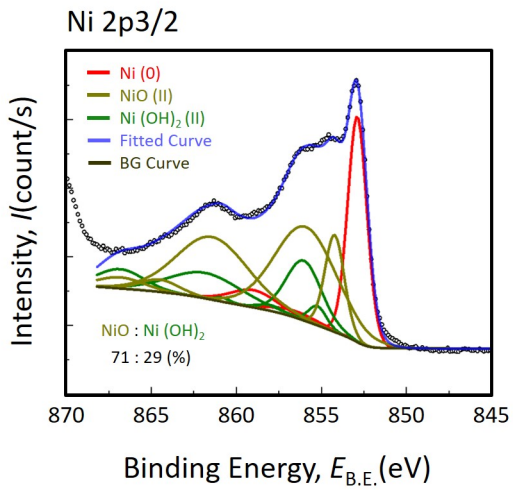

Figure 5.7: ***Representative nickel 2p$_{3/2}$ signal of the pure nickel surface.*** *Fitted components are indicated. Metallic nickel, Ni(0), nickeloxide, NiO, and nickelhydroxide, $Ni(OH)_2$ are sufficient to explain the measured spectrum. The chemical composition of the passive oxide layers in the confined and in the corroded region was analyzed using X-ray photo-electron spectroscopy (XPS). Nickel spectra recorded at 90indicate the expected formation of a mixed nickelhydroxide/oxide layer.*

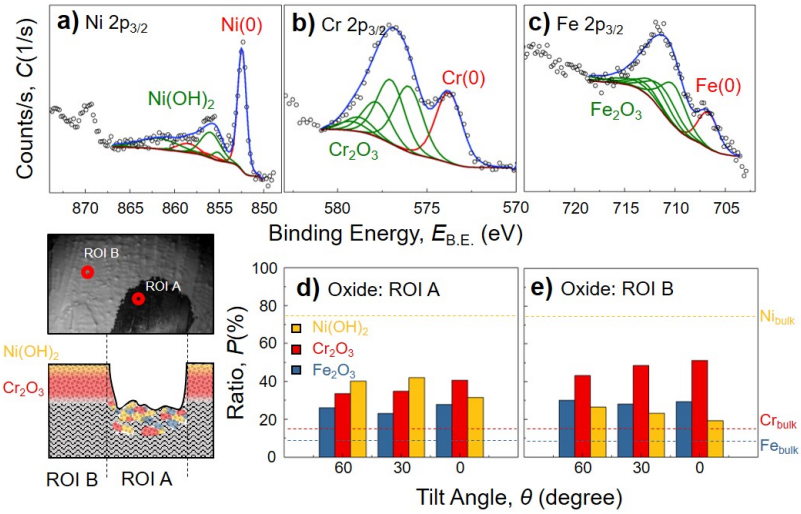

Figure 5.8: ***XPS analysis of $Ni_{75}Cr_{16}Fe_9$: a-c)*** *XPS fine-resolution elemental spectra for Ni, Cr and Fe elemental scans , respectively. XPS spectra of the $Ni_{75}Cr_{16}Fe_9$ alloy are shown in* ***fig. 5.8****. XPS spectra were recorded in the corroded area in the crevice opening, and outside the confinement as indicated in the inset, showing some interesting details as follows. The regions inside and outside the crevice corroded area were scanned to compare the difference of oxide composition. The local composition analysis in regions A/B is given in* ***d,e*** *as function of the photo electron take-off angle.* ***Fig. 5.8*** *shows elemental fine scans and fitting of the three major elements in the alloy, namely* ***a)****Ni,* ***b)****Cr and* ***c)****Fe), recorded in the non-confined area (ROI B). Data (not shown) was also recorded inside the confined area, giving similar components. As shown in* ***fig. 5.8(a-c)****, the XPS data (black circle) can generally be fitted very well with one metallic signal (red line) and a set of envelopes for the oxidizes component. Regarding the fitting of the oxidized components it is worth to mention that spin-spin coupling envelopes (SSCE) are utilized for fitting the transition metal oxides/hydroxides [**?**]. Specifically, for the oxidized components a particular set of SSCE (green lines) is used for fitting with a set ratio of areas. This allows us to obtain a good fit quality without invoking numerous components, and we can clearly identify the oxide chemical composition on $Ni_{75}Cr_{16}Fe_9$. Specifically, for both regions we find that the oxide consists of nickel hydroxide ($Ni(OH)_2$), chromium oxide (Cr_2O_3) and iron oxide (Fe_2O_3]).* ***Fig. 5.8(d,e)*** *compare the oxide composition inside (ROI A) and outside (ROI B) the crevice corrosion region at different tilt angles in terms of a ratio, respectively. For ROI A (rough area) the data taken at lower take-off angles has to be taken with a grain of salt, due to the sample roughness. Still, comparing with the elemental bulk ratio and with data from ROI B (outside), the oxide composition in ROI A (inside corroded crevice) shows a very clear trend of $Ni(OH)_2$ depletion and Cr_2O_3/Fe_2O_3 enrichment at all angles. In addition, in both ROIs an increasing of the sample stage tilt angle results in an increasing the $Ni(OH)_2$ contribution, and a decrease of the Cr_2O_3 contribution, while the Fe_2O_3 remained constant. This trend suggests an oxide structure, illustrated in* ***fig. 5.8d****, with the protective oxide layer consisting of Cr_2O_3 and Fe_2O_3, which is covered by a nickelhydroxide layer.*

Second, the shape of the corroded region at the final stage displays a weakly pronounced anisotropy, which cannot be explained by an isotropic diffusive spreading of aggressive electrolyte. This may rather be due to both the crevice opening geometry and the grain orientation. As indicated in **fig. 5.5(a-d)** this anisotropic progression can be decoupled into individual progression rates along the four principal directions of the elliptical contact area. **Fig. 5.5e** shows the tracking of the boundary position of the corroded region along these directions as a function of the applied potential/time. From the slope of this plot lateral corrosion progression rates can be calculated (see **table 1**).

Interestingly, corrosion initially proceeds slower along the ± X axis compared to the ± Y direction. In particular, along the -X direction (confined region) the rate is two times slower compared to the Y directions.

As sketched in the schematic in **fig. 5.5f** this is very likely due to the limited diffusion rate of the aggressive electrolyte along the confined -X direction, due to the different crevice opening angle and due to confinement and the potential saturation of the only 2-3 nm thick confined electrolyte in the -X direction. At a potential above 0.78 V the -X direction proceeds faster as well. This may be due to spreading of the aggressive environment at larger crevice opening distances, where diffusion into the -X direction is not limited by confinement any longer.

In the later stages it appears that both Y and X directions (via speed up of the X direction) show a weak directional tendency (see **fig.5.5 c**, red arrow), that alignes with the grain orientation as well. The preferential propagation direction is in line with the overall orientation of the grains in this region, which are orientated in a (X,Y) to (-X,-Y) direction. Interestingly this suggests that grain orientation dependency only plays a minor role during the initial spreading of CC, and only evolves at a later stage as a minor influence.

In comparison, it is interesting to summarize that the rSFA data indicates that (1) Ni-corrosion proceeds as pronounced localized pitting and roughening with statistically more pitting inside the confined zone, while (2) the $Ni_{75}Cr_{16}Fe_9$ shows an apparently more severe areal attack in the opening of the confined zone. In both cases, the attack proceeds from an initial critical breakdown at a specific site. This results in confinement acidification and faster breakdown of material in the immideate surroundings of the initial breakdown site. For the alloy we can follow the diffusion of the aggressive environment in real time. This is similar to the behavior found for Ni-thin films in our earlier work[114].

Post experimental analysis of the corroded areas. While interference images along with FECO pattern in the rSFA provide a real time view into a confined

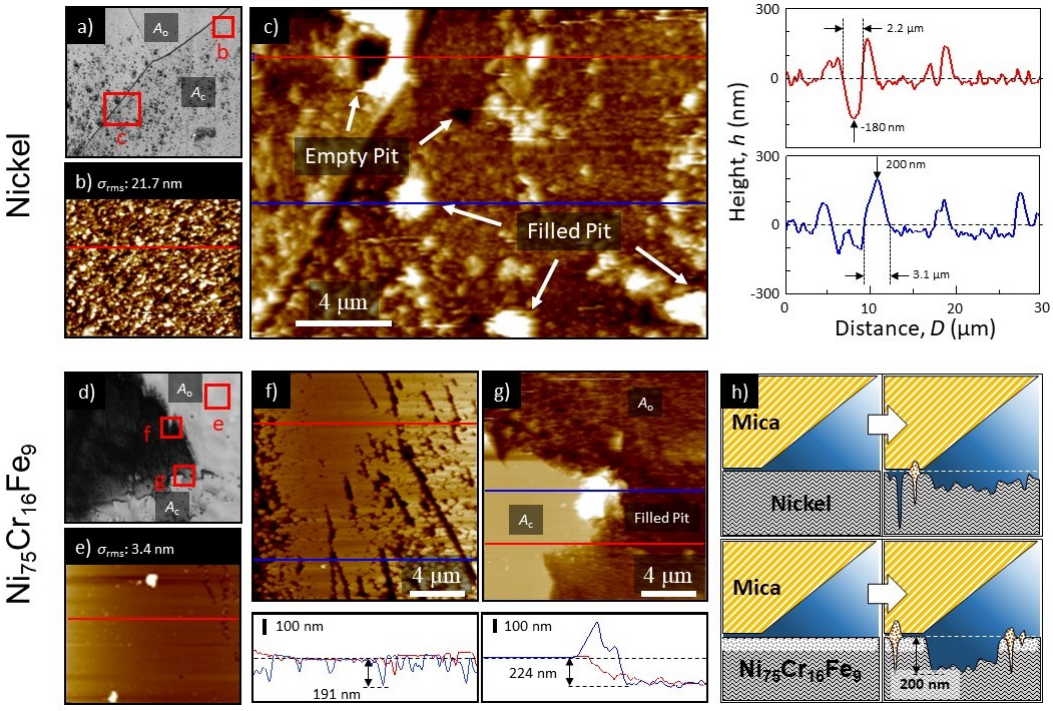

Figure 5.9: ***Post-experiment analysis of the corrosion area with AFM.*** *In* ***(a)*** *Optical image of the confined area of the nickel. AFM images of the surface of the nickel after the corrosion experiment* ***(b)*** *outside the confinement, and* ***(c)*** *inside the crevice area. In* ***(c)*** *two lines, indicate cross-sections shown on the right of the image. The red line indicates the cross-section over an pit, while the blue line is a cross-section of a pit presumably filled with precipitates.* ***(d)*** *Optical image of the* $Ni_{75}Cr_{16}Fe_9$ *after corrosion.* ***(e)*** *AFM topography inside the confinement that was not attacked by the corrosion. The surface is still as smooth as after polishing.* ***f)*** *is on the edge of the black region, the two lines indicate the cross-sections and the graph is reported below.* ***(g)*** *shows an AFM scan over a precipitate filled pit inside the confined region.* ***(h)*** *Schematic representation of the corrosion process for Ni and* $Ni_{75}Cr_{16}Fe_9$ *around the crevice former.*

zone, they are also limited to the Abbe limit of optical microscopy at about 200 nm local resolution. Hence, nano-scaled structure changes during the corrosion process remain unresolved in-situ. For instance roughening is only visible as an average broadening of FECO pattern. In this section, we hence complement the rSFA data with AFM imaging to provide high spatial resolution of both materials after corrosion, and we recorded nanoscale Laue diffraction of corroded regions after corrosion to provide further nanoscopic understanding of the processes visualized in rSFA.

High resolution AFM imaging. **Fig. 5.9** shows AFM images recorded at different areas of the corroded region for both materials used. **Fig. 5.9a** and **d** show an optical image of the corroded regions for the Ni and the Ni-alloy, respectively. The labeled areas indicate where the AFM topographies in displayed in panels **b-c** and **e-g** were recorded, respectively. The recorded AFM images reveal a number of interesting details and highlight the different mechanism observed for the Ni and the Ni-alloy, as follows (see also schematic interpretation in **fig. 5.9h**):

First, the region outside of the confined area of the corroded Ni shown in **fig. 5.9b** indicates a severe roughening with a roughness of $\sigma_{rms} \approx 22$ nm, compared to the initial 2-3 nm before corrosion (not shown). This indicates a rather uniform dissolution process across the entire surface of pure nickel, in addition to the increased pitting probability in confinement. The same roughness level is also found within the confined area shown in **fig. 5.9c**, where denser pit formation is observed as well. The respective height profiles for **fig. 5.9c** indicate that corrosion pits are at least 180-200 nm deep. This depth should be viewed as lower bound due to possible geometric restrictions by the AFM tip geometry. Interestingly, apart from roughening and pit formation also large protrusions up to 180-200 nm appear around pits, or presumably on top of a pit. This may indicate corrosion products that are precipitating in the confined area during the corrosion process due to saturation of the electrolyte, ending up in pits filled with precipitated oxide/hydroxide.

Second and in stark contrast the AFM topography in **fig. 5.9e** indicates that $Ni_{75}Cr_{16}Fe_9$ shows no significant roughening, neither outside the corroding area of the crevice opening, nor in the fully confined zone. However, within the crevice opening, where the surfaces are only a few 100 nm apart, the corrosion is more severe compared to the pure nickel. Specifically, at the progression front, shown in **fig. 5.9f**, severe and dense pitting with pitting depths of about 200 nm occurs. As indicates in **fig. 5.9g** and the respective height profile this dense pitting finally merges into a rough and approximately 200 nm deep corroded area that extends into all spatial directions initiating from the fully confined zone.

This is consistent with the region that was observed to spread in the rSFA data. Interestingly, **fig. 5.9g** and also **d** shows that the fully confined area A_C does not show any roughening, and only pitting with a smaller density compared to the pure Ni. It is visible in **fig. 5.9g** as well, that we again find - presumably precipitate filled pits - in this region with a very similar height compared to the Ni case. This is a generally interesting results and suggests, that the confined zone, where the electrolyte is only 2-3 nm thick, is better protected, presumably due to fast saturation of the nanometer thin electrolyte and reprecipitation. However, the severe reaction within the crevice opening again suggests that the chromium

contributes to a significant acidification of the environment according to **Equation 5.1**. This, in turn, leads to a faster corrosion in this area, where exchange with the bulk electrolyte is slow, yet fast enough to limit saturation.

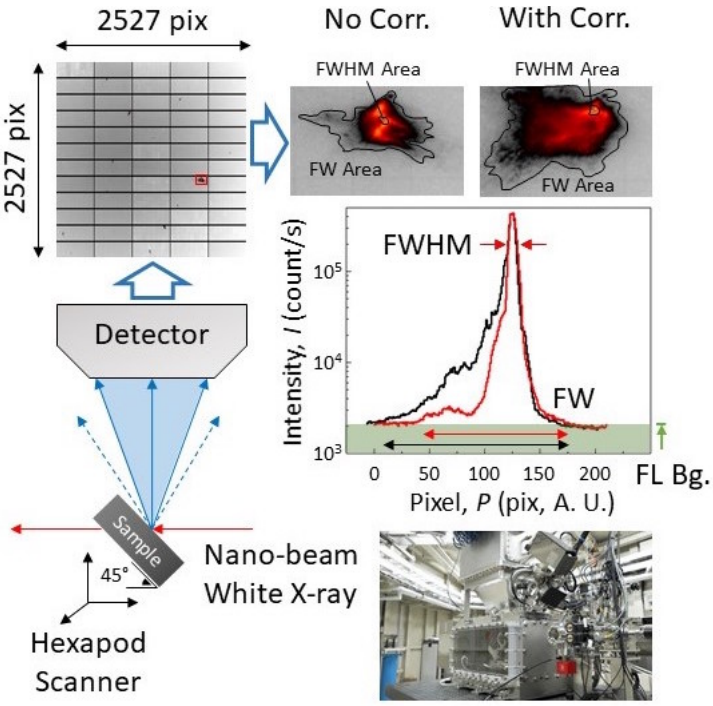

Figure 5.10: ***Taiwan Photon Source Beamline 21A set-up.*** *The white light beam is directed through the sample at a tilt angle of 45°, and diffraction beams are subsequently recorded with a 2527x2527 pixel detector sitting at the top of a high vacuum chamber. Diffraction pattern can be recorded as 2D intensity profile, allowing to measure both the Full Width at Half Maximum (FWHM), as well as low intensity broadening of the peak, measured as Full Width (FW). An image of the end station is shown as well.*

Crystal structure and defects at corroded areas. Apart from the local geometric factors in a crevice environment another contributing factors to corrosion are the crystal or grain structure and stress. To evaluate how defects contribute to local corrosion we further studied corroded regions of rSFA samples with nano Laue diffraction (LD). This method is able to provide locally resolved stress and dislocations density maps for any crystallographic plane after corrosion occurred.

Fig. 5.11 shows results of the nano-Laue diffraction based analysis for the region where corrosion initiated for the $Ni_{75}Cr_{16}Fe_9$ alloy. The indexed scattering patterns (see **fig. 5.12**) confirm that the alloy structure is a nickel-based face centered

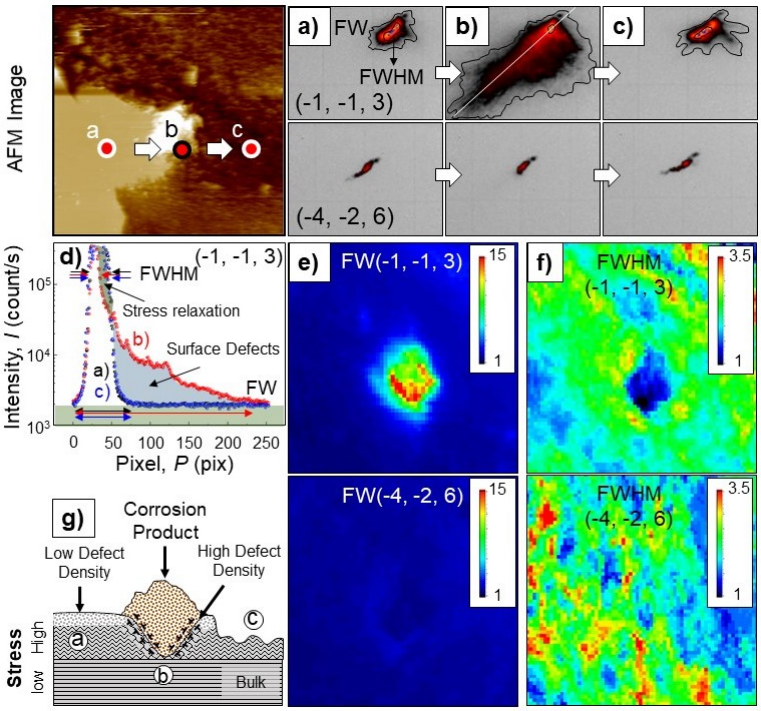

Figure 5.11: Nano-Laue X-ray diffraction analysis. Characteristic Laue scattering pattern of two characteristic orientations (-1, -1, 3) and (-4, -2, 6) are plotted in ***(a-c)****. These pattern were acquired at locations indicated in the AFM image. Variation of the peak shapes are also shown in* ***(d)*** *as line profile plotting pixel number against logarithmic intensity. Any change of the full width (FW) and full width at half maximum (FWHM) of the scattering peak relates to surface defects size of cristalline domains respectrively. In* ***(e,f)*** *FW and FWHM of the Laue peaks are plotted as a function of the location, corresponding to the area shown in the AFM image. A schematic interpretation of results is illustrated in* ***(g)*** *(c.f. text for details).*

cubic (fcc) crystal structure with some nickel atoms replaced by chromium and iron).

A detailed analysis of nano-LD intensity and specifically of the shape and distribution of the pattern on the 2D-detector further provides information on *Full Width* area (FW), corresponding to the surface defect density, and *Full Width Half Maximum* area ($FWHM$) corresponding to the size of ideally crystalline domains. Specifically, the increase of the FW, which characterizes the low intensity broadening of the diffraction peak, is due to surface defects. Furthermore, internal stress in grains leads to the distortion of the entire bulk crystal structure resulting in a broadening of the FWHM. Therefore, for both FW and FWHM, an increased value indicates an increased surface defect density and an increased bulk deformation,

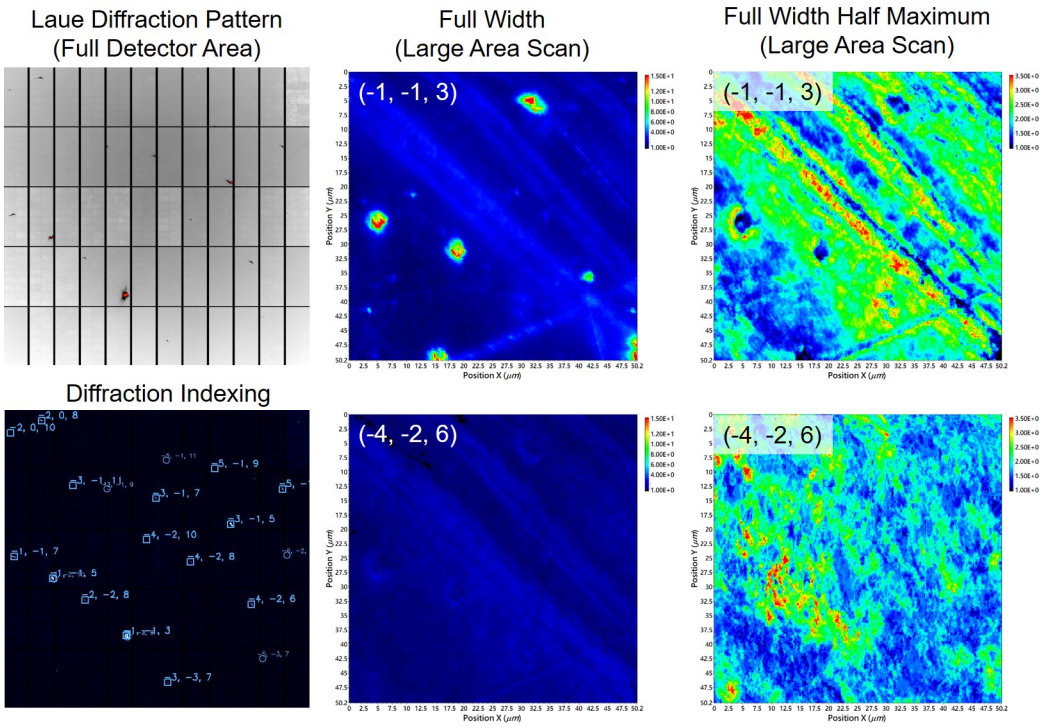

Figure 5.12: ***Diffraction indexing and mapping of the FW*** *for indicated facets over a large area (c.f. text for details).*

respectively.

For the alloy, **fig. 5.11a-c** compare the Laue peak shapes for facets (-1, -1, 3) and (-4, -2, 6) recorded at the points indicated in the AFM image shown as reference as well. Among all the diffraction peaks collected by the detector, characteristic scattering peaks **fig. 5.11a-c** are representative for all observed scattering peaks (see supporting information **fig. 5.13** for further collected peaks). These pattern indicate two interesting aspects.

First, these representative facets show a very stark difference. Facet (-4, -2, 6) shows hardly any low intensity broadening at different locations, while facet (-1, -1, 3) is very sensitive to the location. Specifically, the (-1, -1, 3) facet indicates a significant increase of the *FW*, i.e. a low intensity peak broadening, in the region at the central pit. A comparison of line scans (marked by the white indication line in **(a-c)** of the recorded intensity profile further illustrates this effect in **fig.5.11(d)**. Second, and in stark contrast to the FW, the FWHM decreases within the pit compared to outside of the pit for this facet.

Fig. 5.11e,f show a mapping of the FW and FWHM over the entire region shown

in the AFM image, respectively. This provides a 2D overview of surface defect densities and bulk lattice distortions. The results further detail how the surface defect density (FW) is significantly increased inside the pit. It is interesting, that this localized defect increase only appears for particular facets, specifically the (-1, -1, 3) and (-3, -1, 5) facets (see again **fig. 5.13**). In contrast, e.g. for facet (-4, -2, 6) and many other facets, the analysis indicates that the pit is "invisible" as compared in **fig. 5.13**).

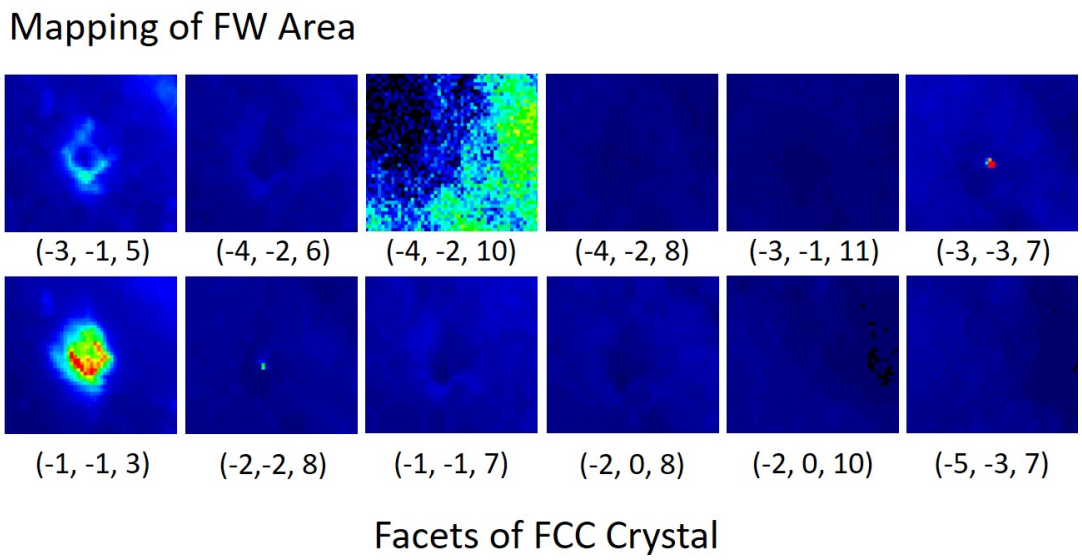

Figure 5.13: ***Mapping of the FW:*** *for different facets as indicated (c.f. text for details).*

This is a very interesting observation and general phenomenon that suggests that corrosion in the pit is fueled by surface defect migration and corrosion progression along particular crystallographic facets, here the (-1, -1, 3) and (-3, -1, 5) facets, as indicated in the schematic in **fig. 5.11g**.

Hence, we can conclude that corrosion proceeds along a particular facet of the alloy, which accumulate a higher surface defect density.

The non-intuitive finding that the FWHM appears significantly less broad in the pit region is also interesting (see **fig. 5.11f**). This suggests that a locally deeper probe volume, where corrosive damage is not yet detectable, contributes to the recorded signal. This may be due to the lower scattering cross-section of the corrosion products within the pit, suggesting corrosion products that are amorphous. This interperetation is supported by the fact that there are no additional peaks that relate to corrosion products deposited within the pit. As such, the corrosion products, that appear to be within the filled pits observed in the AFM scan, are very likely amorphous, which fits a fast reprecipitation reaction after supersaturation of the local environment in a pit.

5.3 Conclusions

In summary, rSFA provides a new and very useful tool to make very well-characterized confined areas on real samples for testing crevice corrosion initiation. It provides a detailed in-situ and real time view into a corroding crevice on bulk metals. rSFA provides detailed insight into the initial crevice corrosion mechanism. Together with a complementary set of extensive post-corrosion analyses it is possible to generate a detailed understanding of the corrosion of any bulk material. It is particularly interesting to mention, that the measured confinement geometry can potentially be modeled accurately using simulation approaches. As such, data generated in an rSFA may serve as a very well defined experimental reference for testing modeling approaches, using classical approaches potentially including machine learning algorithms. For the studied model systems, namely Ni and the $Ni_{75}Cr_{16}Fe_9$ we can summarize the following conclusions:

- The corrosion mechanism of Ni proceeds via severe roughening (from σ_{rms} = 2-3 nm to σ_{rms} = 20 nm) and pitting over the entire surface, with an increased pitting density of >180-200 nm deep pits in the vicinity of and inside the nanometer confined zone. In contrast $Ni_{75}Cr_{16}Fe_9$ shows no visual corrosion outside the confined area.
- $Ni_{75}Cr_{16}Fe_9$ exhibits two distinctly different areas in the confined region.

In the fully confined area no severe corrosion occurs and only pitting at much lower density compared to Ni is found. In contrast, within the crevice opening we find severe corrosion via merging of very dense pitting, resulting in a severely rough area with about 200 nm deep material loss within our experiment.

- The $Ni_{75}Cr_{16}Fe_9$ alloy shows the expected good corrosion resistance only outside of confinement. However, within the crevice opening more severe corrosion compared to Ni occurs due to local acidification and spreading of aggressive electrolyte within the crevice opening. rSFA allows a real-time visualization of the local corrosion process. Local acidification spreads with a rate of 17-50 μm/min, due to fast and significant proton release during passive film breakdown, which releases 10 protons per molecule of Cr_2O_3.
- Based on the material loss and in-situ progression rate of the corrosion recorded using the rSFA we can estimate the local current of $Ni_{75}Cr_{16}Fe_9$ corrosion in the crevice opening to be at least < 0.1 A/cm^2.
- Nano-LD results reveal that pit propagation proceeds along particular facets of the alloy, which may also accumulate a higher surface defect density. Also, corrosion products deposited in pits do not show any crystalline structure, indicating a fast precipitation due to saturation of the local environment.

Chapter 6

EC-ICP-MS

Here in this chapter, we investigated the corrosion mechanism of different nickel based alloys, discussed in the previous chapter in order to have a clear understanding of the corrosion process. Experiments are performed with an the Inductive Coupled Plasma-Mass Spectrometry (ICP-MS) with its reaction cell, that I will briefly introduce, then I will explain the conditions in which we performed the different experiments and after I will comment on different systems that were investigated. First we performed the ICP-MS experiments on the same alloy that was discussed in the previous chapter ($Ni_{75}Cr_{16}Fe_9$) to have a better understanding of the corrosion mechanism, by performing the experiment in both aerated and argon rich environment in order to replicate the crevice conditions. Those measurements enabled us to confirm our hypothesis regarding the corrosion mechanism discussed in the previous chapter. After, we tuned the experimental conditions, by varying the pH, the concentration and the electrolyte to further confirm our hypothesized mechanism. Once we were able to confirm it, we started to tune the concentration of the chromium and molybdenum in the samples, to have a better understanding their role in the protection of the nickel alloy and to identify further interesting substrates for the SFA studies.

The following chapter is based on the submitted article "Time resolved elemental dissolution rates during transpassive anodic polarization of nickel base alloys in the presence of chloride". This chapter contains parts of text and graphics of said article. The author's contribution includes execution and analysis of all experiments, design of research, discussion of all experimental results, and article writing.

6.1 Introduction

As I already pointed out in previous chapters, the real-time analyses of a corroding system, is demanding and crucial in order to prevent possible failure in the material and to further understand its mechanism. We have seen how MBI can be used to see CC in real time; but what we can not see is quantitative chemical dissolution. When an electrochemical cell is coupled with an Inductive Coupled Plasma-Mass Spectrometry (ICP-MS) it is possible to continuously keep track of the ions released from the surface and have an understanding of the kinetic of the system. Shkirskiy *et. al* described the relation between the time dissolution, the reaction happening at the surface and the flow stream [120]. Here, we performed online chemical analysis of corrosion products using a flow cell coupled with an ICP-MS [121],[122], [123] to further characterize the corrosion mechanism of the nickel based alloys in oxygen-rich and oxygen-depleted conditions, mimicking conditions outside and inside of a crevice, respectively.

As already mentioned in previous chapters, nickel alloys are used in a wide range of applications because of their versatility and resistance to corrosion. Unique properties such as high corrosion and temperature resistance, combined with low thermal expansion rates, render nickel base alloys essential and uniquely tailored for a wide range of applications. These include for instance application in steam turbine and nuclear power plants, in medical devices and implants or in petrochemical industries. The unique corrosion resistance of nickel base alloys is due to their ability to form a stable oxide film, which maintains the alloy in a meta-stable state of passivity during anodic polarization. Among all the elements, chromium and molybdenum are the one considered to enhance those characteristics. Many studies were conducted and published in this direction to explain the passivation and the composition of the passive oxide, since the kinetic and stability of the oxide is dependent on this alloying elements. These results based on XPS and AES, showed that the chromium is forming an oxide layer rich to enhance the passivity. It is from literature known, that the role of the chromium is to increase the passivity region, so to delay the pitting potential of the metal, while the role of the molybdenum is to prevent the dissolution of the nickel and iron. Among the multiple theories, regarding the role of molybdenum to prevent corrosion the main one remain:

- the idea that Mo tend to migrate to local defect of the surface and prevent the site to act as a dissolution location
- it postpones the local dissolution because of its high capability of forming high strength metal-metal bonds.

Specifically, passive film formation is promoted by alloying with elements such as chromium, or molybdenum, which can additionally release corrosion inhibiting MoO_4^{2-} ions into solution during passive and transpassive dissolution. [124] On nickel base alloys chromium forms very stable passive layers of well-adhering Cr_2O_3 covered by small amounts of $Cr(OH)_3$ as well as $Ni(OH)_2$.For instance, work by Maurice et al.[125] implied that corrosion of nickel base alloys proceeds via the transport Ni through the oxide layer, and release of Ni^{2+} into the solution. Further, the stability of the passive state is considerably lower when nickel alloys are polarized above some critical electrode potential in environments containing certain aggressive ions (e.g. chloride ions). In such environments a corrosive degradation known as pitting and or crevice corrosion can appear. During this type of corrosion local breakdown of the passive oxide during anodic polarization results in conditions where the bare alloy surface is unable to repassivate, which defines the onset of the transpassive degradation of the material. Kinetics of transpassive dissolution processes are essential to understanding the pitting and crevice corrosion behaviour of nickel base alloys. While much work was performed to characterize corrosive degradation under various conditions, [107] an elemental resolved understanding of transpassive dissolution mechanism and oxide break down still remains unexplored.

It is our aim to utilize ICP-MS to study the time-resolved release of elements into solution in-situ during anodic polarization of a series of model nickel base alloys. Specifically polarization into the transpassive region and above potentials where passivity fails are of interest in this work. In the recent years different combinations of spectroscopy (e.g. atomic emission spectroscopy,[109, 123] ICP mass spectrometry, [121] or UV-VIS) coupled with electrochemical flow cells were established and tested as powerful in-situ spectro-electrochemical methods, that can provide and elemental resolved real-time view into corrosive processes. [120]

Most designs of flow-cell spectrometry couplings include and o-ring pressed onto a sample in order to seal the flow cell, which may provoke crevice corrosion as a main failure mechanism. For testing nickel alloys this is even beneficial, as the expected corrosion mechanism is localized corrosion. However, it is important to consider this in the design of a spectro-electrochemical flow cell method. Therefore, we implemented a new design for a ICP-MS flow cell, which incorporates an Avesta type sample mounting,[123] where an O-ring is not directly pressed on top of the sample, in order to avoid or specifically design for crevice formation during measurement (see **fig. 6.1a**). We study pH dependence and oxygen levels effects on the transpassive dissolution of passive films on nickel base alloys.

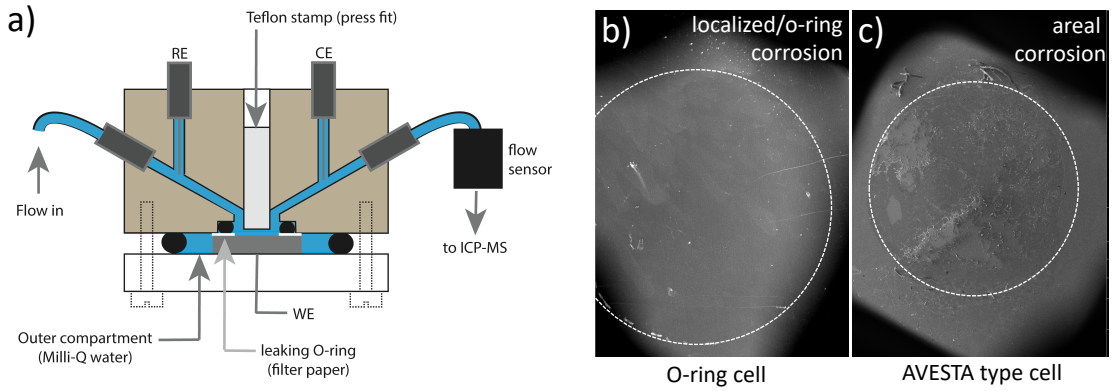

Figure 6.1: ***a)*** *AVESTA type flow cell for coupling with an ICP-MS. An inner "leaking" o-ring of 3 mm diameter presses via a filter paper onto the sample (working electrode (WE)). As a reference electrode (RE) Ag|AgCl is used, and as counter electrode we use a Platinum wire (CE). An outer O-ring forms a Milli-Q water filled compartment. The flow is pumped through the system with a regulated pressure of around 150 bar and the recorded flow is kept constant by monitoring the output of the flow sensor The electrolyte is then directed to the ICP-MS, giving as as an output counts against time.* ***b)*** *SEM image of sample corroded in a cell without the outer compartment indicating localized corrosion at the o-ring, and* ***c)*** *with a leaking o-ring, indicating preferential corrosion over the entire exposed area due to the lack of confinement.*

6.2 Inductive Coupled Plasma-Mass Spectrometry

Inductively coupled plasma mass spectrometry (ICP-MS) is a type of mass spectrometry which is capable of detecting elements in really low concentration such as 1 in 10^{15} (ppq). The sample is ionized with inductively coupled plasma and then the ions are separated and quantified using a mass spectrometer. A schematic of the ICP-MS is shown in **fig. 6.2**: the sample is introduced as a liquid which is converted into a type of aerosol by a nebulizer. The sample will then be guided through the plasma where they are converted into ions. The plasma used is mainly made of argon gas $\mathrm{Ar} \rightarrow \mathrm{Ar}^+ + e^-$. The required energy for this reaction is obtained by pulsing an alternating electric current through wires that surround the argon gas. After the sample is injected, the plasma's extreme temperature causes the sample to separate into individual atoms $\mathrm{M} \rightarrow \mathrm{M}^+ + e^-$ so that they can be detected by the mass spectrometer.

The high temperature of the plasma is enough to convert a large percentage of the sample into ions, however this fraction depends on the ionization potential. The

sample is then carried through a cone made of copper with an entrance diameter of 1 mm and then through a skimmer-cone of nickel with an entrance diameter of 0.8 mm; the latter cone is constantly cooled to keep its temperature beneath that of the plasma. Once the ions have passed the skimmer-cone, they are focused through lenses that have a constant electric field and accelerate through a reaction/collision cell which is filled with helium, so that if some oxides are formed, they are reduced carried out.

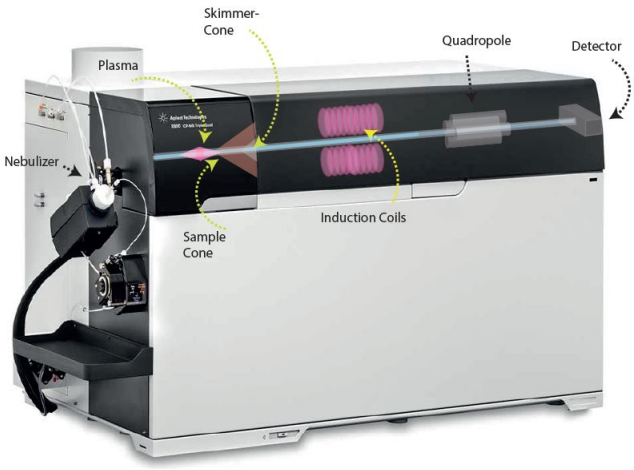

Figure 6.2: ***Components of the ICP-MS*** *The main parts of the ICP-MS are the nebulizer, where the sample is introduced and go through the plasma. After, the mixture goes through the sample cone and the skimmer cone. Once the ions have passed through they are directed, with the help of induction coils, to the quadropole and afterwards to the detector.*

ICP-MS in corrosion

ICP-MS can be used to study corrosion, in order to understand which elements are more prone to dissolve first in real time. As an example, if we consider an alloy containing chromium and molybdenun, since these two elements are known for protecting the surface, we are expecting a lowering of the dissolution rate of the material when they start to leach out.

Fig. 6.3 shows a schematic of the experiment setup: the electrolyte is constantly flowing into a home-built cell with a modified Ogle-design [123] made of PEEK (see **fig. 6.1**) and the flow of the solution over different samples is assured to be maintained constant using a home-built pressure regulator, and it is monitored

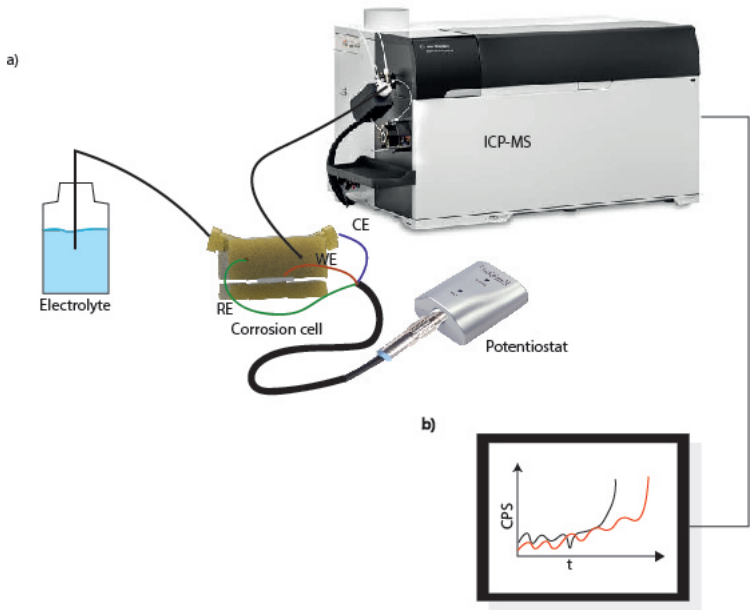

Figure 6.3: ***EC-ICP-MS:****the electrolyte is pumped through the cell with a pumping system; the electrochemistry is recorded with a potentiostat, EMSTAT 3^{+}. The resulting solution is directly guided inside the ICP-MS.*

by a micro-fluidics pressure sensor (MPS from Elveys). The outlet of the cell is directly connected to the ICP-MS (7900 Agilent Technologies). The instrument is calibrated using standard tuning solutions obtained from Agilent. The time lag from the active cell area to the ICP-MS analysis is typically about 10 seconds, and the observed ion flow profiles resemble log-normal distributions[120]. The output we get from the instrument is the number of counts (for every single element) in relation to time.

6.3 Results and discussion

In this section we show and discuss corrosion characteristics for a set of different nickel base alloys during transpassive degradation of the materials. We start the discussion with a comparison of different chromium content of NiCrFe based model alloys, and later compare the behaviour to various nickel base alloys containing molybdenum.

The first experiment we performed was a post analyses of the solution collected after the SFA experiment were the potential was ramp up at rate of 1 mV/s (see

fig. 6.4). The experiments was performed on the same alloy, described in the previous chapter $Ni_{75}Cr_{16}Fe_9$.

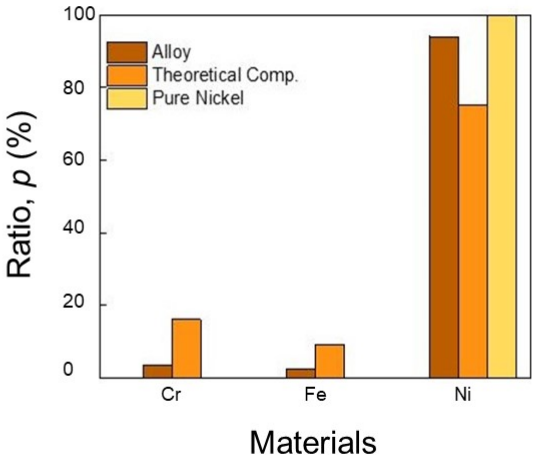

Figure 6.4: ***Ratio of the components of the alloy in stagnant solution:****interestingly, here we observed an higher dissolution ratio of the nickel compared to the effective composition and a minor dissolution regarding the chromium and iron, leading us to think that the oxide left on the surface will be richer in chromium and iron compared to nickel. These hypothesis find its confirmation in the XPS data, that were discussed in the previous chapter (see* ***fig. 5.8****)*

However, as stated before, the real power of this technique is to be able to solve element analysis in real time. Therefore, we performed experiments in that sense, in order to analyze the different rate and time in dissolution of the different elements. Interestingly, the kinetic varied substantially according to the environmental conditions and the percentage of the element in each material. Here I will first discuss the data regarding the $Ni_{75}Cr_{16}Fe_9$ alloy in 1mM NaCl.

NiCrFe based model alloys. **Fig. 6.5** shows the time resolved elemental analysis of electrolyte flowing over $Ni_{75}Cr_{16}Fe_9$ during 1 mV/s anodic polarization. The electrolyte flow rate is 0.3 mL/min, with a time delay of 10 seconds from passing through the electrochemical cell to injection into the Plasma.

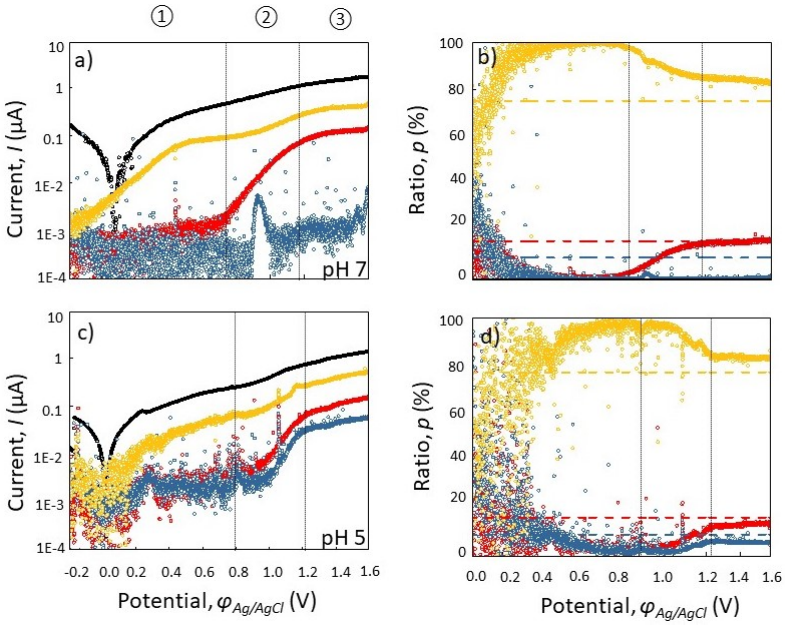

Figure 6.5: ***ICP-MS spectro-electrochemistry of*** $Ni_{75}Cr_{16}Fe_9$ ***in argon bubbled 1 mM NaCl solution :a/b*** *at pH = 7 and at* ***c/d*** *pH = 5. Elements are color coded as: yellow circles for nickel, red for chromium and, blue for iron. The black circles represent the electrochemistry. The ICP-MS data and the electrochemistry one are aligned and taking in consideration the possible delay. Panels* ***a)*** *and* ***c)*** *show the recorded transients and the elemental currents derived from ICP-MS. Panels* ***b)*** *and* ***d)*** *show the mass ratio of the elements derived from ICP-MS on the total mass.*

Here, we first test polarization in oxygen depleted environments **a-b)** in a neutral and **c-d)** slightly acidic pH 5.0 in 1 mM NaCl solutions. In **a)** and **c)**, the collected metal species during the corrosion experiment were converted into a current using expected charge transfer numbers (Ni/Ni^{2+}: 2, Cr/CrO_4^-(VI): 6 and Fe/Fe^{2+}: 3), and plotted together with the total electrochemical current measured. To further investigate the relation between the dissolved materials at different stages, the ratio between the dissolved ionic species were plotted in **b)** and **d)**.

As indicated in **fig. 6.5** there are three distinctly different regimes. We define these regimes as follows. First, in *regime 1* the passive film is stable, and mainly dissolution of materials across the passive film is observed. Second, in *regime 2* the dissolution of the passive film is indicated by the onset and steep increase of elemental currents from the passive film forming elements. Finally, in *regime 3* the dissolution rate recorded in ICP-MS establishes a stable rate that does not change with increasing the potential. Here, the material is in the transpassive region, and no passive film protects the bare metal from electrochemical disintegration.

In *regime 1* $Ni_{75}Cr_{16}Fe_9$ shows very low and exclusively nickel dissolution at both pH values, with an increasing dissolution rate at more anodic potentials. The observed behaviour can be rationalized by inspecting the Pourbaix diagrams of nickel, chromium and iron. Accordingly, nickel dissolution is expected at all applied potentials and pH values applied here, as follows:

$$Ni_{(s)} \rightarrow Ni^{2+}_{(aq)} + 2e^- \tag{6.1}$$

On the other hand, at pH 7 and pH 5 the dissolution of chromium and iron oxides is not expected, and it is also observed to be very close to the detection limit. At both pH value the stable species of chromium and iron are Cr_2O_3 and Fe_2O_3 oxides, respectively, according to a Pourbaix diagram. Given the thermodynamic stability, the observed small currents are likely related to chemical dissolution into the flowing electrolyte, rather then electrochemical degradation.

The *second regime* is characterized by a significant increase of Cr-dissolution rates at pH 7 and 5, while only at pH 5 stable iron dissolution is established during further anodic polarization. At pH 7 iron dissolution rates remain very low and never reach expected bulk ratios. Passive film breakdown initiates at 0.7 V ϕ_B as indicated by a sudden and significant increase of the chromium dissolution rate, until a constant elemental dissolution rate is reached (**regime 3**). In the third regime a stable trans passive dissolution current is established and the ratio of corrosion products dissolving into solution remains constant.

Interestingly, the chromium and iron dissolution rates show a seemingly unexpected behaviour. The pH 7 case exhibits Cr-dissolution and very limited Fe-dissolution at $\phi_B = 0.95$ V. In stark contrast, the significant Cr-dissolution in the more acidic case is accompanied by a fast and significant Fe dissolution, occurring at higher onset potentials $\phi_B = 0.8$ V.

The breakdown of chromium oxide at pH 7 is expected at $\phi_B = 0.6$ V vs. Ag|AgCl, while it is expected at $\phi_B = 0.75$ V at lower pH mV vs .Ag|AgCl. This agrees very well with the observed breakdown potentials and the expected anodic shift of the oxide breakdown at the lower pH, based on Pourbaix diagrams. The dissolution of chromium proceeds at both pH values as follows:

$$\mathrm{Cr_2O_{3(s)} + 5H_2O_{(l)} \rightarrow 2CrO_4^{2-}{}_{(aq)} + 6e^- + 10H^+_{(aq)}} \tag{6.2}$$

Accordingly, a strong acidification of the interface occurs during the Cr-oxide

breakdown. The increased iron dissolution at the lower pH value is in line with the faster passive film breakdown and the more effective local acidification of the interface region. According to the Pourbaix diagram of iron, Fe_2O_3 only dissolves as Fe^{3+} at pH 3.6 above 0.7 V. This acidification is five times more effective compared to acidification via Ni-dissolution due to the release of the 10 protons. In addition, the oxide breakdown proceeds at higher potentials at lower pH, which is expected. But at the same time the kinetic of the passive film break down is faster and in competition with diffusion and migration of protons away from the interface the local pH can establish a lower value during passive film breakdown, which effectively also dissolves Fe_2O_3. This also suggest that the electrochemical dissolution of Cr_2O3 at pH7 proceeds gradually at lower applied potentials, as observed in the ICP-MS data, with only a moderate decrease of the local pH. No strong acidification occurs explaining the slow electrochemical degradation of the Cr_2O_3 in deaerated environments in ICP-MS.

Interestingly, if the polarization is performed in aerated, oxygen containing, electrolyte, we find a completely different and unexpected behaviour. **Fig. 6.6** shows that the transpassive dissolution of the passive film has a similar onset compared to the deaerated case. However, the kinetics are completely different. Instead of a gradual transition towards bulk ratio dissolution, data indicates a very abrupt breakdown of the passive film, and a limited ability to maintain or reform a passive film during polarization. This suggests, that the oxygen plays a crucial role in the degradation of the oxide film. At first, this seems to be at odds with the fact, that chromium is already oxidized in the passive film. However, in the transpassive dissolution (regime 3), according to the Pourbaix diagram, Cr_2O_3 is further oxidized to chromate, CrO_4^{2-}. Hence, the data suggests, that oxygen or possibly a reaction intermediate of the oxygen reduction, which also may occur at this interface, is promoting an accelerated electrochemical degradation of the passive film. A similar transpassive breakdown behaviour may be expected for many alloys that are protected by a Cr_2O_3 passive film.

Fig. 6.7 shows the elemental dissolution rates during polarization of $Ni_{86}Cr_5Fe_9$ at pH 7 in aerated and dearated conditions, respectively. As expected, the lower chromium content results in a very severe corrosive reaction for both conditions. In contrast to the alloy with 16% chromium, already at 0.3 V a clear critical potential is observed, with an increase of current over one order of magnitude. At this point, the protective film breaks down with very fast kinetics, irrespective of oxygen levels in solution. Above 0.5 V the transpassive dissolution proceeds with bulk ratios of the alloying elements (*region 3*).

This data confirms expectations, that chromium levels below 10% do not result in a sufficiently stable chromium oxide layer. The data indicates that a $/Cr_2O_3$ layer

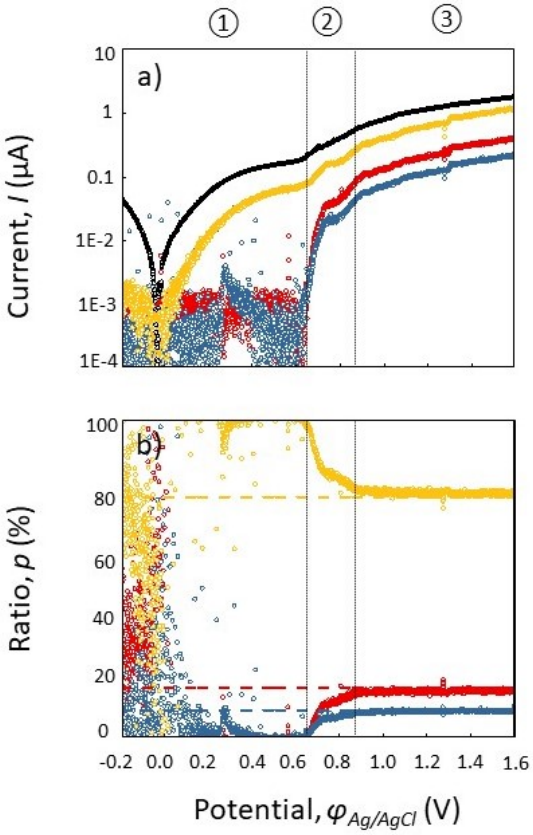

Figure 6.6: ICP-MS spectro-electrochemistry of $Ni_{75}Cr_{16}Fe_9$ in aerated 1 mM NaCl solution at pH =7 and at c/d)) pH 5. Panels b) shows the mass ratio of the elements on the total mass derived from ICP-MS. Elements are color coded as: yellow circles for nickel, red for chromium and, blue for iron. The black circles represent the electrochemistry.

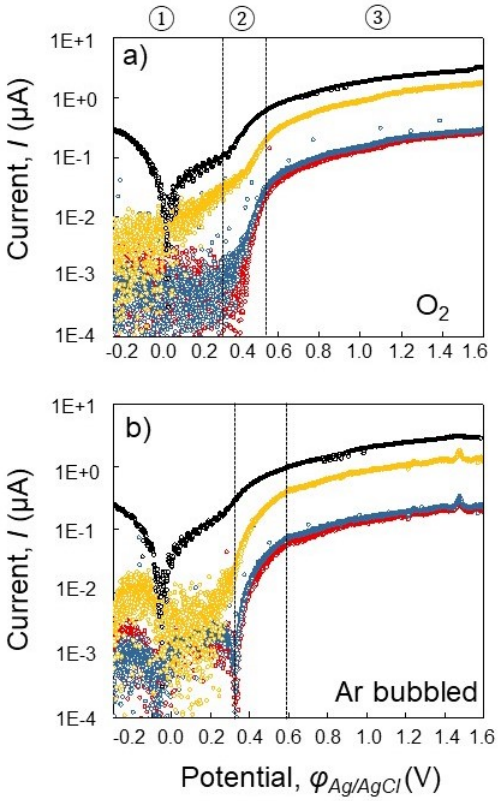

Figure 6.7: ICP-MS spectroelectrochemistry of $Ni_{86}Cr_5Fe_9$ in aerated ***a)*** *and* ***b)*** *Argon bubbled 1 mM NaCl solutions at pH 7 respectively. The regimes 1-3 are indicated according to the definition in* ***fig. 6.5****. Elements are color coded as: yellow circles for nickel, red for chromium and, blue for iron. The black circles represent the electrochemistry.*

is still present at this chromium level, however the layer breaks down with faster kinetics and at lower potentials then expected from a Pourbaix diagram of Cr. This breakdown at lower potentials is interesting, as it suggest that the layer is possibly a defect rich or incomplete Cr_2O3 layer, containing significant amounts of other elements, defects or locally different oxide structures (including possibly lees protective nickel oxides). The electrochemical breakdown of Cr_2O3 is expected at 0.7 V. In contrast to $Ni_{75}Cr_{17}Fe_9$, which does break down close to the expected potential, this finding suggests that the higher chromium content is necessary to for forming a compact, and defect free Cr_2O3 layer.

Influence on molybdenum. **Fig. 6.8a**and **b** shows the elemental dissolution rates during polarization of $Ni_{74}Cr_{16}Fe_9Mo$ at pH 7 in aerated and deaerated conditions, respectively. As expected, addition of 1% molybdenum improves the corrosion resistance of the alloys considerably. The spectro-electrochemical data indicates that the onset of the passive film break down is shifted to 0.9 V vs. Ag|AgCl, which is 300 mV above the expected breakdown for Cr_2O_3. The break down exhibits fast kinetics and bulk dissolution ratios are established at about 1 V vs Ag|AgCl. Compared to $Ni_{75}Cr_{16}Fe_9$ there is no significant influence of oxygen on the break down kinetics at 0.9V. Here, the influence of oxygen is quite different, and mainly moderated the nickel dissolution rates. Specifically, in oxygen containing environments we find significantly less nickel dissolution. This may be due to the ongoing oxygen reduction, which can result in locally higher pH values at the surface, and hence nickel hydroxide precipitation. **Fig. 6.8c/d** compares $Ni_{74}Cr_{16}Fe_9Mo$ corrosion behaviour to commercial high molybdenum content alloys B2 ($NiMo_{30}$ plus up to 1% other elements) and C276 ($NiCr_{15}Mo_{16}Fe_6$ plus up to 5% other elements) at pH 7 in aerated conditions, respectively. C276 shows excellent passivity, comparable to $Ni_{74}Cr_{16}Fe_9Mo$. The onset of transpassive oxide break down occurs at 0.9 V vs. Ag|AgCl. Interestingly, C276 never reaches bulk elemental dissolution ratios during polarization into the transpassive regime above 0.9V. This is indicative of a continuous repassivation of the material during corrosion. The passive film on C276 is never fully dissolved, and the bare alloy is not exposed to the corroding solution. This is interesting as it suggests that the higher molybdenum content leads to the formation of a passive film with high stability in the region were the other alloys are transpassive. Within the tested range, C276 never reaches conditions of trans-passivity, defined by a sustained dissolution of material at elemental composition. As expected B2 **fig.6.8 e)** exhibits no corrosion resistance during anodic polarization. B2 is even less corrosion resistant compared to pure nickel. It is designed as an alloy for reducing conditions. It is however interesting to include it in this comparison with other Mo-containing alloys. The increased corrosion resistance of C276 is hence not due to formation of

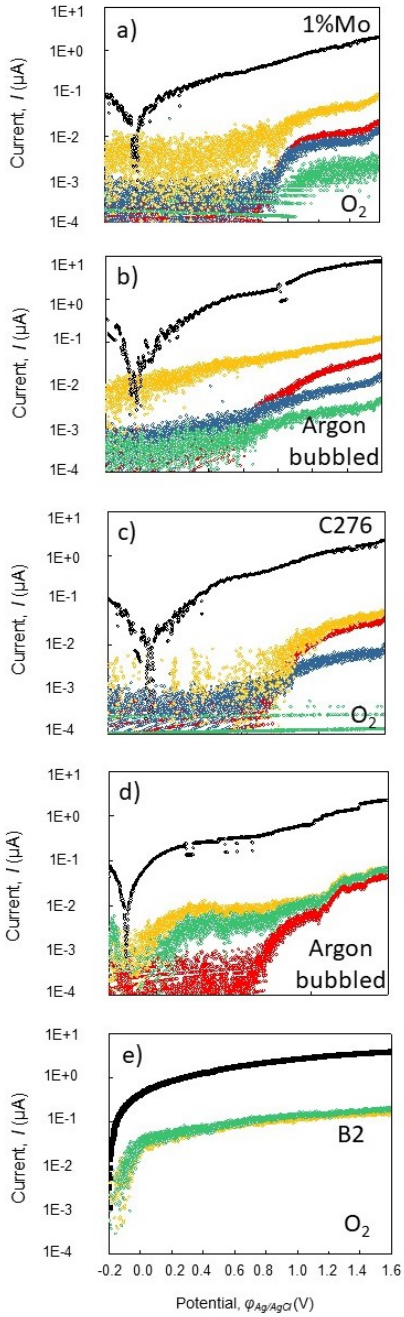

Figure 6.8: ICP-MS spectroelectrochemistry of $Ni_{84}Cr_5Fe_9Mo_1$ ***a)*** *in aerated* ***b)*** *and Argon bubbled 1 mM NaCl solutions at pH 7. Data for the commercial alloy C276 is shown* ***c)*** *in aerated and* ***d)*** *deaerated 1 mM NaCl solutions.* ***e)*** *shows data for the B2 alloy as comparison in aerated 1 mM NaCl. Elements are color coded as: yellow circles for nickel, red for chromium, blue for iron and, green for molybdenum. The black circles represent the electrochemistry.*

any molybdenum rich oxide film. Molybdenum and chromium exhibit a synergistic effect, possibly via increasing the passive film formation kinetics at high anodic potentials. The mechanism of this synergy effect remains illusive, and warrant further studies.

6.4 Conclusions

We characterized time resolved elemental dissolution rates during anodic polarization of a series of nickel base alloys. The selection focused on characterizing the synergistic effect of chromium and molybdenum. In general, ICP-MS proves to be well suited to characterize the onset of an anodic oxide breakdown and the onset potential of the transpassive region. We define the onset of the transpassive region as the potential above which bulk ratio dissolution rates are established in the ICP-MS data. The transition region is indicative of the competition between repassivation and localized complete passive film breakdown with bulk metal exposure. The following specific conclusions can be drawn for the alloys used.

- For the $Ni_{84}Cr_5Fe_9$ alloy passive film breakdown occurs at 300mV more cathodic potentials compared to $Ni_{84}Cr_5Fe_9$, indicating and incomplete or defect rich passive film.
- $Ni_{84}Cr_5Fe_9$ exhibits a stable passive film, which breaks down at the potential where Cr_2O_3 is expected to break down. Also, the breakdown potential shifts to higher values according expectations from Pourbaix diagrams for Cr_2O_3. This is indicative of a stable Cr_2O_3 oxide film formation with thermodynamic properties of neat Cr_2O_3, without defects, or significant deviations due to presence of other elements.
- Oxygen promotes an accelerated electrochemical degradation of passive Cr_2O_3 films, and apparently plays an important role in the reaction pathway of transpassive oxide breakdown of Cr_2O_3 passive film if no molybdenum is present.
- This also suggests, that corrosion protection in confined zones, where oxygen is depleted, is improved due to slower dissolution kinetics of the passive film. This may have implications for crevice corrosion protection strategies.
- Passive film break down of molybdenum containing alloys is considerably shifted to higher potentials by about 300 mV compared to materials without NiCrFe alloys without Mo.

- Also nickel dissolution rates are lower for molybdenum containing alloys, in oxygen environments.
- Synergistic effects of high amounts of molybdenum (C276) on Cr_2O_3 repassivation kinetics considerably extend the onset of transpassive dissolution beyond potentials of 1.6 V applied in this work.

Conclusions of ICP-MS in relation to SFA experiments of CC

As explained previously, crevice corrosion can be very detrimental for some materials, especially due to the fact that it can be very difficult to detect. In previous chapters I underlined how important it is to understand how the metal dissolution starts, through visualization with SFA coupled to electrochemistry. However, what was missing, was a deeper understanding of the corrosion mechanism and how different elements in nickel alloys and environmental conditions can influence it.

In **chapter 5**, we saw the different corrosion mechanisms of pure nickel and the NiCrFe alloy. From literature we would expect the alloy – bearing the chromium – to be more corrosion resistant. Even if we did observe a significant shift of the corrosion potential **fig. 5.2** in the electrochemistry measurements, SFA **fig. 5.3** and AFM **fig. 5.9** analysis showed the surface of the alloy to be more damaged.

We found that during the corrosion process of the alloy there was the formation of a roughened area with 200 nm material loss. We attributed this mechanism to the dissolution of the chromium oxide and the rapid decrease of the pH in the confined area. In this chapter, ICP-MS experiments provided confirmation that the dissolution rate of the alloy increases dramatically with the breakdown of the chromium oxide. Unlike *nickel*, that starts to dissolve even at low potentials, we confirm the role of the *chromium* in protecting the iron as it only dissolves once the chromium oxide breaks down.

A second interesting detail from ICP-MS data is that oxygen promotes an accelerated electrochemical degradation of passive Cr_2O_3 films. This should actually be beneficial for crevice corrosion resistance, where oxygen is depleted locally. As such, Cr_2O_3 is a good passive layer for preventing crevice corrosion: In ogygen depleted environments its breakdown is slowed down.

Chapter 7

Conclusions and Outlook

Here are reported the general conclusions of this work. The more specific one, are already addressed at the end of each individual chapter.

In this work we adapted multiple beam interferometry to study corrosion and we integrated it in a surface force apparatus (SFA) implemented with electrochemistry both in reflection and transmission mode.

We first tested the proof of principle, working with thin layer of metal films, and seeing that the technique was able to give us information regarding the initiation and the local current. Compared with standard optical microscopy with transparent crevice formers, the depth resolution of evolving initial corrosive degradation is superior, allowing measurement of pit depths in 3D with subnanometer and millisecond time resolution. Also, the EC-SFA uniquely enables measurement of single pit-current densities and growth shapes in 3D (both laterally and in depth), as well as time-evolving pit densities within the confined zone. Local currents originating from reactions within the confined zone (with single pit resolution), and currents from outside the zone can be uniquely differentiated using the EC-SFA technique. Direct comparisons with quantitative theoretical models of the initiation of crevice corrosion for other metal and alloys systems, enabling direct characterization of initial crevice corrosion mechanisms, can be made.

Once we understood how to exploit those characteristics, we extended the apparatus to bulk materials, by using the SFA in reflection mode. Here, we were still able to calculate the local current and to follow the corrosion process in real time. Together with a complementary set of extensive post-corrosion analysis it was possible to generate a detailed understanding of the corrosion of any bulk material. Particularly interesting was the difference in the corrosion mechanism between the bare nickel and the nickel alloy.

As a final step, we performed chemical dissolution time resolved with inductive coupled plasma spectrometry (ICP-MS). Here we were able to isolate the role of single elements in preventing corrosion. Extending our studies to other alloys commonly used in industry we have shown that chromium is able to postpone the dissolution potential to higher values, and that when the chromium oxide breaks down it is the role of molybdenum to repair it, but an alloy without chromium and just molybdenum is even less resistant than the pure nickel itself.

At the end of this journey, I hope to have convinced the reader of the power of multiple beam interferometry in studying corrosion. Despite the fact that during this work we were able to answer some important questions regarding crevice corrosion, on the other hand we probably opened the road for even more questions.

Some further areas of research could include the following:

- a 3D modelling of the confinement area, with the information obtained from the Newton's rings in parallel with the FECO. In this way, it would be possible to fully characterize it and implement the 3D confined geometry into simulation of corrosion in order to see how the different parameters such as confinement area and liquid thickness would affect the metal dissolution. A machine learning algorithm could then be applied in order to predict, by just looking at the confinement geometry, where and how severe the damage to a metal surface could be.
- Another possibility is to further study the mechanism of corrosion of alloy C276 in a SFA, since its capability to resist corrosion, as fully characterized in chapter six, makes it a good system for referencing similar alloys against. In chapter five we saw that it was possible to use rSFA for crevice corrosion of bulk material; to follow the corrosion mechanism from a visualization point of view and hence derive the local charge and material dissolution.
- On the other hand in chapter six we saw that the ICP-MS provided us with information regarding the chemical mechanism of corrosion, therefore, it would be ideal, to have the simultaneous analysis of the visualization and chemical mechanism by coupling the two set ups.

This thesis has hence laid the ground work to perform very detailed experiments on corrosion in confinement, to develop a mechanistic understanding as a function of the alloy composition.

Bibliography

[1] W Betteridge. *Nickel and its alloys*. Ellis Horwood ; Halsted Press, 1984. OCLC: 10914817.

[2] Nickel Institute. Nickel and sustainability. url: https://www.nickelinstitute.org/en/nickelmagazine/magazinehome/allarchives/current/volume33-2.aspx. 2018-11-21.

[3] Samuel J. Rosenberg. *Nickel and Its Alloys*. National Bureau of Standards, 1968.

[4] Nickel Institute. Nickel metal the facts. url: https://www.nickelinstitute.org/nickeluseinsociety/aboutnickel/nickelmetalthefacts.aspx. 2018-11-21.

[5] J. Fuller and R.T. Carlin. In situ optical microscopy investigations of lithium and sodium film formation in buffered room temperature molten salts.

[6] Herbert H. Uhlig. The cost of corrosion to the united states. *Corrosion*, 6(1):29–33, January 1950.

[7] National Academy of Corrosion Engineers. International measures of prevention, application, and economics of corrosion technologies study. url: http://impact.nace.org/documents/nace-international-report.pdf.

[8] P. of National Academy of Corrosion Engineers Virmani. Corrosion costs and preventive strategies in the united states. url: https://www.nace.org/uploadedfiles/publications/ccsupp.pdf, Aug 2002.

[9] U.R. Evans. The corrosion and oxidation of metals: Scientific principles and practical applications. *Journal of Chemical Education*, 1960.

[10] M. Pourbaix. Atlas electrochemical equilibria in aqueous solution. *National Association of Corrosion Engineers*, 1974.

[11] P. Marcus and J. Oudar. *Corrosion mechanism in theory and practice*. Marcel Dekker Inc., 1995.

[12] J. Kruger and S. Begum. Corrosion of metals: overview. *Science and material engineering*, August 2016.

[13] C. Y. Chao, L. F. Lin, and D. D. Macdonald. A point defect model for anodic passive films i: film growth kinetics. *J. Electrochem. Soc.*, 128(6):1187–1194, 1981.

[14] L. F. Lin, C. Y. Chao, and D. D. Macdonald. A point defect model for anodic passive films ii: chemical breakdown and pit initiation. *J. Electrochem. Soc.*, 128(6):1194–1198, 1981.

[15] Glyn F. Kennell, Richard W. Evitts, and Kevin L. Heppner. A critical crevice solution and ir drop crevice corrosion model. *Corrosion Science*, 50(6), June 2008.

[16] R. G. Kelly and J. S. Lee. *Localized corrosion: crevice corrosion.* Elsevier, Oxford, January 2018.

[17] R.B. Mears and U.R. Evans. Corrosion at contact with glass. *Trans. Faraday Soc.,*, 1934.

[18] Brian De Force and Howard Pickering. A clearer view of how crevice corrosion occurs. *JOM*, 47(9):22–27, September 1995.

[19] J. R. Scully, N. Sridhar, D. S. Dunn, C. S. Brossia, G. A. Cragnolino, and J. R. Kearns. Crevice corrosion. *Corrosion Tests and Standards: Application and Interpretation-Second Edition*, January 2005.

[20] R. G. Kelly and K. C. Stewart. Combining the ohmic drop and critical crevice solution approaches to rationalize intermediate attack in crevice corrosion. *Corrosion science,*, 1934.

[21] J. W. Oldfield and W. H. Sutton. Crevice corrosion of stainless steels. i a mathematical model. *British Corrosion Journal*, 13(1):13–22, January 1978.

[22] JOSE R. Galvele. 1 - pitting corrosion. In J. C. Scully, editor, *Treatise on Material Science and Technology*, volume 23 of *Corrosion: aqueous process and passive film*, pages 1–57. Elsevier, January 1983.

[23] C. W. Shanley, R. E. Hummel, and E. D. Verink. Differential reflectometry—a new optical technique to study corrosion phenomena. *Corrosion Science*, 20(4):467–480, January 1980.

[24] Liao C.-M., Olive J. M., Gao M., and R. P. Wei. In-situ monitoring of pitting corrosion in aluminum alloy 2024. *Corrosion*, 54:451–458, October 1996.

[25] J. Li and D. Lampner. In-situ afm study of pitting corrosion of cu thin films. *Colloids and Surfaces A: Physicochemical and Engineering Aspects*, 154:227–237, August 1999.

[26] Jacob Nissim Israelachvili and David Tabor. The measurement of van der waals dispersion forces in the range 1.5 to 130 nm. *Proc. R. Soc. Lond. A*, 331(1584):19–38, November 1972.

[27] N. Tamura, A. A. MacDowell, R. Spolenak, B. C. Valek, J. C. Bravman, W. L. Brown, R. S. Celestre, H. A. Padmore, B. W. Batterman, and J. R. Patel. Scanning X-ray microdiffraction with submicrometer white beam for strain/stress and orientation mapping in thin films. *Journal of Synchrotron Radiation*, 10(2):137–143, March 2003.

[28] JN Israelachvili, NA Alcantar, N Maeda, TE Mates, and M Ruths. Preparing contamination-free mica substrates for surface characterization, force measurements, and imaging. *Langmuir*, 20(9):3616–3622, April 2004.

[29] S. Tolansky. *Multiple-beam interferometry of surfaces and films*. Dover Publications, 1970.

[30] Jacob N. Israelachvili and Patricia M. McGuiggan. Adhesion and short-range forces between surfaces. part i: new apparatus for surface force measurements. *Journal of Materials Research*, 5(10):2223–2231, October 1990.

[31] J Israelachvili, Y Min, M Akbulut, A Alig, G Carver, W Greene, K Kristiansen, E Meyer, N Pesika, K Rosenberg, and H Zeng. Recent advances in the surface forces apparatus (SFA) technique. *Reports on Progress in Physics*, 73(3), 2010.

[32] David Tabor and R. H. S. Winterton. The direct measurement of normal and retarded van der waals forces. *Proc. R. Soc. Lond. A*, 312(1511), September 1969.

[33] J. N. Israelachvili and G. E. Adams. Direct measurement of long range forces between two mica surfaces in aqueous kno_3 solutions. *Nature*, (5571):774–776, August 1976.

[34] J. N. Israelachvili. Techniques for direct measurements of forces between surfaces in liquids at the atomic scale. *Chemtracts: Anal. Phys. Chem*, 1:1–12.

[35] J. N. Israelachvili. Open discussion of papers by israelachvili, tirrell, and garoff. *Proceedings of the National Academy of Sciences*, 84(14):4733–4736.

[36] T. E. Balmer and M. Heuberger. Precision thickness and refractive index imaging of molecular films. *Review scientific instruments*, 78(14):3839–3848.

[37] M. Heuberger, G. Luengo, and J. Israelachvili. Topographic information from multiple beam interferometry in the surface forces apparatus. *Langmuir*, 13(14):3839–3848.

[38] Joëlle Fréchette and T. Kyle Vanderlick. Double layer forces over large potential ranges as measured in an electrochemical surface apparatus. *Langmuir*, 17:7620–7627, November 2001.

[39] A Tonck, J. M Georges, and J. L Loubet. Measurements of intermolecular forces and the rheology of dodecane between alumina surfaces. *Journal of Colloid and Interface Science*, 126(1):150–163.

[40] Jacob Klein. Forces between mica surfaces bearing adsorbed macromolecules in liquid media. *Journal of the Chemical Society, Faraday Transactions 1: Physical Chemistry in Condensed Phases*, 79(1):99–118.

[41] M. Heuberger, M. Zäch, and N. D. Spencer. Sources and control of instrumental drift in the surface forces apparatus. *Review of scientific instruments*, 71(12), 2000.

[42] Hugo K. Christenson and Christina E. Blom. Solvation forces and phase separation of water in a thin film of nonpolar liquid between mica surfaces. *The Journal of Chemical Physics*, 86(1):419–424.

[43] B. Moeremans, H. W. Cheng, Q. Hu, H.F. Garces, N. P. Padture, F. Renner, and M. Valtiner. Lithium-ion battery electrolyte mobility at nano-confined graphene interfaces. *Nature Communications*, 7:12693, August 2016.

[44] J. Balajka, A. M. Hines, J. I. W. DeBenedetti, and U. Diebold. High-affinity adsorption leads to molecularly ordered interfaces on tio 2 in air and solution. *Science*, 361:786–789, 2018.

[45] R. G. Connor, J. N. Horn. *Review of Scientific Instruments*, 74:4601–4606, 2003.

[46] P. Bilotto M. Lengauer C. Merola H. W. Cheng K. A. Schwenzfeier, A. Erbe and M. Valtiner. Optimizing multiple beam interferometry in the surface forces apparatus: Novel optics, reflection mode modelling, metal layer thicknesses, birefringence and rotation of anisotropic layers. *Review of Scientific Instruments, submitted*, November 2018.

[47] J. N Israelachvili. Thin film studies using multiple-beam interferometry. *Journal of Colloid and Interface Science*, 44:259–272, August 1973.

[48] J. M. Levins and T. K. Vanderlick. Extended spectral-analysis of multiple-beam interferometry. *Langmuir*, 10(7):2389–2394, July 1994.

[49] M. T. Clarkson. Multiple-beam interferometry with thin metal films and unsymmetrical systems. *Journal of Physics D - Applied Physics*, 22(4):475–482, April 1989.

[50] M. Heuberger. The extended surface forces apparatus. Part I. Fast spectral correlation interferometry. *Review of Scientific Instruments*, 72(3):1700–1707, March 2001.

[51] M. Born and E. Wolf. *Principles of Optics*, chapter 1.6.2. Pergamon Press, fourth edition, 1970.

[52] M. Schubert. Polarization-dependent optical parameters of arbitrarily anisotropic homogeneous layered systems. *Physical Review B*, 53(8):4265–4274, February 1996.

[53] R.B. Deboer, P.J.C. Nagtegaal, and E.M. Duyvis. Pressure solution on experiments on quarz sand. *Geochimica and cosmochimica acta*, 41(2):257–&, 1977.

[54] N Alcantar, J Israelachvili, and J Boles. Forces and ionic transport between mica surfaces: Implications for pressure solution. *Geochimica and cosmochimica acta*, 67(7):1289–1304, April 2003.

[55] N. Mishra, L. Hold, A. Iacopi, B. Gupta, N. Motta, and F. Iacopi. Controlling the surface roughness of epitaxial sic on silicon. *Journal of applied physics*, 115(20), May 2014.

[56] O Piotrowski, C Madore, and D Landolt. The mechanism of electropolishing of titanium in methanol-sulfuric acid electrolytes. *J. Electrochem. Soc.*, 145(7):2362–2369, July 1998.

[57] N. J. Laycock, J. Stewart, and R. C. Newman. The initiation of crevice corrosion in stainless steels. *Corrosion Science*, 39(10):1791–1809, October 1997.

[58] S.E. Lott and R.C. Alkire. The role of inclusion in initiation of crevice corrosion of stainless steel: experimental studies. *J. Electrochem. Soc.*, 136(4):973–979, April 1989.

[59] John O. Grippo, Marvin Simring, and Thomas A. Coleman. Abfraction, abrasion, biocorrosion and the enigma of noncarious cervical lesions: a 20 year perspective. *Journal of esthetic and restorative dentistry*, 24(1):10–23, 2012.

[60] HY Lin and JD Bumgardner. In vitro biocorrosion of Co-Cr-Mo implant alloy by macrophage cells. *Journal of orthopedica research*, 22(6):1231–1236, November 2004.

[61] P. Jakupi, J. J. Noel, and D. W. Shoesmith. Crevice corrosion initiation and propagation on alloy-22 under galvanically-coupled and galvanostatic conditions. *Corrosion science*, 53:3122–3130, October 2011.

[62] H Bohni. Breakdown of passivity and localized corrosion processes. *Langmuir*, 3(6):924–930, December 1987.

[63] P. Marcus, V. Maurice, and H. H. Strehblow. Localized corrosion (pitting): A model of passivity breakdown including the role of the oxide layer nanostructure. *Corrosion Science*, 50:2698–2704, September 2008.

[64] Bastian Maier and G. S. Frankel. Pitting corrosion of bare stainless steel 304 under chloride solution droplets. *J. Electrochem. Soc.*, 157:C302–C312, 2010.

[65] Sri Hastuty, Atsushi Nishikata, and Tooru Tsuru. Pitting corrosion of type 430 stainless steel under chloride solution droplet. *Corrosion Science*, (6):2035–2043, June 2010.

[66] N. S. Zadorozne, C. M. Giordano, M. A. Rodriguez, R. M. Carranza, and R. B. Rebak. Crevice corrosion kinetics of nickel alloys bearing chromium and molybdenum. *Electrochemica acta*, 76:94–101, August 2012.

[67] N.J. Laycock and R.C. Newman. Localised dissolution kinetics, salt films and pitting potentials. *Corrosion Science*, 39(10-11):1771–1790, November 1997.

[68] B. Malki, T. Souier, and B. Baroux. Influence of the alloying elements on pitting corrosion of stainless steels: A modeling approach. *J. Electrochem. Soc.*, 155(12):C583–C587, 2008.

[69] Yeong Ho Kim and G. S. Frankel. Effect of noble element alloying on passivity and passivity breakdown of Ni. *J. Electrochem. Soc.*, 154(1):C36–C42, 2007.

[70] B. T. Lu, J. L. Luo, and Y. C. Lu. A mechanistic study on lead-induced passivity-degradation of nickel-based alloy. *J. Electrochem. Soc.*, 154(8):C379–C389, 2007.

[71] S. P. Knight, M. Salagaras, A. M. Wythe, F. De Carlo, A. J. Davenport, and A. R. Trueman. In situ X-ray tomography of intergranular corrosion of 2024

and 7050 aluminium alloys. *Corrosion Science*, 52(12):3855–3860, December 2010.

[72] G. W. Greene, K. Kristiansen, E. E. Meyer, J. R. Boles, and J. N. Israelachvili. Role of electrochemical reactions in pressure solution. *Geochimica et cosmochimica acta*, 73(10):2862–2874, May 2009.

[73] B. R. Shrestha, Q. Hu, T. Baimpos, K. Kristiansen, J. N. Israelachvili, and M. Valtiner. Real-time monitoring of aluminum crevice corrosion and its inhibition by vanadates with multiple beam interferometry in a surface forces apparatus. *J. Electrochem. Soc.*, 162:C327–C332, 2015.

[74] J Frechette and TK Vanderlick. Control of adhesion and surface forces via potential-dependent adsorption of pyridine. *Journal of physical chemistry B*, 109(9):4007–4013, March 2005.

[75] Israelachvil, J.N. Thin film studies using multiple beam interferometry. *Journal of colloidal and interface science*, 44(2):259–272, 1973.

[76] O Lev, F.R. Fan, and A.J. Bard. The application of scanning tunneling microscopy to insitu studies of nickel electrodes under potential control. *J. Electrochem. Soc.*, 135(3):783–784, March 1988.

[77] JN Connor and RG Horn. Extending the surface force apparatus capabilities by using white light interferometry in reflection. *Review of Scientific Instruments*, 74(11):4601–4606, November 2003.

[78] M Schubert. Polarization-dependent optical parameters of arbitrarily anisotropic homogeneous layered systems. *Physical review B*, 53(8):4265–4274, February 1996.

[79] J R. Scully and S T. Hensley. Lifetime prediction for organic coatings on steel and a magnesium alloy using electrochemical impedance methods. *Corrosion*, 50:705–716, 1994.

[80] K. Kristiansen, M. Valtiner, G. W. Greene, J. R. Boles, and J. N. Israelachvili. Pressure solution - the importance of the electrochemical surface potentials. *Geochimica and cosmochimica acta*, 75:6882–6892, November 2011.

[81] JN Israelachvili. *Intermolecular and Surface Forces*. Academic, San Diego, 2011.

[82] G.S. Frankel, J.O. Dukovic, V. Brusic, B.M. Rush, and C.V. Jahnes. Pit growth in nife thin films. *J. Electrochem. Soc.*, 139(8):2196–2201, August 1992.

[83] V. Maurice and P. Marcus. Passive films at the nanoscale. *Electrochemica acta*, 84:129–138, December 2012.

[84] V. Maurice, L.H. Klein, and P. Marcus. Atomic structure of metastable pits formed on nickel. *Electrochemical and solid state letters*, 4(1):B1–B3, January 2001.

[85] Rayleigh L. On the equilibrium of liquid conducting masses charged with electricity. *Philos. Mag.*, 1882.

[86] GS Frankel. Pitting corrosion of metals - A review of the critical factors. *J. Electrochem. Soc.*, 145(6):2186–2198, June 1998.

[87] M. K. Sawford, B. G. Ateya, M. A. Abdullah, and H. W. Pickering. The role of oxygen on the stability of crevice corrosion. *J. Electrochem. Soc.*, June 2002.

[88] G. S. Frankel, L. Stockert, F. Hunkeler, and H. Boehni. Metastable pitting of stainlees steels. *Corrosion*, 43:429–436, 1987.

[89] D. V. Vasquez Moll, R. C. Salvarezza, H. A. Videla, and A. J. Arvia. The Pitting Corrosion of Nickel in Different Electrolyte Solutions Containing Chloride Ions. *J. Electrochem. Soc.*, 132:754–760, 1985.

[90] N. D. Tomashov, G. P. Chernova, and O. N. Marcova. Effect of Supplementary Alloying Elements On Pitting Corrosion Susceptibility Of 18cr-14ni Stainless Steel. *Corrosion*, 20:166t–173t, 1964.

[91] A. A. Seys, M. J. Brabers, and A. A. Van Haute. Analysis of the Influence of Hydrogen on Pitting Corrosion and Stress Corrosion of Austenitic Stainless Steel in Chloride Environment. *Corrosion*, pages 47–52, 1974.

[92] H.-H. Strehblow. Nucleation and repassivation of corrosion pits for pitting on iron and nickel. *Materials and Corrosion*, 27:792–799, 1976.

[93] Ja. M. Kolotyrkin. Pitting corrosion of metals. *Corrosion*, 19:261t–268t, 1963.

[94] Z. Szklarska-Smialowska. Review of literature on pitting corrosion published since 1960. *Corrosion*, 27:223–233, 1971.

[95] Helmuth Sarmiento Klapper, Natalia S. Zadorozne, and Raul B. Rebak. Localized corrosion characteristics of nickel alloy: a review. *Acta Metallurgica Sinica*, 30:296–305, 2017.

[96] Mirna Urquidi and Digby Macdonald. solute/vacancy interaction model for

the effect of minor alloying eleemnts on the breakdown of passive films. *Electrochemical Society Extended Abstracts*, 85:29–30, 1985.

[97] Masao Sakashita and Norio Sato. The effect of molybdate anion on the ion-selectivity of hydrous ferric oxide films in chloride solutions. *Corrosion Science*, 17:473–486, 1977.

[98] B. C. Syrett, D. D. Macdonald, and H. Shih. Pitting resistance of engineering materials in gethermal brines: low salinity brine. *Corrosion*, 36:130–139, 1980.

[99] Christopher M. Wylie, Richard M. Shelton, Garry J. P. Fleming, and Alison J. Davenport. Corrosion of nickel-based dental casting alloys. *Dental Materials*, 23:714–723, June 2007.

[100] J. R. Hayes, J. J. Gray, A. W. Szmodis, and C. A. Orme. Influence of Chromium and Molybdenum on the Corrosion of Nickel-Based Alloys. *Corrosion*, 62, June 2006.

[101] Corrosion Resistance of Nickel and Nickel Alloys Against Acids and Lyes.

[102] Guojin Lu and Giovanni Zangari. Corrosion resistance of ternary NiP based alloys in sulfuric acid solutions. *Electrochimica Acta*, 47:2969–2979, July 2002.

[103] Nilo A. S. Sampaio, José W. J. Silva, Heloisa A. Acciari, Roberto Z. Nakazato, Eduardo N. Codaro, and Hamilton de Felipe. Influence of Ni and Cr Content on Corrosion Resistance of Ni-Cr-Mo Alloys for Fixed Dental Prostheses in 0.05% NaF Aqueous Solution. *Materials Sciences and Applications*, 01:369, December 2010.

[104] J. Horvath and H. H. Uhlig. Critical potential for pitting corrosion of Ni, Cr-Ni, Cr-Fe, andrelated stainlees steels. *J. Electrochem. Soc.*, 115:791–795, 1968.

[105] Smith Kaye Kheyrandish Colligon Fujimoto, Newman. Passivation thresold in iron-chromium alloys prepared by ion-beam sputtering. *Corrosion Science*, 35:51–55.

[106] N. Ebrahimi, P. Jakupi, J.j. Noël, and D.w. Shoesmith. The role of alloying elements on the crevice corrosion behaviour of ni-cr-mo alloys. *Corrosion*, 71:1441–1451, 2015.

[107] P. Marcus and J. M. Grimal. The anodic dissolution and passivation of NiCrFe alloys studied by ESCA. *Corrosion Science*, 33:805–814, May 1992.

[108] S. Nagarajan and N. Rajendran. Crevice corrosion behaviour of super-austenitic stainless steels: Dynamic electrochemical impedance spectroscopy and atomic force microscopy studies. *Corrosion Science*, 51:217–224, 2009.

[109] Hiroyuki Ogawa, Hiroyasu Omata, Isao Itoh, and Hideya Okada. Auger electron spectroscopic and electrochemical analysis of the effect of alloying elements on the passivation behaviour of stainless steels. *CORROSION*, 34:52–60, February 1978.

[110] L. Lazzari. *4 - Pitting and Crevice Corrosion*. European Federation of Corrosion (EFC) Series. January 2017.

[111] Z. Ahmad. *Principles of Corrosion Engineering and Corrosion Control*, chapter 4, pages 120–270. Oxford, July 2006.

[112] J. Kruger and S. Begum. *Corrosion of Metals: Overview*. Elsevier, January 2016.

[113] Israelachvili JN, Younjin Min, Mustafa Akbulut, A Alig, G Carver, George Greene, K Kristiansen, E Meyer, N Pesika, K Rosenberg, and Hongbo Zeng. Recent advances in the surface forces apparatus (SFA) technique. *Reports on Progress in Physics*, 73:036601, 2010.

[114] K. Schwenzfeier K. Kristiansen Y.J. Chen H. A. Dobbs J N Israelachvili C. Merola, H. W. Cheng and M. Valtiner. In situ nano-to microscopic imaging and growth mechanism of electrochemical dissolution (e.g. corrrosion) of a confined meta surface. *PNAS*, 114:9541–9546, 2017.

[115] Ulaganathan J., Carcea A.G., Newman R.C., Barabash R.I., and N. S. McIntyre. Mapping of changes in microscopic strain in alloy 600 during multi-step applications of mechanical stress. *Surface Interface Analysis*, 49:1442–1448, 2017.

[116] Brewer L. N., Field D.P., and Merriman C.C. *Mapping and assessing plastic deformation using EBSD in material science*. Springer, 2009.

[117] E. Y. Ma et al. Mobile metallic domain walls in an all-in-all-out magnetic insulator. *Science*, 350:538–541.

[118] N. Tamura K. Chen, M. Kunz and H. R. Wenk. Residual stress preserved in quartz from san Andreas fault observatory at depth. *Geology*, 43:219–222.

[119] A. Mehta et al. Understanding the deformation and fracture of nitinol endovascular stents using in situ synchrotron x-ray microdiffraction. *Advanced Material*, 19:1183–1186.

[120] V. Shkirskiy, P. Maciel, J. Deconinck, and K. Ogle. On The Time Resolution of the Atomic Emission Spectroelectrochemistry Method. *J. Electrochem. Soc.*, 163(3):C37–C44, January 2016.

[121] L. Rossrucker, K. J. J. Mayrhofer, G. S. Frankel, and N. Birbilis. Investigating the real time dissolution of mg using online anaysis by icp-ms. *J. Electrochem. Soc.*, 161:C115–C119, 2014.

[122] M. J. Duarte, J. Klemm, S. O. Klemm, K. J. J. Mayrhofer, M. Stratmann, S. Borodin, A. H. Romero, M. Madinehei, D. Crespo, J. Serrano, S. S. A. Gerstl, P. P. Choi, D. Raabe, and F. U. Renner. Element-resolved corrosion analysis of stainless type glass forming steels. *Science*, 341:372–376, 2013.

[123] K. Ogle and S. Weber. Anodic dissolution of 304 stainless steel using atomic emission spectroelectrochemistry. *J. Electrochem. Soc.*, 147:1770–1780, 2000.

[124] Katsuhisa Sugimoto and Yoshinobu Sawada. The role of alloyed molybdenum in austenitic stainless steels in the inhibition of pitting in neutral halide solutions. *Corrosion*, 32(9):347–352, September 1976.

[125] A Machet, A Galtayries, S Zanna, L Klein, V Maurice, P Jolivet, M Foucault, P Combrade, P Scott, and P Marcus. XPS and STM study of the growth and structure of passive films in high temperature water on a nickel-base alloy. *Electrochimica Acta*, 49(22):3957–3964, September 2004.

Appendix

Resulting publications

As first author:

- "C. Merola, H. W. Cheng, K. Schwenzfeier, K. Kristiansen, Y. J. Chen, H. A. Dobbs, J. N. Israelachvili, and M. Valtiner", "In situ nano-to microscopic imaging and growth mechanism of electrochemical dissolution (e.g. corrrosion) of a confined meta surface.,"PNAS , vol. 114,pp. 9541–9546, 2017"
- "C. Merola, H.-W. Cheng, D. Dworschak, C.-S. Ku,C.-Y. Chiang, F.U.Renner, and M. Valtiner" Nanometer resolved real time visualization of acidification and material breakdown of Nickel and $Ni_{75}Cr_{16}Fe$ alloy in confinement" submitted.
- "D. Dworschak*, C. Merola*, H.-W. Cheng, M. Valtiner", Time resolved elemental dissolution rates during transpassive anodic polarization of nickel base alloys in the presence of chloride" submitted. [1]

As corresponding author:

- " V. Dandapani, A. Altin, C. Merola and M. Rohwerder" "Probing the Buried Metal-Organic Coating Interfacial Reaction Kinetic Mechanisms by a Hydrogen Permeation Based Potentiometric Approach" Journal of the electrochemical society, 2016
- " H. W. Cheng, J.-N. Dienemann, P. Stock, C. Merola, Y. J. Chen, M. Valtiner" "The Effect of Water and Confinement on Self-Assembly of Imidazolium Based Ionic Liquids at Mica Interfaces" Scientific Reports 2016
- "B. Moeremans, H. W. Cheng, C. Merola, Q. Hu, M. Bael, An Hardy, M. Valtiner and R. U. Renner" "In-situ nanoscopic mechanical analysis of the

[1]* Authors contributed equally

solid electrolyte interphase in lithium batteries"

- "K. A. Schwenzfeier, A. Erbe, P. Bilotto, M. Lengauer, C. Merola, H. W. Cheng, and M. Valtiner" , "Optimizing multiple beam interferometry in the surface forces apparatus: Novel optics, reflection mode modelling, metal layer thicknesses, birefringence and rotation of anisotropic layers." submitted.

Conference participation

- GGRC - Aqueous Corrosion, New London, NH (USA), July 2016(Poster)(Simultaneous Interferometry and Microscopy Reveal Unexpected Nickel Corrosion Dynamics in Confined Geometry) (C. Merola, H. W. Cheng, K. Kristiansen, Y. J. Chen, J. Israelachvili and M. Valtiner)
- ECS Honolulu October 2016 (Poster)(Simultaneous Interferometry and Microscopy Reveal Unexpected Nickel Corrosion Dynamics in Confined Geometry) (C. Merola, H. W. Cheng, K. Kristiansen, Y. J. Chen, J. Israelachvili and M. Valtiner)
- DPG Dresden March 2017 (Talk)(In-situ confinement monitoring by using newly developed Surface Force Apparatus) (C. Merola, H. W. Cheng, K. Kristiansen, Y. J. Chen, J. Israelachvili and M. Valtiner)
- EuroCorr 2017 Prague September (Talk)(In situ nano- to microscopic imaging and growth mechanism of electrochemical dissolution (e.g., corrosion) of a confined metal surface.) (C. Merola, H.-W. Cheng,K. Schwenzfeier,K. Kristiansen, Y.-J. Chen, H. A. Dobbs, J. N. Israelachvili, and M.Valtiner)
- AVS October 2017 Tampa (Talk) (Interferometry: A New Way to Study Corrosion at Confined Interfaces), (C.Merola, H.W. Cheng, K. Schwenzfeier and M. Valtiner)
- GRC - Aqueous Corrosion, New London, NH (USA), July 2018 (Conference Chair)
- Eurocorr September 2018 Krakow (Talk)("Unravelling of corrosion mechanism in nanometer confined gaps using white light interferometry in reflection and transmission mode") (C. Merola, H.W. Cheng, D. Dworshak & Markus Valtiner)

Copyright permission

RE: request the permission for the article to be printed in Dissertation

Messaggio 1 di 2

Mittente PNAS Permissions
Destinatario merola@iap.tuwien.ac.at
Data 2018-10-16 19:21

Thank you for your message. Authors do not need to obtain permission for the following uses of material they have published in PNAS:

- to use their original figures or tables in their future works;
- to make copies of their papers for their own personal use, including classroom use, or for the personal use of colleagues, provided those copies are not for sale and are not distributed in a systematic way;
- to include their articles as part of their dissertations; or
- to use all or part of their articles in printed compilations of their own works.

Please include a complete citation for the original PNAS article when reusing the material, and include "Copyright (copyrightyear) National Academy of Sciences, U.S.A." as a copyright note. Because this material published between 1993 and 2008, a copyright note is required.

You may also refer to http://www.pnas.org/page/authors/licenses for more information. Feel free to contact us with any additional questions you might have.

Sincerely,

Kay McLaughlin for
Diane Sullenberger
PNAS Executive Editor

-----Original Message-----
From: merola@iap.tuwien.ac.at <merola@iap.tuwien.ac.at>
Sent: Monday, October 15, 2018 3:24 AM
To: PNAS Permissions <PNASPermissions@nas.edu>
Subject: [SUSPECTED SPAM] request the permission for the article to be printed in Dissertation

To whom it may concern,

I Would like to request the permission for the article : "In situ nano- to microscopic imaging and growth mechanism of electrochemical dissolution (e.g., corrosion) of a confined metal surface" in order to include it in my Dissertation.

Author informations:

Claudia Merola
PhD Student at Technical University of Vienna Wiedner Hauptstraße 8-10
1030 Wien
+43-1-58801-13443
merola@iap.tuwien.ac.at

Article information:

"In situ nano- to microscopic imaging and growth mechanism of electrochemical dissolution (e.g., corrosion) of a confined metal surface"
PNAS September 5, 2017 114 (36) 9541-9546 published ahead of print August 21, 2017
https://doi.org/10.1073/pnas.1708205114

Best Regards,
Claudia Merola

Claudia Merola

Address	Zaunergasse 16
	1030 Wien
	Österreich
Personal Data	+49 1523/6655205
	claudia.merola@mailbox.org
Date of birth and place	31.05.1989 in Milan (Italy)
Nationality	Italian

Studies and background

08. 2015 - ca. 01. 2019 **PhD candidate at Technical University Vienna**

- Part of the Outreach Projects in Wien
- Moved to Vienna to follow my supervisor.
- Continued the projects started in Düsseldorf.
- Collaboration with industries on projects related to corrosion and adhesion forces.

PhD candidate at Max Planck institut für Eisenforschung in Düsseldorf

- Emphasis on electrochemistry, corrosion and material science.
- PhD programme of the International Max Planck Research School for Interface Controlled Materials for Energy Conversion (IMPRS-SurMat) with focus on chemistry, physic and material science.
- Graduate Course in corrosion science at Eurocorr in Prague (1-3 September 2017).

10. 2014 – 06. 2015 **Master of second degree in Intellectual property and Trademarks at University of Milan**

- knowledge about the Italian and European patent law.
- extensive exercises in reading and writing patents.

10.2013 – 07.2015 **Master degree in Industrial Chemistry and management at University of Milan**

- Emphasis: chemistry and physics.
- Knowledge of theory and practical aspects of the industrial production in different areas of chemistry, specifically concerning the product-process relationship. Acquisition of good knowledge of economics and management.
- Note: 107/110
- Thesis title: *The world of heat exchangers. The role of applied polymers in affecting the final performances.*

10.2011 – 07.2014 **Accounting Secretary at Residence Consult Hotel, Milano**

10.2010 – 07.2013 **Bachelor degree in Industrial Chemistry at University of Milan**

- Emphasis: Chemistry and industrial processing.
- Thesis title: *Synthesis and characterization of reinforced hydrogels with polyamidoamine for tissue engineering.*

07.2009 – 06.2010 **Brittin College in Vancouver, Canada**

- Preparation for university attendance.
- Co-founder of the EF school Journal of Vancouver.

09. 2004 – 07.2009 **Scientific highschool Giordano Bruno in Cassano d´Adda, Italy**

- Fundamentals of the main scientific notions in the following areas : algebra , geometry , physics, chemistry.
- General bases of the history of humanistic thought , mainly in the following areas : Italian literature , Latin and English , philosophy , history.

Publication, awards and conferences

2018 C. Merola *et al.* Initial crevice corrosion of alloy 600 and model derivatives: In situ visualization using interferometric microscopy and complementary analysis using an ICP-MS flow cell, AFM and nano-Laue diffraction (to be submitted).

07.2016 – 07.2018 Conference Chair : Gordon Seminar Conference in Aqueous Corrosion 2018.

03.2017 – 12.2017 External PhD representative of Max Planck Institute in Düsseldorf

10. 2017 The Biointerphases First Prize Student Award at the AVS 64 International Symposium.

08. 2017 C. Merola *et al.* In situ nano- to microscopic imaging and growth mechanism of electrochemical dissolution (e.g., corrosion) of a confined metal surface (PNAS).

Conferences

GRC Boston July 2016(Poster), ECS Honolulu October 2016 (Poster), DPG Dresden March 2017 (Talk), EuroCorr 2017 Prague September (Talk), AVS October 2017 Tampa (Talk), GRC Boston July 2018 (Chair Conference), Eurocorr September 2018 Krakow (Talk).

Additional knowledge

Languages	Italian (mother tongue), English (C1), German (C1) and French (B1)
IT-Knowledge	Microsoft Office (Excel, Power Point, Word), Solidedge, Keyshot, Origin, Blender, Adobe Illustrator, Photoshop. Python courses: Python Bootcamp: Vom Anfänger zum Profi, inkl. Data Science and Python for Data Science and machine learning. Introduction course to HTML, CSS Java script and SQL.
Extra	Driving licence B
Sports	Marathon runner

List of Figures

1.1 Economic loss by field due to corrosion. 4
1.2 Corrosion cell. 6
1.3 Pourbaix diagram for a general metal. 7
1.4 Crevice corrosion schematic 9

2.1 Schematic of a SEM and EBSD 16
2.2 Principles of AFM 19
2.3 Schematic of synchrotron setup 20
2.4 Principles of XPS 22

3.1 Schematic MBI 27
3.2 Relation between the shift of the FECO and the separation distance of the surfaces. 28
3.3 FECOs during the approach of two surfaces 29
3.4 SFA setup: overview 31
3.5 Traditional SFA setup 32
3.6 Error in optics alignment 34
3.7 Relevance of background 36
3.8 Improved optics in SFA 38
3.9 Relation between FECO and NR during alignment 39
3.10 FECO variation during the dissolution process 41
3.11 Schematic of optical path in reflection mode. 42
3.12 Schematic of the interference pattern in reflection mode 43
3.13 FECO comparison in transmission and reflection mode 44
3.14 Crevice former and crevice configuration in SFA 46
3.15 A comparison of the corrosion process between transmission mode SFA and reflection mode SFA 47

4.1 Modified Ec-SFA 52
4.2 Relation between nickel thickness and transmission 55
4.3 Injection of the electrolyte 56
4.4 Optical images of the corrosion process in-situ 57

4.5 Simulated current during corrosion process 58
4.6 Proposed mechanism of nickel/nickel oxide dissolution/corrosion. . . 61
4.7 Electrochemically measured current density 62
4.8 Simulated confinement environment 65
4.9 Evans diagram of nickel 66
4.10 Step potential curve 67
4.11 Calculated local charge 68
4.12 Probability chart of the staring position of the corrosion process. . . 69
4.13 Relation between the structure and the corrosion mechanism of thin film nickel. 70

5.1 Reflection mode SFA and detail view of the interferometer setup . . 74
5.2 EC-RSFA 76
5.3 Establishing and characterization of confined zones 77
5.4 Time lapse of the corrosion of the pure nickel sample 78
5.5 Speed corrosion analysis of the nickel alloy 80
5.6 Bending of the Newton bands due to the dissolution of the oxide . . 81
5.7 XPS analysis of pure nickel 82
5.8 XPS analysis of $Ni_{75}Cr_{16}Fe_9$ 83
5.9 Post-experiment analysis of the corrosion area with AFM. 85
5.10 Taiwan Photon Source Beamline 21A set-up. 87
5.11 Nano-Laue X-ray diffraction analysis. 88
5.12 Diffraction indexing and mapping of the FW 89
5.13 Mapping of FW 90

6.1 Avesta/confinement cell 96
6.2 Components of the ICP-MS 97
6.3 EC-ICP-MS 98
6.4 Ratio of the components of the alloy in stagnant solution 99
6.5 Dissolution of nickel alloy considering the pH variation 100
6.6 ICP-MS spectro-electrochemistry of $Ni_{75}Cr_{16}Fe_9$ at different pH . . 103
6.7 ICP-MS spectroelectrochemistry of $Ni_{86}Cr_5Fe_9$ 104
6.8 ICP-MS spectroelectrochemistry of $Ni_{84}Cr_5Fe_9Mo_1$ 106

List of Tables

4.1 Correspondence between the potential and number of pits 67

5.1 Spatially resolved corrosion rates for the $Ni_{75}Cr_{16}Fe_9$ along the major and minor axis of the confined zones. 79